

Development of a genetic algorithm approach to
calibrate the EVPSC model

DEVELOPMENT OF A GENETIC ALGORITHM APPROACH TO
CALIBRATE THE EVPSC MODEL

BY
HANQING GE, B.Sc.

A THESIS
SUBMITTED TO THE DEPARTMENT OF MECHANICAL ENGINEERING
AND THE SCHOOL OF GRADUATE STUDIES
OF MCMASTER UNIVERSITY
IN PARTIAL FULFILMENT OF THE REQUIREMENTS
FOR THE DEGREE OF
MASTER OF APPLIED SCIENCE

© Copyright by Hanqing Ge, September 2016

All Rights Reserved

Master of Applied Science (2016)
(Mechanical Engineering)

McMaster University
Hamilton, Ontario, Canada

TITLE: Development of a genetic algorithm approach to calibrate
the EVPSC model

AUTHOR: Hanqing Ge
B.Eng. (Shanghai Jiao Tong University)

SUPERVISOR: Dr. P.D.Wu

NUMBER OF PAGES: xiv, 117

This is dedicated to my beloved parents and boyfriend

Abstract

Magnesium is known as one of the lowest density metals. With the increasing importance of fuel economy and the need to reduce weight, magnesium has proven to be a very important structural material used in transportation industry. However, the use of magnesium alloys have been limited by its tendency to corrode, creep at high temperature, and higher cost compare to aluminium alloys and steels.

Polycrystal plasticity models such as VPSC and EVPSC were used to study deformation mechanisms of magnesium alloys. However, current polycrystal plasticity models with slip and twinning involve a large number of material parameters, which may not be uniquely determined. Furthermore, determining material parameters using traditional trial-and-error approach is very time consuming. Therefore, a genetic algorithm approach is developed in this thesis to optimize these material parameters.

The genetic algorithm approach is evaluated by studying large strain behavior of magnesium alloys under different deformation processes. The material parameters for those models are determined by material numerical simulations based on the polycrystal model to the corresponding experimental data. Then the material parameters are used to make prediction of other deformation behaviors (stress strain curves, R values, texture evolution and lattice strain), and the performance is judged by how well the prediction match the actual experimental data. The results show that the genetic algorithm approach works well on determining parameters, it can get reliable results within a relatively short period of time.

Acknowledgements

First of all, I would like to give my deepest appreciation to my supervisor Prof. Wu. Without your guidance, support and encouragement, this thesis would not have been possible. Your mentorship, broad knowledge background, and the opportunities you have given me have truly enriched both me and my experience as a graduate student.

To many of my colleagues in research group and my good friends Hua Qiao, Xiaoqian Guo, Yue Fu, Shu Deng, thank you for your company, support and selfless help. You are my best teammates and best friends during the hardest period of my life.

To my boyfriend Hongbo Fan, for all your love and support. Words cannot describe how lucky I am to have you in my life. You have selflessly given more to me than I ever could have asked for.

To my parents, back home in China, thank you for your sacrificial love and supporting while I am studying abroad. Thank you both for giving me strength to reach for the stars and chase my dreams.

List of Abbreviations

BCC	body center cubic
CDC	channel die compression
CG	composite grain
CRSS	critical resolved shear stress
EPSC	elasto plastic self-consistent
EVPSC	elastic-viscoplastic self-consistent
FCC	face centered cubic
FEA	finite element analysis
GA	genetic algorithm
HCP	hexagonal close packed
HEM	homogeneous effective medium
MTS	Mechanical Threshold Stress
ND	normal direction
ND-C	compression along normal direction
ND-T	tension along normal direction
PTR	predominant twin reorientation
PTS	predominant twin system
RC	relaxed constraints
RD	rolling direction
RD-C	compression along rolling direction
RD-T	tension along rolling direction
RSS	resolved shear stress
SC	self-consistent

TD	transverse direction
TDT	twinning and de-twinning
TD-C	compression along transverse direction
TD-T	tension along transverse direction
TT	through-thickness
VFT	volume fraction transfer
VPSC	visco-plastic self-consistent

Contents

Abstract	iv
Acknowledgements	v
List of Abbreviations	vi
1 General introduction	1
1.1 Background	1
1.2 Thesis outline	3
2 Literature review	4
2.1 Overview of magnesium	4
2.2 Deformation of HCP metals	6
2.2.1 Elastic behavior	6
2.2.2 Slip	8
2.2.3 Twinning	10
2.3 Deformation modeling	11
2.3.1 Homogenisation schemes	12
2.3.2 Twinning models	15
3 Genetic algorithm approach	19
3.1 Introduction of genetic algorithm	19
3.2 Procedure of genetic algorithm approach	22
4 Study of magnesium alloy ZEK100 under tension and compression in different orientations	25

4.1	Introduction	25
4.2	Constitutive model	27
4.2.1	Crystal plasticity	27
4.2.2	Twinning model	31
4.3	Genetic algorithm approach	32
4.4	Results and discussion	33
4.5	Conclusion	47
5	Study of magnesium alloy with random texture under tension and compression	48
5.1	Introduction	48
5.2	Constitutive model	51
5.2.1	Crystal plasticity	51
5.2.2	Twinning model	53
5.3	Genetic algorithm	61
5.4	Results and discussion	64
5.5	Conclusion	73
6	Study of rolled magnesium AZ31 alloy under uniaxial compression and plane strain compression	75
6.1	Introduction	75
6.2	Constitutive model	77
6.2.1	Crystal plasticity	77
6.2.2	Twinning mode	81
6.3	Results and discussion	82

6.4 Conclusion	101
7 General conclusions	102

List of Figures

Figure 2.1 HCP single crystal structure.	6
Figure 2.2 Frequently observed slip systems in magnesium at room temperature (Partridge, 1967).	9
Figure 2.3 Crystallographic elements of twinning (Partridge, 1967).	10
Figure 2.4 Twinning modes in magnesium at room temperature.	11
Figure 3.1 Procedure of genetic algorithm approach.	24
Figure 4.1 Initial texture of ZEK100 sheet represented in terms of the $\{0001\}$, $\{10\bar{1}0\}$ and $\{11\bar{2}0\}$ pole figures.	35
Figure 4.2 Stress - plastic strain curves of ZEK100 sheet in different orientations(Kurukuri <i>et al.</i> , 2014).	36
Figure 4.3 Fitted stress strain curves (a) and activities (b) under tension along RD (RD-T).	37
Figure 4.4 Fitted stress strain curves (a) and activities (b) under compression along RD (RD-C).	37
Figure 4.5 Fitted stress strain curves (a) and activities (b) under compression along TT (TT-C).	38
Figure 4.6 Predicted stress strain curves (a) and activities (b) under tension along TD (TD-T).	39
Figure 4.7 Predicted stress strain curves (a) and activities (b) under compression along TD (TD-C).	39
Figure 4.8 Predicted stress strain curves (a) and activities (b) under tension along 45° (45-T).	40

Figure 4.9	Predicted stress strain curves (a) and activities (b) under compression along 45° (45-C).	40
Figure 4.10	Instantaneous R values in different orientations in (a) tension and (b) compression.	41
Figure 4.11	Predicted $\{0001\}$ and $\{10\bar{1}0\}$ pole figures of (a) initial texture (b) under tension along RD at strain = 0.15.	44
Figure 4.12	Predicted $\{0001\}$ and $\{10\bar{1}0\}$ pole figures of (a) initial texture (b) under tension along TD at strain = 0.2.	45
Figure 4.13	Predicted $\{0001\}$ and $\{10\bar{1}0\}$ pole figures of deformed compression samples at strain = 0.1 along (a) RD, (b) TD, (c) TT.	46
Figure 5.1	Schematic representation of twinning and de-twinning in a grain (Wang <i>et al.</i> , 2012a).	54
Figure 5.2	Initial texture of the random texture cast magnesium represented in terms of the $\{0001\}$, $\{10\bar{1}0\}$ and $\{11\bar{2}0\}$ pole distributions.	65
Figure 5.3	Experiment (symbols) and simulated (solid lines) true stress and true strain curves under (a) uniaxial compression, (c) uniaxial tension, Predicted slip/twinning activities under (b) uniaxial compression (d) uniaxial tension.	67
Figure 5.4	Experimental(symbols) and simulated(lines lines) twinned volume fraction in tension(red) and compression(black). The experimental data are taken from Čapek <i>et al.</i> (2014).	68
Figure 5.5	Simulated texture evolution in uniaxial compression.	69
Figure 5.6	Simulated texture evolution in uniaxial tension.	70

Figure 5.7	Experimental (symbols) and simulated (lines) lattice strain evolution versus the applied stress in uniaxial compression for both direction.	72
Figure 5.8	Experimental (symbols) and simulated (lines) lattice strain evolution versus the applied stress in uniaxial tension for both direction.	72
Figure 6.1	Initial texture presented in terms of the $\{0001\}$, $\{10\bar{1}0\}$ and $\{11\bar{2}0\}$ pole figures.	84
Figure 6.2	Schematic representation of a uniaxial compression sample with an angle α rotating around the RD from the ND to the loading direction (LD).	84
Figure 6.3	Experimental true stress and strain curves under (a) channel-die compression (CD) and (b) uniaxial compression (UC).	85
Figure 6.4	Experiment (symbols) and simulated (solid lines) stress - strain curves and activities under (a,b) CD-0; (c,d) UC-0.	88
Figure 6.5	Experiment (symbols) and simulated (solid lines) stress - strain curves and activities under (a,b) CD-90; (c,d) CD-RD.	90
Figure 6.6	Experiment (symbols) and simulated (solid lines) stress - strain curves and activities under (a,b) CD-30; (c,d) CD-45; (e,f) CD-60. . .	91
Figure 6.7	Experiment (symbols) and simulated (solid lines) stress - strain curves and activities under (a,b) UC-30; (c,d) UC-45; (e,f) UC-60. . .	93
Figure 6.8	Experiment (symbols) and simulated (solid lines) stress - strain curves and activities under (a,b) UC-90; (c,d) UC-RD.	94
Figure 6.9	Predicted total twin volume fraction under (a) channel-die compression, (b) uniaxial compression along different tilt angles.	95

Figure 6.10 Predicted twin volume fraction of (a) tensile twinning and (b) compression twinning under channel-die compression.	97
Figure 6.11 Predicted twin volume fraction of (a) tensile twinning and (b) compression twinning under uniaxial compression.	97
Figure 6.12 Predicted texture evolution under Channel-die compression along (a) $\alpha = 0^\circ$; (b) $\alpha = 45^\circ$; (c) $\alpha = 90^\circ$	99
Figure 6.13 Predicted texture evolution under uniaxial compression along (a) $\alpha = 0^\circ$; (b) $\alpha = 45^\circ$; (c) $\alpha = 90^\circ$	100

Chapter 1

General introduction

1.1 Background

Magnesium, as one of the lowest density structural metals, has attracted the interest of many researchers in recent years. It is also a highly competitive material for transportation industry due to the increasing importance of fuel economy and the need to reduce weight. However, the use of magnesium alloy has been limited by its tendency to corrode, creep at high temperatures, and higher cost compared to aluminium alloys and steels (Hirsch and Al-Samman, 2013).

Despite the efforts of the scientific community in the last several decades the study of the deformation properties of magnesium alloys is still a challenging task. The magnesium alloys have a hexagonal closed packed (HCP) structure, which leads to a unique deformation behavior completely different from other cubic metals. In most FCC and BCC crystal, plastic deformation is dominated by crystallographic slip. However, in HCP, both slip and twinning contribute to it is plastic deformation, which leads to difficulties and uncertainties in the simulation of HCP polycrystal.

Various constitutive models have been developed to describe polycrystalline deformation. In early study of polycrystal plasticity models, Sachs model (Sachs, 1928) and Taylor model (Taylor, 1938) were the most famous two. Later, Kröner (1958) proposed another popular homogenizing method, self-consistent approach. The self-consistent approach considers all the grains with the same orientation as an inclusion embedded in a homogeneous effective medium (HEM), which is an aggregate of all the

inclusions. The external imposed stress and strain should coincide with the average of the aggregate.

Visco-Plastic Self-Consistent (VPSC) model is a popular self-consistent model. It is proposed by Lebensohn and Tomé (1993). This model is applied to simulate large strain behavior and texture evolution of HCP polycrystalline under various deformations, and it works well. However, VPSC model focus on visco-plastic deformation, it does not take elastic deformation into consideration. Wang *et al.* (2010c) developed a finite strain Elastic-Viscoplastic Self-Consistent (EVPSC) model for polycrystalline materials. It is a completely general elasticviscoplastic, fully anisotropic, self-consistent polycrystal model, applicable at large strain and to any crystal symmetry.

An important aspect associated with various crystal plasticity models is how to incorporate a reorientation scheme for deformation twinning into the constitutive model. Tomé *et al.* (1991) proposed a predominant twin reorientation (PTR) model. In recent years, Wang *et al.* (2012a) developed a new constitutive twinning model, twinning-detwinning (TDT) model. TDT model gives out more accurate simulated result during strain path changes tests.

It has been noticed that the current polycrystal plasticity models with slip and twinning involve a large number of material parameters, which may not be uniquely determined. For a textured HCP polycrystal, the only practical way to determine the material parameters are by fitting numerical simulations based on the polycrystal plasticity model to the corresponding experimental data(Xu *et al.*, 2008). By introducing more constrains, the number of suitable parameter combinations can be significantly reduced, which can lead to a better predictive capability. An efficient

way to tune polycrystal plasticity models is to obtain material parameters by not only fitting the macroscopic stress-strain curves and deformation textures, but also simultaneously fitting elastic lattice strains measured by in-situ neutron diffraction. However, using both the macroscopic and microscopic quantities to determine material parameters is very time consuming. Therefore, a genetic algorithm approach is developed to optimize material parameters, in an effort to improve the agreement between predictions from polycrystalline plasticity models and experimental data.

The purpose of this research is to develop a method that can significantly simplify the human work in determining the material parameters of polycrystal plasticity models.

1.2 Thesis outline

The thesis is composed of seven chapters:

In this Chapter, the background of this thesis have been illustrated.

Chapter 2: Literature Review.

Chapter 3: A brief introduction of the genetic algorithm approach.

Chapter 4: Study of magnesium alloy ZEK100 under tension and compression in different orientations.

Chapter 5: Study of magnesium alloy with random texture under tension and compression.

Chapter 6: Study of rolled magnesium AZ31 alloy under uniaxial compression and plane strain compression.

Chapter 7: General conclusions.

Chapter 2

Literature review

2.1 Overview of magnesium

Magnesium, known as the ninth most abundant element in the universe and third most commonly used structural metal. It is used extensively by many industrial products and has attracted the interest of many researchers in recent years. Magnesium is well known as one of lightweight metals. On average, magnesium is 35% lighter than aluminum and 80% lighter than steel per volume. The advantages of magnesium alloys, low density, high strength and great workability, lead to their use in automobile, aircraft and electronics.

The application of magnesium alloys traces back to as early as World War I. It was used to build German military aircraft. But the application of magnesium in the commercial aerospace industry was generally restricted to engine-related components, due to magnesium parts have tendency to corrode and creep at high temperatures. Currently, the use of magnesium alloys in aerospace is increasing, mostly driven by the increasing importance of fuel economy and the need to reduce weight. In automobile manufacturing, using magnesium alloys is one of best ways on vehicle weight reduction. Car manufacturers use magnesium alloys on crankcase, wheels and other parts. However, knowledge of aluminum and steel is far more advanced than that of magnesium.

Magnesium alloys are mixtures of magnesium with other elements, often aluminum, zinc, manganese, silicon, copper, rare earths and zirconium.

The designation system for magnesium alloys follow a system using one or two prefix letters, two or three numerals, and a suffix letter. The prefix letters designate the two principal alloying metals according to the following format developed in ASTM specification B275 (De Garmo *et al.*, 2011): A = Aluminium, E = Rare Earths, K = Zirconium, M = Manganese, S = Silicon, Z = Zinc. The numerals correspond to the rounded-off percentage of the main alloy elements. Marking AZ31 for example conveys magnesium alloy with roughly 3 weight percent aluminium and 1 weight percent zinc.

In this thesis, the research focuses on three types of magnesium alloys, magnesium ZEK100 sheet, cast magnesium alloy with random texture and rolled magnesium AZ31 plate.

The density of magnesium is near $1.738g/cm^3$, which is lower than aluminium and iron. The melting point of magnesium is $650^\circ C$. Unfortunately, magnesium alloys tend to corrode too easily, that lead to the used of magnesium less than aluminium and iron.

At room temperature, crystal structure of magnesium alloys is hexagonal close-packed(HCP), presented in Figure 2.1. Plastic deformation of the hexagonal lattice is more complicated than in cubic latticed metals like steel and aluminium. The anisotropic material properties (thermal, elastic, and plastic) are due to the polycrystalline texture and intergranular stresses. The anisotropy of the polycrystalline material is caused by the anisotropic properties of the single crystal (i.e., the c-axis shown in Figure 2.1 has different properties than the a-axis) combine with texture. The c/a ratio at room temperature is 1.624, smaller than the theoretical value for incompressible sphere model, 1.633. That leads to restricted number of deformation slip and twinning modes.

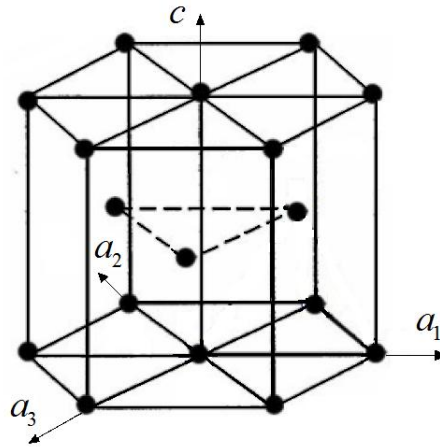


Figure 2.1: HCP single crystal structure.

2.2 Deformation of HCP metals

The deformation of HCP metals can be separated into elastic deformation and plastic deformation. In this section, the elastic behavior and possible slip and twinning systems will be discussed.

2.2.1 Elastic behavior

For isotropic material, the stress increases linearly with respect elastic strain before yield point. That is the Hooke's Law:

In normal stress:

$$\sigma = E\varepsilon \quad (2.1)$$

In shear stress

$$\tau = G\gamma \quad (2.2)$$

Where, σ and τ are normal stress and shear stress, ε and γ are normal strain and

shear strain, E and G are elastic modulus (Young's Modulus) and shear modulus.

The relation of E and G is:

$$G = \frac{E}{2(1 - \nu)} \quad (2.3)$$

For anisotropy crystal, elastic modules in different direction are different. The elastic behavior can be describe as generalized Hooke's law:

$$\begin{bmatrix} \sigma_{11} \\ \sigma_{22} \\ \sigma_{33} \\ \sigma_{12} \\ \sigma_{13} \\ \sigma_{23} \end{bmatrix} = \begin{bmatrix} C_{11} & C_{12} & C_{13} & C_{14} & C_{15} & C_{16} \\ C_{21} & C_{22} & C_{23} & C_{24} & C_{25} & C_{26} \\ C_{31} & C_{32} & C_{33} & C_{34} & C_{35} & C_{36} \\ C_{41} & C_{42} & C_{43} & C_{44} & C_{45} & C_{46} \\ C_{51} & C_{52} & C_{53} & C_{54} & C_{55} & C_{56} \\ C_{61} & C_{62} & C_{63} & C_{64} & C_{65} & C_{66} \end{bmatrix} \begin{bmatrix} \varepsilon_{11} \\ \varepsilon_{22} \\ \varepsilon_{33} \\ \varepsilon_{12} \\ \varepsilon_{13} \\ \varepsilon_{23} \end{bmatrix} \quad (2.4)$$

Where σ_{ij} ε_{ij} are stress vector and elastic strain vector, C_{ij} is elastic stiffness tensor.

Due to the symmetry of HCP structure, the number of independent elastic constants is reduced to 5. Equation 2.4 can be simplified as:

$$\begin{bmatrix} \sigma_{11} \\ \sigma_{22} \\ \sigma_{33} \\ \sigma_{23} \\ \sigma_{31} \\ \sigma_{12} \end{bmatrix} = \begin{bmatrix} C_{11} & C_{12} & C_{13} & 0 & 0 & 0 \\ C_{12} & C_{11} & C_{13} & 0 & 0 & 0 \\ C_{13} & C_{13} & C_{33} & 0 & 0 & 0 \\ 0 & 0 & 0 & C_{44} & 0 & 0 \\ 0 & 0 & 0 & 0 & C_{44} & 0 \\ 0 & 0 & 0 & 0 & 0 & (C_{11} - C_{12})/2 \end{bmatrix} \begin{bmatrix} \varepsilon_{11} \\ \varepsilon_{22} \\ \varepsilon_{33} \\ 2\varepsilon_{23} \\ 2\varepsilon_{31} \\ 2\varepsilon_{12} \end{bmatrix} \quad (2.5)$$

2.2.2 Slip

There are two prominent mechanisms of plastic deformation, namely slip and twinning. Slip is the prominent mechanism of plastic deformation in metals. It involves sliding of blocks of crystal over one other along definite crystallographic planes, called slip planes. The slip will be activated when applied resolved shear stress acting on this slip plane reaches a critical value, known as the critical resolved shear stress (CRSS).

A slip system describes the set of symmetrically identical slip planes and associated family of slip directions for which dislocation motion can easily occur and lead to plastic deformation. The slip planes are normally the planes with the highest density of atoms, and the slip directions are the directions in the slip plane that corresponds to one of the shortest lattice translation vectors

Different crystal structure has different slip system. FCC has 12 slip systems, and BCC has 48. There are six types of slip systems have been observed in HCP metals, listed in Table 2.1.

Slip system	Burgers vector type	Slip direction	Slip plane
1	a	$\langle 11\bar{2}0 \rangle$	$\{0001\}$
2	a	$\langle 11\bar{2}0 \rangle$	$\{10\bar{1}0\}$
3	a	$\langle 11\bar{2}0 \rangle$	$\{10\bar{1}1\}$
4	c+a	$\langle 11\bar{2}3 \rangle$	$\{11\bar{2}2\}$
5	c	$\langle 0001 \rangle$	$\{10\bar{1}0\}$
6	c	$\langle 0001 \rangle$	$\{11\bar{2}0\}$

Table 2.1: Independent slip systems in HCP metals (Partridge, 1967).

Poirier and Le Hazif (1976) have studied the slip systems in HCP metals based on transmission electron microscopy. They indicated that each HCP metal has primary slip system which is easily activated as well as one or more secondary systems which have significantly higher CRSS. Primary slip system of magnesium is the basal slip

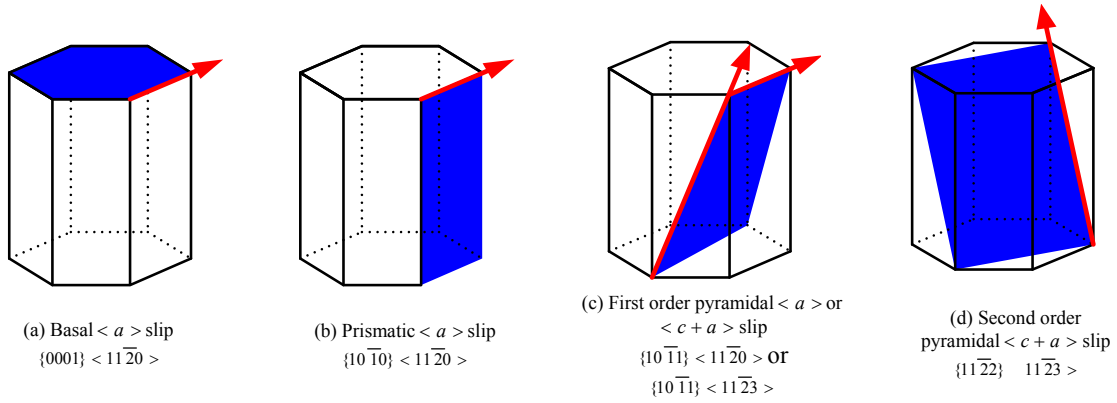


Figure 2.2: Frequently observed slip systems in magnesium at room temperature (Partridge, 1967).

$\{0001\} \langle 11\bar{2}0 \rangle$. Basal slip is the glide along the closed-packed direction ($\langle a \rangle$) and on the most closed-packed plane ($\{0001\}$ plane). It has lower CRSS than other slip systems.

Flynn *et al.* (1961) concluded that the prismatic $\langle a \rangle$ is more important than pyramidal $\langle a \rangle$ slip. In addition, as pointed by Agnew *et al.* (2001), the deformations and crystallographic textures induced by pyramidal $\langle a \rangle$ slip could be resulted from a combination of basal slip $\langle a \rangle$ and prismatic $\langle a \rangle$ slip. Therefore, pyramidal $\langle a \rangle$ slip is often not included in the crystal-based plastic analysis.

In magnesium alloys, deformation slips are accommodated by a combination of $\{0001\} \langle 11\bar{2}0 \rangle$ (or basal $\langle a \rangle$), $\{10\bar{1}0\} \langle 11\bar{2}0 \rangle$ (or prismatic $\langle a \rangle$), $\{11\bar{2}2\} \langle 11\bar{2}3 \rangle$ (or second-order pyramidal $\langle a + c \rangle$). Figure 2.2 presents the frequently observed slip systems in magnesium at room temperature.

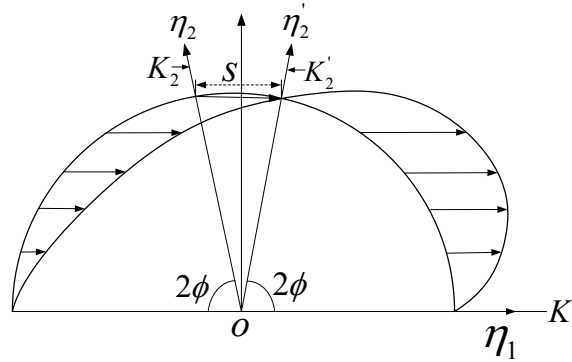


Figure 2.3: Crystallographic elements of twinning (Partridge, 1967).

2.2.3 Twinning

In addition to slip, twinning is another important mode of deformation mechanism in HCP materials. Twinning involves a homogeneous shear evenly distributed over a portion of the lattice such that the lattice orientation in the twinned region is a mirror image of the original lattice. The plastic strain is therefore accommodated by translation of a section of a crystal relative to another across a single twinning plane by an amount which is a multiple of Burgers vector. In addition, a twinning system can only activate in one direction, which is known as polarization. Twinning results in a sudden reorientation of the crystal lattice, whereas slip causes a much more gradual reorientation.

As Figure 2.3, a twin can be described by four elements: the first undistorted plane K_1 , the direction of shear η_1 , the second undistorted plane K_2 , and η_2 . The plane K_1 is the twin plane and remain unchanged during twinning. The shear direction of η_1 that lies in the plane K_1 is the direction where twinning occurs. The plane K_2 is displaced to K'_2 by the twinning shear γ . K_2 and K'_2 are the lines of intersection of the shear plane (normal to K_1 and K_2) with plane K_2 and K'_2 , respectively.

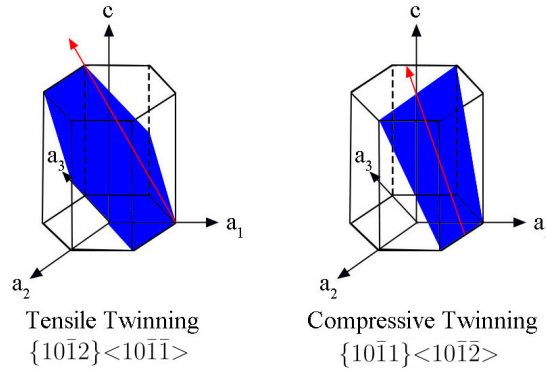


Figure 2.4: Twinning modes in magnesium at room temperature.

For magnesium alloys, which $c/a = 1.624$, the most predominate twinning mode at room temperature is $\{10\bar{1}2\}\langle 10\bar{1}\bar{1}\rangle$. This type of twinning is called “tensile” twinning or “extension” twinning, which elongates the c-axis. The twinning mode activates under a compressive stress along the c-axis is named as “compressive” twinning or “contraction” twinning $\{10\bar{1}1\}\langle 10\bar{1}\bar{2}\rangle$. Figure 2.4 presents this two twinning modes in magnesium at room temperature.

2.3 Deformation modeling

Crystal plasticity modelling is the simulation of plastic deformation in crystalline materials based on microscopic deformation mechanisms at crystal level (Battaini, 2008).

In polycrystal plasticity models, materials are considered as a composite composed of crystals or grains with a preferred orientation distribution, called crystallographic texture (Kocks *et al.*, 2000). The deformation of each grain is described by slip and twinning models in single crystal plasticity.

There are various homogenization schemes to describe the deformation of polycrystals. The most popular three are Taylor model (Taylor, 1938), Sachs model (Sachs, 1928), and Self Consistent model.

2.3.1 Homogenisation schemes

The earliest homogenisation scheme was proposed by Sachs (1928). This model assumes stress are equal and yielding occurs simultaneously in all the grains (Kocks *et al.*, 2000). This assumption turns out to be a lower bound of prediction. Moreover, it assumes only single slip in each of the grains and, consequently, the compatibility between the grains is impossible to achieve (Hosford, 1993; Taylor, 1938)

In contrast, Taylor model (Taylor, 1938), well known as upper bound model, assumes that strains are equal in all grains and ignores strains heterogeneity among grains. One of the assumption of the Taylor scheme is that at least five independent components of strain should be present to accommodate the change in shape with constant volume. This implies that the Taylor model neglects strain variations from grain to grain in the polycrystalline aggregate. It does not consider the interaction between crystals. Since high crystallographic symmetries in BCC and FCC materials, the interaction between crystal is less significant. Taylor model worked well in modeling of forming of aluminum and steel steets (Wu *et al.*, 1997; Dawson *et al.*, 2003; Eyckens *et al.*, 2009; Lévesque *et al.*, 2010). However, Taylor model may cause high stress concentration and further activate unexpected mechanisms with large CRSS in HCP metals. Consequently, polycrystal plasticity models based on the self-consistent approach originally proposed by Kröner (1958), for the elastic case and later extended to the elastoplastic (Hill, 1965) and viscoplastic (Hutchinson, 1976),

are becoming more popular than the Taylor model when modeling HCP polycrystals.

Another popular homogenisation schemes is Self-consistent(SC) scheme. It was propose by Kröner (1958). It is proved that the self-consistent approach is more suitable than the classic Taylor model for modeling the mechanical behavior of HCP polycrystals (Hill, 1965, 1967; Hutchinson, 1970). In general, self-consistent models allow for different strain response in each grain. The strain depends on the relative stiffness between the grain and a surrounding homogeneous equivalent medium (HEM). The consistency conditions require that the averaged behavior over all the grain must be the same as the macroscopically imposed one. Interaction between the inclusion and the HEM is obtained with the solution of local stress equilibrium equations. The SC schemes has been developed to take into account interaction between two or more grains. (Lebensohn and Canova, 1997; Lebensohn *et al.*, 1997; Canova, 1994; Solas and Tomé, 2001). Consequently, the results of multi-phase materials can be promoted. SC schemes consist of many subtypes with different mathematical assumptions. Such as ‘affine’, ‘secant’, ‘tangent’ and ‘neff = 10’

Various SCSs have been evaluated by comparing their predictions, including mechanical responses and texture evolutions, with finite element calculations and full field simulations or available experimental evidence for polycrystals (e.g., Molinari and Tóth (1994); Tomé (1999); Lebensohn *et al.* (2007)). It has been found that Secant and Tangent SCSs, among the first-order SCSs, exhibit asymptotic trend to respectively the upper-bound and lower-bound in the rate-insensitive limit. Therefore, they are not appropriate for highly anisotropic materials like HCP polycrystals. The intermediate SCSs, Affine and Neff give better overall predictions, if appropriate artificial parameter Neff is assigned according to results of finite element calculations

(Molinari and Tóth, 1994) or relative directional compliance approach (Tomé, 1999). It has to be noted that these evaluations are based on the assumption that all the material parameters at single crystal level are the same for various SCSs.

The visco-plastic self-consistent (VPSC) model, proposed by Lebensohn and Tomé (1993) has been employed to investigate the large deformation behavior of polycrystal materials, including uniaxial tension and compression, plane strain loading and simple shear. (Lebensohn *et al.*, 1996; Agnew and Duygulu, 2005; Proust *et al.*, 2007, 2009; Xu *et al.*, 2009; Wang *et al.*, 2010b).

Turner and Tomé (1994) proposed an elasto-plastic self-consistent(EPSC) model. The EPSC model works only for small deformation and earlier EPSC models did not include texture evolution associated with slip or twinning. The model has been employed to investigate the deformation mechanisms of HCP metals via the interpretation of elastic lattice strain results(Agnew *et al.*, 2003, 2006; Xu *et al.*, 2008). Clausen *et al.* (2008) extended the EPSC model by including texture development and stress relaxation due to twinning, while Neil and Agnew (2009) developed a large strain EPSC model to approximately account for the kinematics of large strain, rigid body rotations, texture evolution and grain shape evolution. Máthis *et al.* (2015) employed such models to study the effect of loading mode on the evolution of the deformation mechanisms in randomly textured magnesium polycrystals. Recently, based on the framework of EPSC model, Zecevic *et al.* (2015) proposed a multi-scale EPSC model with hardening based on dislocation density, twinning and de-twinning. However, the rate-insensitive character of the constitutive law upon with the EPSC model is based on prevents us from addressing strain rate-sensitivity, and the experimentally observed stress relaxation and creep associated with finite hold times for

acquisition of lattice-strain data.

Wang *et al.* (2010c) developed a finite strain Elasto-Viscoplastic Self-Consistent (EVPSC) model for polycrystalline materials. The proposed EVPSC model is a general rate-sensitive self-consistent polycrystal plasticity model valid at arbitrarily large deformations. The EVPSC model has been successfully applied to analyze the deformation mechanisms of HCP metals (Wang *et al.*, 2010a,b,d, 2011, 2012b; Guo *et al.*, 2013; Qiao *et al.*, 2015a). A twinning and detwinning model (TDT) has been proposed by Wang *et al.* (2010b, 2013a) and implemented into the EVPSC model. The EVPSC-TDT model has been applied to simulate the deformation mechanisms associated with the twinning/detwinning behavior for HCP metals under monotonic/cyclic loading (Wang *et al.*, 2013c, 2015; Lee *et al.*, 2014; Wu *et al.*, 2014; Guo *et al.*, 2015a,b; Qiao *et al.*, 2015b).

2.3.2 Twinning models

In addition to slip, twinning is another important deformation mechanism in HCP materials, especially in accommodating the c-axis strain. Twinning model is used to account for the formation of twins, which needs to be designed in a manner considering computational efficiency. In this thesis, several popular twinning models which are usually adopted by researchers will be introduced.

Firstly, the predominant twin reorientation (PTR) model (Tomé *et al.*, 1991; Van Houtte, 1978; Lebensohn and Tomé, 1993) is one of the most popular twinning model. In PTR model, the volume fractions of all twinning systems in each grain are tracked during deformation process. When an accumulated volume fraction of a twin system exceeds a threshold value, that corresponding grain will be fully reoriented.

That twin system with an exceeding volume fraction is called the predominant twin system (PTS) and determines the reorientation of the grain. The threshold value will be updated after each reorientation at each step. This model performs very well, when one twin system prevails in the grains. However, similar activities of different twinning systems may lead to unrealistic results by this model.

The second is the volume fraction transfer (VFT) scheme. This scheme describes the initial texture using volume fractions in a regular grid of orientations in Euler space and the change of volume fractions is used to represent the reorientation process. In this way, the real quantitative status of twinning can be modelled explicitly. However, the history of deformation will be lost. The two twinning schemes above are mainly employed in the simulation work of magnesium.

Subsequently, a sophisticated composite grain (CG) model for describing twinning has been proposed by Tomé and Kaschner (2005) and Proust *et al.* (2007) based on the lamellar grain model of Lebensohn (1999). The CG model accounts for the twin shape and twin-parent interaction, and was implemented in the VPSC code and applied to address the role of twinning during strain path changes in Zr. The CG model has been extended to include de-twinning when studying magnesium subjected to strain path changes (Proust *et al.*, 2009). In the early version of CG model (Proust *et al.*, 2007) the continuity of the shear stress parallel to the twin interface was enforced in order to deal with the laminar twin structure in magnesium. When grown-up twins are assumed to coalesce and become separate inclusions, the continuity of the shear stress across twin boundaries was relaxed in studying the mechanical response of Mg. Recently, one major development of CG model is that the empirical twin nucleation model used in Refs. Proust *et al.* (2007, 2009) has been updated with newly developed

physics-based nucleation models (Capolungo *et al.*, 2009; Beyerlein and Tomé, 2010) that are inspired by atomistic simulations (Wang *et al.*, 2010d; Tomé *et al.*, 2011) and experiments (Aydiner *et al.*, 2009). For what follows, it is important to notice that the CG model assumes that twin growth accommodates strains inside the un-twinned domain (matrix) and is driven by the average stress in the matrix, while de-twinning accommodates strain inside the twin domain and is driven by the average stress in the twin. This treatment assigns the contribution of plastic deformation that results from twinning or de-twinning to either the matrix or the twin domains, respectively, rather than assigning the plastic deformation to the composite entity formed by both the matrix and twin domains.

To overcome this shortage, the model that been used here will adopt both the average stresses in the matrix and in the twin to calculate the twin growth and the twin shrinkage (de-twinning). In addition, the continuity of stress across the twin interface was relax in the present model, and both parent and twin are treated as separate inclusions from the start. As a consequence, the model is not strictly a composite grain one, and allows accounting for more than one twin variant per grain. Thus the model develop a physics-based crystal plasticity model including twinning and de-twinning, correspondingly named TDT (Wang *et al.*, 2012a), to study plastic deformation of HCP metals during cyclic loading and strain path changes. In the TDT model, the growth of twinning and de-twinning processes of twin system α are represented by four “operations” (A, B, C, D). The twin volume fractions of α due to each of the operations are tracked and used to obtain the total twin volume fraction of α . A threshold value for termination of reorientation by twinning is defined with accumulated twin fraction and effective twinned fraction (volume fraction of twin

terminated grains). After the comparison between total twin volume fraction and threshold value, a decision with regard to reorientation of the twinned area can be made. It is worth noting that no additional parameter for de-twinning is introduced in this model.

Chapter 3

Genetic algorithm approach

It has been noticed that the current polycrystal plasticity models with slip and twinning, including the VPSC and EVPSC, involve a large number of material parameters, which may not be uniquely determined. For a textured HCP polycrystal, the only practical way to determine the material parameters is by fitting numerical simulations based on the polycrystal plasticity model to the corresponding experimental data. By introducing more constraints, the number of suitable parameter combinations can be significantly reduced, which can lead to a better predictive capability.

However, using both the macroscopic and microscopic quantities to determine material parameters is very time consuming, and the traditional trial-and-error approach is also not appropriate in this case. Therefore, a genetic algorithm approach is developed to optimize material parameters, in an effort to improve the agreement between predictions from polycrystalline plasticity models and experimental data.

3.1 Introduction of genetic algorithm

In the field of artificial intelligence, genetic algorithm (GA) is a search heuristic that mimics the process of natural selection. It is a method for solving optimization problems using technique inspired by natural evolution. It became widely used for practical problem solving and for scientific modeling.

The basic genetic algorithm includes three types of operations: selection, crossover and mutation.

Selection This operator selects individual in the population for reproduction. The fitter the genes, the more chance it is likely to be selected.

Crossover After selection operator, this operator is the process of creating an individual for generation $(n + 1)$ from two individuals in generation n . In data fitting case, if the parents individuals in generation n with parameter sets of (a_1, a_2, \dots, a_i) and (b_1, b_2, \dots, b_i) , after crossover process, the new individual for generation $(n + 1)$ has parameters as:

$$[\alpha_1 a_1 + (1 - \alpha_1) b_1, \alpha_2 a_2 + (1 - \alpha_2) b_2, \dots, \alpha_i a_i + (1 - \alpha_i) b_i] \quad (3.1)$$

Where $\alpha_1, \alpha_2, \dots, \alpha_i$ are random real numbers between 0 and 1.

Mutation This operator is similar to biological mutation. It randomly flips some of the bits in a chromosome and lead to some gene of children is different from their parents. If a mutation was added to the crossover example parameter set 3.1, a possible new result is:

$$[\alpha_1 a_1 + (1 - \alpha_1) b_1, \alpha_2 a_2 + (1 - \alpha_2) b_2, \dots, x_k, \dots, \alpha_i a_i + (1 - \alpha_i) b_i] \quad (3.2)$$

x_k is a new gene which does not come from parents genes.

Mutation is important in that it maintains a level of diversity amongst individuals of the same generation, which is useful in helping the GA to avoid becoming trapped in a region of the parameter space that is only locally optimal.

A simple genetic algorithm for data fitting works as follows(Mitchell, 1998):

1. Start with a randomly generated population of n sets of parameter, each of them contain i parameters.

2. Calculate the fitness ($f(x)$) of each parameter set x in the population.
3. Repeat the following steps until n offspring have been created:
 - (a) Select a pair of parent chromosomes from the current population, the probability of selection being an increasing function of fitness. Selection is done "with replacement," meaning that the same chromosome can be selected more than once to become a parent.
 - (b) With probability p_c (the "crossover probability" or "crossover rate"), cross over the pair at a randomly chosen point (chosen with uniform probability) to form two offspring. If no crossover takes place, form two offspring that are exact copies of their respective parents. (Note that here the crossover rate is defined to be the probability that two parents will cross over in a single point. There are also "multipoint crossover" versions of the GA in which the crossover rate for a pair of parents is the number of points at which a crossover takes place.)
 - (c) Mutate the two offspring at each locus with probability p_m (the mutation probability or mutation rate), and place the resulting chromosomes in the new population. If n is odd, one new population member can be discarded at random.
4. Replace the current population with the new population.
5. Go to step 2.

3.2 Procedure of genetic algorithm approach

Mostly, determining parameter with EVPSC model is done manually and used traditional trial-and-error approach. However, the traditional method is very time consuming. The benefit of genetic algorithm is obvious. Computing power of computer is increasing rapidly. It is a general trend to use computer instead of man to do boring work such as the determination of parameters. It is obvious that a computer can easily replace human work. Genetic algorithm is a basic and effective method for solving optimization problems, which can be use in determining material parameters involved in polycrystal plasticity models.

The procedure of genetic algorithm is straight forward. As stated in the previous section, the genetic algorithm can be simple as two part: calculating fitness and generating next generation.

A fitness function needs to be define to calculate the fitness for each individual. The fitness was define as the difference between the simulated curve and the actual experimental curve. The smaller fitness value means the fitting is better.

$$Fitness = \sum \text{distance (sim,exp)}$$

The process stop when the highest ranking solution's fitness is reaching or has reached a plateau such that successive iterations no longer produce better results. That means the average relative change in the best fitness function value between old and new generation satisfy:

$$\frac{Fitness_{old} - Fitness_{new}}{Fitness_{old}} < 10^{-3}$$

The procedure flow chart of genetic algorithm is shown in Figure 3.1. At first, the GA program creates the first generation of individuals randomly. For each individual in the current generation k , it runs the EVPSC program to get a simulation result. The simulation result is compared with the experimental result to calculate fitness. If it does not reach the termination, the new generation $k + 1$ is created by crossover of generation k and the loop continues.

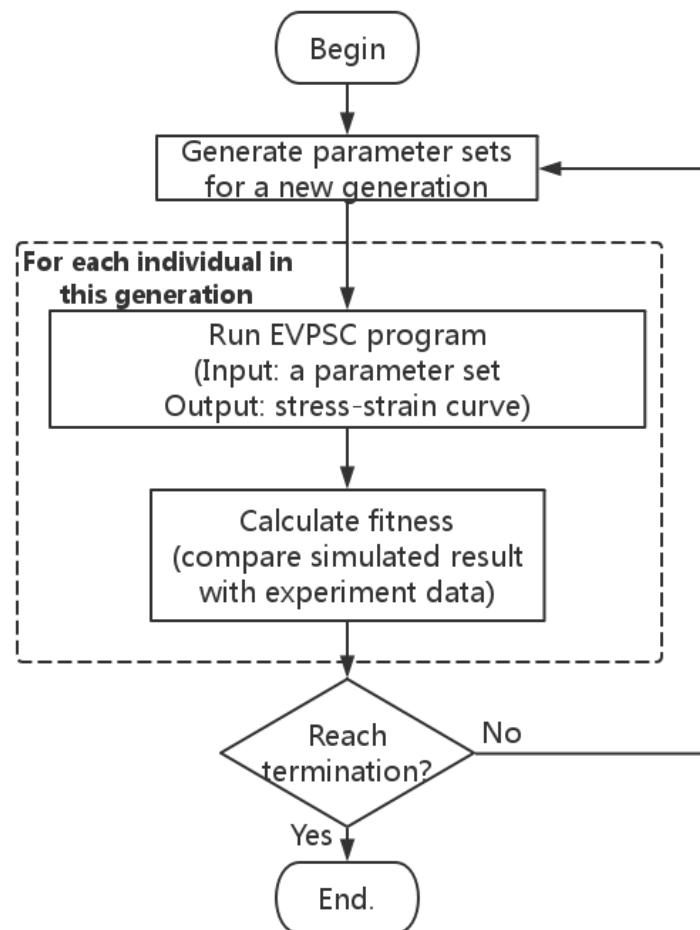


Figure 3.1: Procedure of genetic algorithm approach.

Chapter 4

Study of magnesium alloy ZEK100 under tension and compression in different orientations

4.1 Introduction

Magnesium alloys are widely used as lightweight materials for aircraft and transportation industry in recent years because of its low density and relatively high strength. However, present applications of magnesium alloys are mostly limited to extruded and cast parts since magnesium sheet alloys have limited formability at room temperature which is due to the hexagonal close packed (HCP) structure of magnesium alloys. Because of the strong basal texture, magnesium alloys, such as AZ31, offer only a limited number of slip systems which are active at room temperature (Agnew and Duygulu, 2005; Lou *et al.*, 2007). It is proved that adding rare-earth elements such as Ce, Nd, Y and Gd can weaken the basal texture in order to improve the room temperature formability of rolled magnesium alloys (Bohlen *et al.*, 2007, 2010; Hantzsche *et al.*, 2010; Dreyer *et al.*, 2010). Experiments have shown that the improved texture of rare-earth alloyed ZEK100 sheet leads to enhanced formability as well as reduced mechanical anisotropy at room temperature.

Magnesium alloys have been thoroughly studied experimentally in terms of stress-strain behavior, development of texture and evolution of internal elastic strain, etc. The corresponding modeling studies have used either the Visco-Plastic Self-Consistent (VPSC) model (Lebensohn and Tomé, 1993) or the Elasto-Plastic Self-Consistent (EPSC) model (Turner and Tomé, 1994). In 2010, a large strain elasto-viscoplastic

self-consistent(EVPSC) model was developed by Wang *et al.* (2010c). The EVPSC model is a completely general elastic-viscoplastic, fully anisotropic, self-consistent polycrystal plasticity model. It has been proven that the EVPSC model is able to predict many aspects of the large strain behavior of HCP materials (Agnew and Duygulu, 2005; Clausen *et al.*, 2008; Guo *et al.*, 2013; Hutchinson *et al.*, 2012; Muránsky *et al.*, 2008, 2009; Neil and Agnew, 2009; Oppedal *et al.*, 2012; Xu *et al.*, 2008; Turner *et al.*, 1995; Wang *et al.*, 2010a,d, 2011, 2012a,b, 2013b; Wu *et al.*, 2012).

However, there are a large number of material parameters need to be determined for current polycrystal plasticity models, including VPSC and EVPSC. For a textured HCP polycrystal, the only practical way to determine the material parameters is by fitting numerical simulations to the corresponding experimental data(Xu *et al.*, 2008). The material parameters may not be uniquely determined. By introducing more constrains, the number of suitable parameter combinations can be significantly reduced, which can lead to a better predictive capability. But using the traditional trial-and-error approach to determine parameters are very time consuming. Furthermore, the more constrains are used, the more difficult to determine the parameter by traditional method. Therefore, a genetic algorithm approach is developed to optimize material parameters, in an effort to improve the agreement between predictions from polycrystalline plasticity models and experimental data.

In this chapter, genetic algorithm approach is used to determine material parameters for magnesium ZEK100 sheet in EVPSC-PTR model. The simulated result including stress-strain curves, R value and post-deformation textures is compared with experimental data.

4.2 Constitutive model

4.2.1 Crystal plasticity

The EVPSC model, developed by Wang *et al.* (2010c) is a completely general elastic-viscoplastic, fully anisotropic, self-consistent polycrystal model. It can be applied to large strains and any crystal symmetry. The model is based on the approximation proposed by Molinari *et al.* (1997) for treating the elasto-visco-plastic inclusion problem. Details of the model is briefly described here. The elastic constitutive equation for a crystal is:

$$\overset{\nabla}{\sigma}^* = \mathcal{L} : \dot{\epsilon}^e - \sigma \text{tr} \dot{\epsilon}^e \quad (4.1)$$

where \mathcal{L} is the fourth order elastic stiffness tensor, $\dot{\epsilon}^e$ is the elastic strain rate tensor and $\overset{\nabla}{\sigma}^*$ is the Jaumann rate of the Cauchy stress σ based on the lattice spin tensor \boldsymbol{w}^e . The single crystal elastic anisotropy is included in \mathcal{L} through the crystal elastic constants C_{ij} (Wang and Mora, 2008).

The plastic deformation of a crystal is assumed to be due to crystallographic slip and twinning on crystallographic systems $(\boldsymbol{s}^\alpha, \boldsymbol{n}^\alpha)$. Here, \boldsymbol{s}^α and \boldsymbol{n}^α are, respectively, the slip/twinning direction and the normal to the slip/twinning plane for system α . The following equation gives the grain (crystal) plastic strain rate, $\dot{\epsilon}^p$ (see e.g., Asari and Needleman, 1985) :

$$\dot{\epsilon}^p = \sum_{\alpha} \dot{\gamma}^{\alpha} \boldsymbol{P}^{\alpha} \quad (4.2)$$

in terms of the shear rate $\dot{\gamma}^{\alpha}$ and the Schmid tensor $\boldsymbol{P}^{\alpha} = (\boldsymbol{s}^{\alpha} \boldsymbol{n}^{\alpha} + \boldsymbol{n}^{\alpha} \boldsymbol{s}^{\alpha})/2$ for system α . For both slip and twinning, the driving force for shear rate $\dot{\gamma}^{\alpha}$ is the resolved shear stress $\tau^{\alpha} = \boldsymbol{\sigma} : \boldsymbol{P}^{\alpha}$, where $\boldsymbol{\sigma}$ is the Cauchy stress tensor.

For slip,

$$\dot{\gamma}^\alpha = \dot{\gamma}_0 |\tau^\alpha / \tau_{cr}^\alpha|^{\frac{1}{m}} \text{sign}(\tau^\alpha) \quad (4.3)$$

Where $\dot{\gamma}_0$ is a reference shear rate, τ_{cr}^α is the Critical Resolved Shear Stress (CRSS), and m is the strain rate sensitivity. Due to its polar nature, the shear rate due to twinning is described by:

$$\dot{\gamma}^\alpha = \begin{cases} \dot{\gamma}_0 |\tau^\alpha / \tau_{cr}^\alpha|^{\frac{1}{m}} & \tau^\alpha > 0 \\ 0 & \tau^\alpha \leq 0 \end{cases} \quad (4.4)$$

For both slip and twinning, the evolution of the critical resolved shear stress (CRSS) τ_{cr}^α as deformation processed is given by:

$$\dot{\tau}_{cr}^\alpha = \frac{d\hat{\tau}^\alpha}{d\gamma_{ac}} \sum_{\beta} \mathbf{h}^{\alpha\beta} \dot{\gamma}^\beta \quad (4.5)$$

Where γ_{ac} is the accumulated shear strain in the grain, and $\mathbf{h}^{\alpha\beta}$ are the latent hardening coupling coefficients, which empirically account for the obstacles on system α associated with system β . $\hat{\tau}^\alpha$ is the threshold stress, described here by an extended Voce law (Tome *et al.*, 1984):

$$\hat{\tau}_0^\alpha = \tau_0^\alpha + (\tau_1^\alpha + h_1^\alpha \gamma_{ac}) (1 - \exp(-\frac{h_0^\alpha}{\tau_1^\alpha} \gamma_{ac})) \quad (4.6)$$

Here, τ_0 , h_0 , h_1 and $\tau_0 + \tau_1$ are the initial CRSS, the initial hardening rate, the asymptotic hardening rate, and the back-extrapolated CRSS, respectively.

The response of a polycrystal comprised of many grains is obtained using a self-consistent approach: each grain is treated as an ellipsoidal inclusion embedded in

a homogeneous effective medium (HEM), which represents the aggregate of all the grains. Interactions between each grain and the HEM are described using the Eshelby inclusion formalism (Eshelby, 1957). The behaviour of the inclusion (single crystal) and HEM (polycrystal) can be linearized as follows:

$$\dot{\boldsymbol{\epsilon}} = \mathbf{M}^e : \dot{\boldsymbol{\sigma}} + \mathbf{M}^\nu : \boldsymbol{\sigma} + \dot{\boldsymbol{\epsilon}}^0 \quad (4.7)$$

$$\dot{\mathbf{E}} = \overline{\mathbf{M}}^e : \dot{\boldsymbol{\Sigma}} + \overline{\mathbf{M}}^\nu : \boldsymbol{\sigma} + \dot{\mathbf{E}}^0 \quad (4.8)$$

Here, \mathbf{M}^e , \mathbf{M}^ν , $\dot{\boldsymbol{\epsilon}}$, $\boldsymbol{\sigma}$ and $\dot{\boldsymbol{\epsilon}}^0$ are, respectively, the elastic compliance, the viscoplastic compliance, the strain rate, the true stress, and the back-extrapolated strain rate for the grain. $\overline{\mathbf{M}}^e$, $\overline{\mathbf{M}}^\nu$, $\dot{\mathbf{E}}$, $\boldsymbol{\Sigma}$ and $\dot{\mathbf{E}}^0$ are the corresponding terms for the HEM. Equations 4.7 and 4.8 can be written in component form as follows:

$$\dot{\epsilon}_{ij} = M_{ijkl}^e \dot{\sigma}_{kl} + M_{ijkl}^\nu \sigma_{kl} + \dot{\epsilon}_{ij}^0 \quad (4.9)$$

$$\dot{E}_{ij} = \overline{M}_{ijkl}^e \dot{\Sigma}_{kl} + \overline{M}_{ijkl}^\nu \Sigma_{kl} + \dot{E}_{ij}^0 \quad (4.10)$$

The grain-level stress and strain rates are related self-consistently to the corresponding values for the HEM (Turner and Tomé, 1994; Wang *et al.*, 2010c):

$$(\dot{\boldsymbol{\epsilon}} - \dot{\mathbf{E}}) = -\tilde{\mathbf{M}}^e : (\dot{\boldsymbol{\sigma}} - \dot{\boldsymbol{\Sigma}}) - \tilde{\mathbf{M}}^\nu : (\boldsymbol{\sigma} - \boldsymbol{\Sigma}) \quad (4.11)$$

where $\tilde{\mathbf{M}}^e$ and $\tilde{\mathbf{M}}^\nu$ are the interaction tensors that can be given by:

$$\tilde{\mathbf{M}}^e = (\mathbf{I} - \mathbf{S}^e)^{-1} : \mathbf{S}^e : \overline{\mathbf{M}}^e$$

$$\tilde{\mathbf{M}}^\nu = (\mathbf{I} - \mathbf{S}^\nu)^{-1} : \mathbf{S}^\nu : \overline{\mathbf{M}}^\nu$$

Where \mathbf{S}^e and \mathbf{S}^ν are the elastic and visco-plastic Eshelby tensors for a given grain, respectively, and \mathbf{I} is the identity tensor.

The response of a polycrystal comprised of many grains is obtained by applying the self-consistent approach. Various self-consistent schemes have been proposed. Wang *et al.* (2010c) have demonstrated that the predicted response of a polycrystal is very sensitive to the self-consistent scheme employed. Wang *et al.* (2010b) have evaluated various self-consistent schemes used in self-consistent modeling by applying them to the large strain behavior of magnesium alloy AZ31B sheet under different deformation processes. It was found that the Affine self-consistent scheme gave the best overall performance among the self-consistent approaches examined. Therefore, the Affine self-consistent scheme is employed in the present study.

The affine method (Masson *et al.*, 2000; Lebensohn *et al.*, 2004) assumes a higher compliance and will have a higher strain heterogeneity compared to the secant method. The Affine method employs the same formulation for the grain compliance as the Tangent method, but keeps the back extrapolated term in the local/global relation between strain rate and stress, which provides a harder inclusion/matrix interaction than the Tangent model as the rate sensitivity m decreases. The Affine method applies the following linearization:

$$\mathbf{M}^{\nu,\text{aff}} = \frac{\dot{\gamma}_0}{\mathbf{m}} \sum_{\alpha} \left(\frac{\tau^{\alpha}}{\tau_{cr}^{\alpha}} \right)^{\frac{1}{m}-1} \frac{\mathbf{P}^{\alpha} \mathbf{P}^{\alpha}}{\tau_{cr}^{\alpha}}, \dot{\varepsilon}^{0,\text{aff}} = \left(1 - \frac{1}{m}\right) \dot{\varepsilon}^p \quad (4.12)$$

For details concerning the self-consistent equations associated with the different visco-plastic self-consistent algorithms, one can refer to (Lebensohn *et al.*, 2007)

4.2.2 Twinning model

To model twinning, the Predominant Twin Reorientation (PTR) scheme proposed by Tomé *et al.* (1991) is used. PTR prevents grain reorientation by twinning until a threshold volume fraction A^{th1} is accumulated in any given system and rapidly raises the threshold to a value around $A^{th1} + A^{th2}$. Secondary twinning is not allowed in the PTR model and grain size effects on twinning are not explicitly modeled.

The PTR model works as follows: within each grain, g , the PTR model keeps track of the shear strain, $\gamma^{t,g}$, contributed by each twin system t , and of the associated volume fraction $V^{t,g} = \gamma^{t,g}/S^t$ as well (S^t is the characteristic twin shear). Crystallographically equivalent twins belong to the same twin mode. For example, the $\{10\bar{1}2\}$ twinning systems, which are activated by c-axis tension, constitute the tensile twin mode. The sum over all twin systems associated with a grain twin mode, and over all grains, represents the accumulated twin fraction, $\mathbf{V}^{acc,mode}$, in the aggregate for the particular twin mode (measured by SEM).

$$\mathbf{V}^{acc,mode} = \frac{\sum_g \sum_t \gamma^{t,g}}{S^t} \quad (4.13)$$

Since it is not numerically feasible to consider each twinned fraction as a new orientation, the PTR scheme adopts a statistical approach. At each incremental step, the scheme fully reorients some grains by twinning provided certain conditions are fulfilled. The effective twinned fraction, $\mathbf{V}^{th,mode}$, the volume associated with the fully reoriented grains for that mode, and the threshold volume fraction is defined as:

$$\mathbf{V}^{th,mode} = A^{th1} + A^{th2} \frac{\mathbf{V}^{eff,mode}}{\mathbf{V}^{acc,mode}} \quad (4.14)$$

After each deformation increment, a grain is randomly selected and the twin system with the highest accumulated volume fraction is identified. If it is larger than the threshold, $V^{\text{th,mode}}$, the grain is allowed to reorient and $V^{\text{eff,mode}}$ and $V^{\text{th,mode}}$ are updated. The process is repeated until either all grains are checked or until the effective twin volume exceeds the accumulated twin volume. In the latter case, reorientation by twinning ceases and the next deformation step is considered. This approach statistically solves the practical problem that the number of orientations would grow continually if each activated twinning system was represented by a new orientation. Additionally, it maintains the twinned volume fraction at a level that is consistent with the shear activity of the twins contributing to the deformation.

4.3 Genetic algorithm approach

Genetic algorithm is a widely used method for optimization problem and can be applied to many problems including data fitting. The theory of genetic algorithm is based on natural selection, the process that drives biological evolution. The genetic algorithm repeatedly modifies a population of individual solutions. At each step, the genetic algorithm selects individuals at random from the current population to be parents and uses them to produce the children for the next generation. Over successive generations, the population “evolves” toward an optimal solution.

While using genetic algorithm to determine the material parameters for magnesium ZEK100 sheet, a rough range was obtained by previous attempt. In order to narrow down the range to reduce the fitting time, the first step of genetic method approach is to determine the initial critical resolved shear stress (CRSS) τ_0 by fitting the yield stress.

In the first step, 20 individuals were used in each generation of genetic algorithm. The algorithm was allowed to run for a total of 30 generations. It took roughly 6 hours.

The first step generates a set of possible τ_0 for all 4 slip and twinning modes, The upper and lower bound of τ_0 can be narrow to a smaller range. The second step is determined all material parameters by fitting numerical simulation of stress-strain curves to the corresponding experimental data.

In this case, four deformation mechanisms are taken into account during modeling and are subsequently refined by the genetic algorithm approach: basal slip, prismatic slip, pyramidal slip and tensile twinning. As stated in the previous section, the parameters being adjusted for each slip and twinning system are initial CRSS τ_0 , the initial hardening rate θ_0 , the asymptotic hardening rate θ_1 , and the back-extrapolated CRSS τ_1 . According to previous attempt at fitting EVPSC output to this data set, latent hardening $h_{\alpha\beta}$ simplified as h_{st} , indicates only the effect of tensile twinning system t for each slip system s take into account. That reduces latent hardening coefficients from 16 to 4. The total number of free parameters is 22.

In the secondary fitting step of genetic algorithm approach, 100 individuals were used in each generation, and the algorithm was allowed to run for a total of 20 generations, resulting in a total of more than 1850 different parameter sets being run through the EVPSC-PTR model. It took roughly 3 days.

4.4 Results and discussion

The material considered in this chapter is a rolled Magnesium ZEK100 sheet, which previously studied by Kurukuri *et al.* (2014). The composition of this material is

1.3 wt pct Zn, 0.2 wt pct Nd, 0.25 wt pct Zr and 0.01 wt pct Mn, and the nominal thickness of the sheet is 1.6 mm. The pole figures of initial texture used in simulation are shown in Figure 4.1. The texture has 1944 grains ($10^\circ \times 10^\circ \times 10^\circ$ grid in Euler space) with independent orientations and weights. From the $\{0001\}$ and $\{10\bar{1}0\}$ pole figures presented in Figure 4.1, the ZEK100 sheet exhibits relatively weak basal texture, with significant spreading in the TD and a weak peak intensity.

The plastic deformation of Mg ZEK100 alloy is assumed to be due to basal ($\{0001\} \langle 11\bar{2}0 \rangle$), prismatic ($\{10\bar{1}0\} \langle 11\bar{2}0 \rangle$) and pyramidal $\langle \mathbf{a}+\mathbf{c} \rangle$ ($\{11\bar{2}2\} \langle 11\bar{2}3 \rangle$) slip as well as tensile twinning ($\{10\bar{1}2\} \langle 10\bar{1}1 \rangle$). In all the simulations in this chapter, the reference slip/twinning rate, $\dot{\gamma}_0$, and the rate sensitivity, m , are prescribed to be the same for all the slip/twinning systems: $\dot{\gamma}_0 = 0.001\text{s}^{-1}$ and $m = 0.05$, respectively. The room temperature elastic constants of the MgZn alloy are assumed to be close to those of pure Mg: $C_{11} = C_{22} = 58.0$; $C_{33} = 61.2$; $C_{12} = 25.0$; $C_{13} = C_{23} = 20.8$; $C_{44} = C_{55} = 16.6$; and $C_{66} = 16.5$ GPa (Simmons and Wang, 1971). Wang *et al.* (2010b) have evaluated several self-consistent approaches by studying the large strain behavior of magnesium alloy AZ31B sheet under tension and compression along different direction. It has been demonstrated that, of the approaches examined, the Affine self-consistent scheme gives the best overall performance. Therefore, all the simulations reported in this chapter are based on the Affine self-consistent scheme.

Tensile tests are performed in the rolling and transverse and at 45 deg to the rolling direction (designated herein as RD, TD, and 45°, respectively). Compression tests are performed in the rolling, transverse, 45 degree to RD and through-thickness (TT) directions. For both tension and compression, the strain rate is 0.001s. The stress strain results of this experiment reveal pronounced anisotropy in this material.

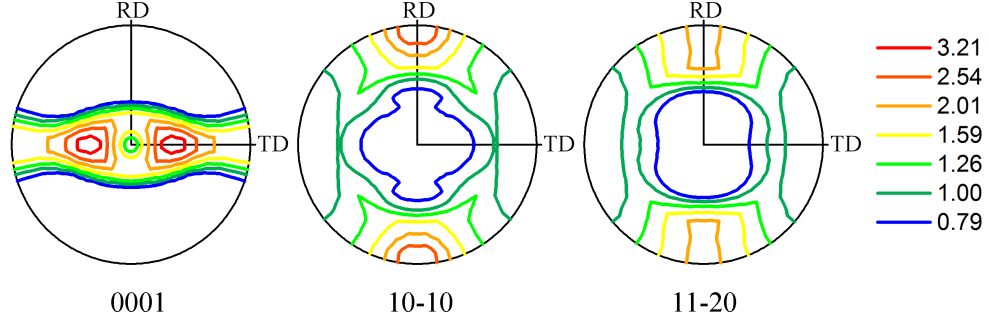


Figure 4.1: Initial texture of ZEK100 sheet represented in terms of the $\{0001\}$, $\{10\bar{1}0\}$ and $\{11\bar{2}0\}$ pole figures.

(Figure 4.2) It needs to be notice that the strain measured in experiment is plastic strain, but EVPSC model simulates both elastic and plastic deformation. The true strain is calculated as elastic strain plus plastic strain:

$$\varepsilon^{total} = \varepsilon^e + \varepsilon^p = \frac{\sigma}{Y} + \varepsilon^p \quad (4.15)$$

where Y is Young's modulus, which is 37MPa in this ZEK100 sheet.

Values of the hardening parameters are determined by using genetic algorithm approach fitting stress-strain curve under tension and compression along RD and compression along TT (RD-T, RD-C, and TT-C). The determined parameters associated with the EVPSC-PTR model are listed in Table 4.1.

Mode	τ_0 (MPa)	τ_1 (MPa)	θ_0 (MPa)	θ_1 (MPa)	h^{st}	A_1	A_2
Basal	11	2	110	20	2		
Prismatic	110	5	680	15	3		
Pyramidal	113	220	2070	90	3		
Tensile Twin	43	20	190	0	4	0.4	0.35

Table 4.1: List of material parameters for EVPSC-PTR constitutive model of ZEK100 sheet.

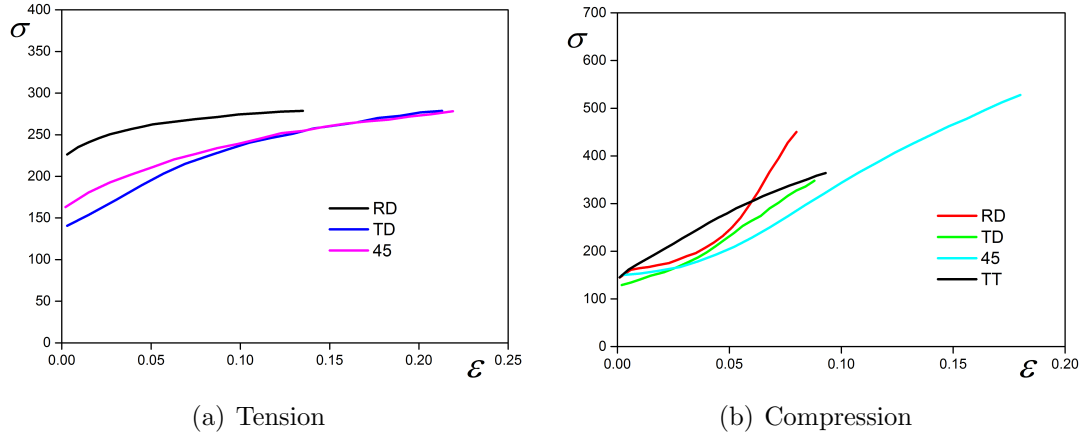


Figure 4.2: Stress - plastic strain curves of ZEK100 sheet in different orientations(Kurukuri *et al.*, 2014).

Figure 4.3-4.5 present the measured and fitted stress - strain curves and the relative activities of the various deformation mechanisms under uniaxial tension and compression along the RD (RD-T, RD-C), and under uniaxial compression along TT(TT-C), respectively. Figure 4.6-4.9 show the measured and predicted macroscopic stress-strain curves as well as the predicted relative activities of the various deformation mechanisms under tension and compression along TD and 45°.

Figure 4.3 shows that the experimental stress-strain curve under tension along the RD fitted by EVPSC-PTR model using genetic algorithm approach. The predicted relative activities of the various deformation mechanism are shown in Figure 4.3(b). Basal and prismatic slips are the primary and secondary deformation mechanisms under tension along RD. Because of the polar nature of the material, it is expected that tensile twinning is nearly inactive during uniaxial tension along the RD.

Figure 4.4 shows the measured and simulated macroscopic mechanical responses of the material under uniaxial compression along the RD. As shown in Figure 4.4(a), the stress-strain curve fit the experimental stress-strain curve very well. The predicted

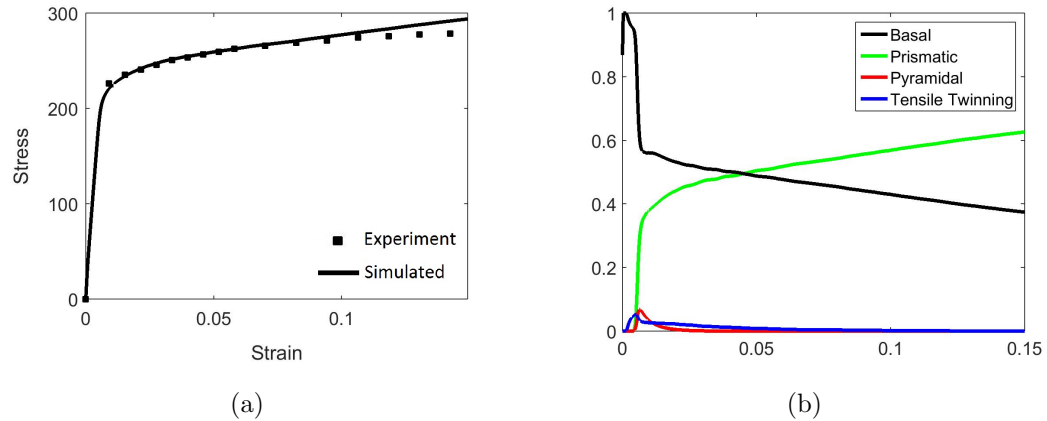


Figure 4.3: Fitted stress strain curves (a) and activities (b) under tension along RD (RD-T).

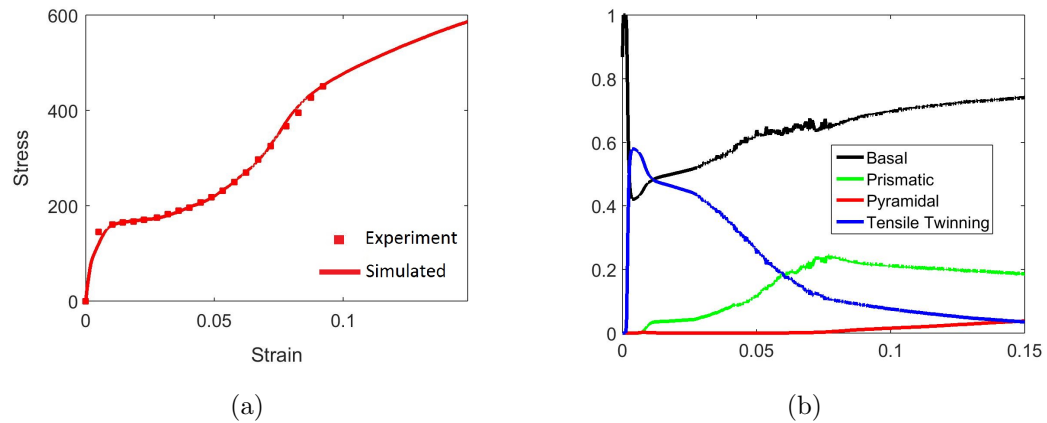


Figure 4.4: Fitted stress strain curves (a) and activities (b) under compression along RD (RD-C).

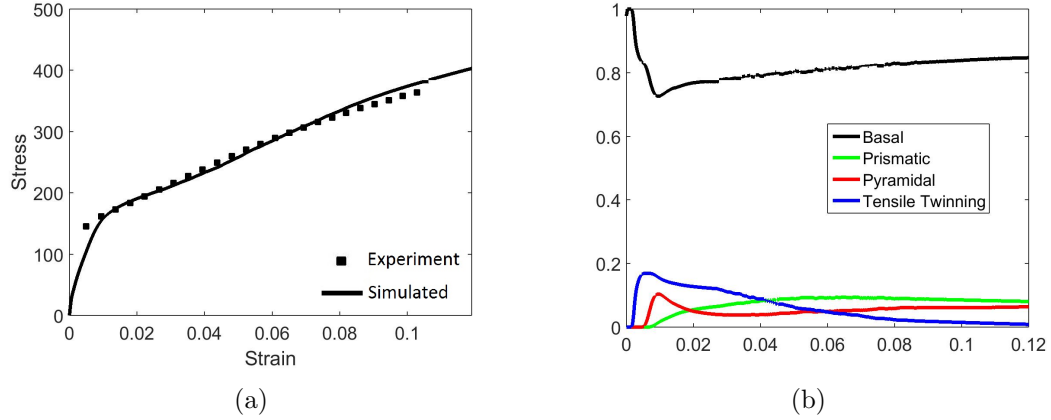


Figure 4.5: Fitted stress strain curves (a) and activities (b) under compression along TT (TT-C).

activities (Fig. 4.4(b)) show that the basal and prismatic slip are activated. Since the material has basal texture, tensile twinning can be easily activated by tension along c-axis. Therefore the relative activity of tensile twinning is found to be very active initially but then decreases gradually with further deformation. The predicted maximum twin volume fraction based on the PTR model is about 60%.

For uniaxial compression along the TT shows in Figure 4.5, it can be observed that the simulated result fitted the experimental stress-strain curves well. The stress and strain curve exhibits a typical slip dominated plastic deformation. The predicted activities in Fig. 4.5(b) show that the primary deformation mechanism is the basal slip. Very little Prismatic and Pyramidal slips activities are predicted by the model. Tensile twinning is noticeable but only at small strains.

Figure 4.6 and 4.7 show the measured and predicted stress-strain curve and activities of deformation mechanisms under tension and compression along TD. The predicted stress-strain curves obtain reasonable agreement. The stress-strain curve under compression along tension exhibits typical slip dominated plastic deformation,

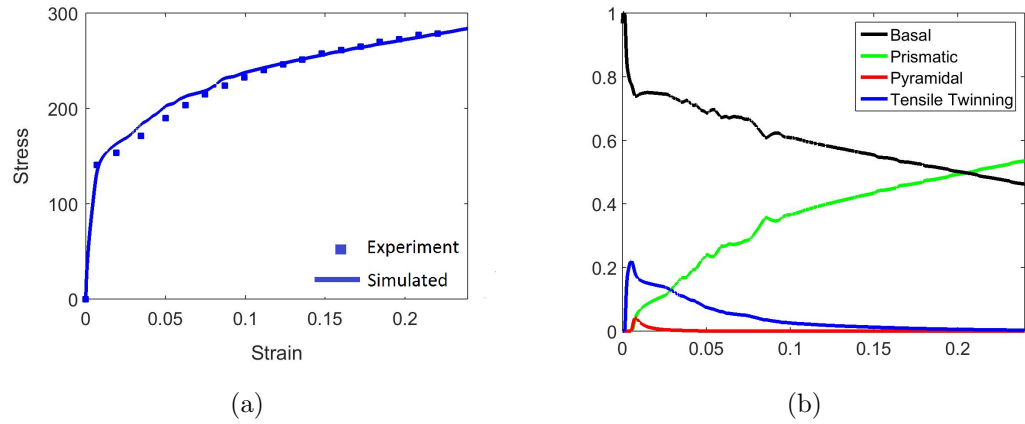


Figure 4.6: Predicted stress strain curves (a) and activities (b) under tension along TD (TD-T).

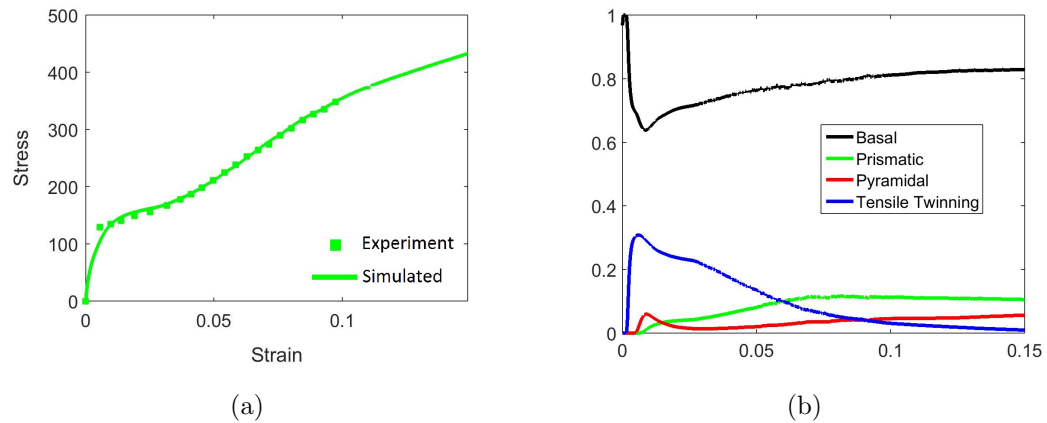


Figure 4.7: Predicted stress strain curves (a) and activities (b) under compression along TD (TD-C).

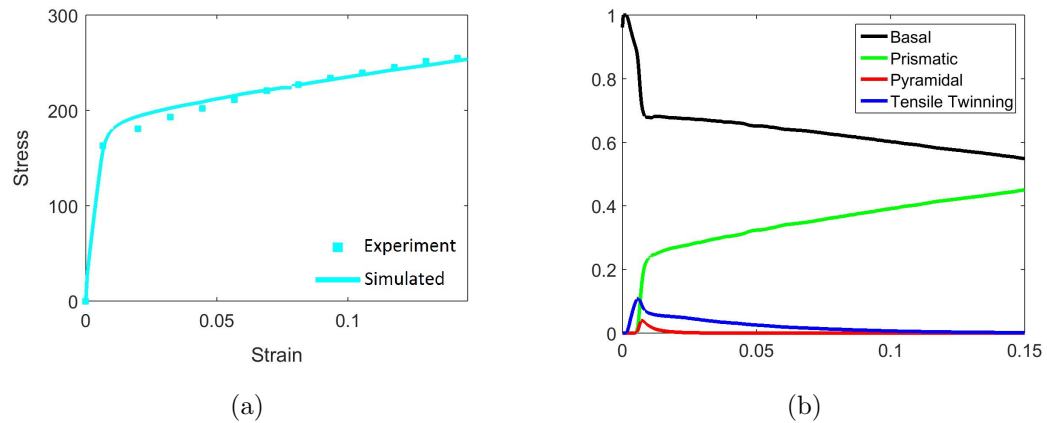


Figure 4.8: Predicted stress strain curves (a) and activities (b) under tension along 45° (45-T).

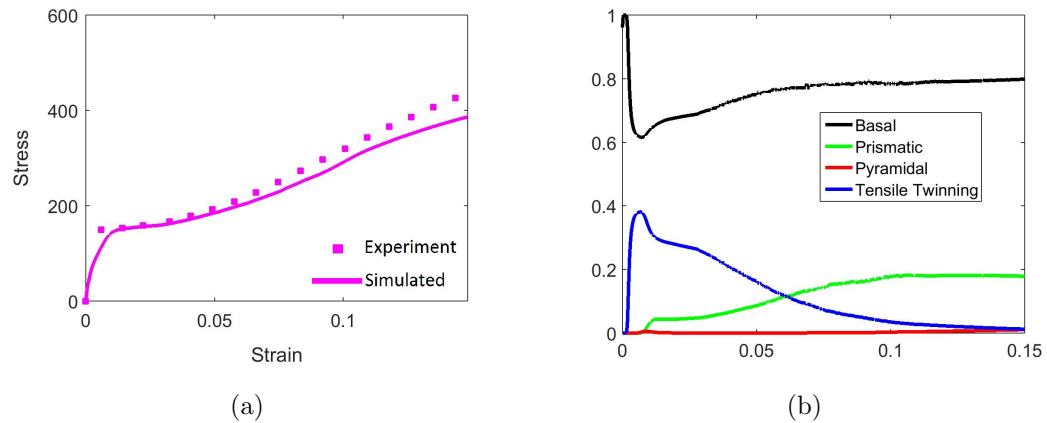


Figure 4.9: Predicted stress strain curves (a) and activities (b) under compression along 45° (45-C).

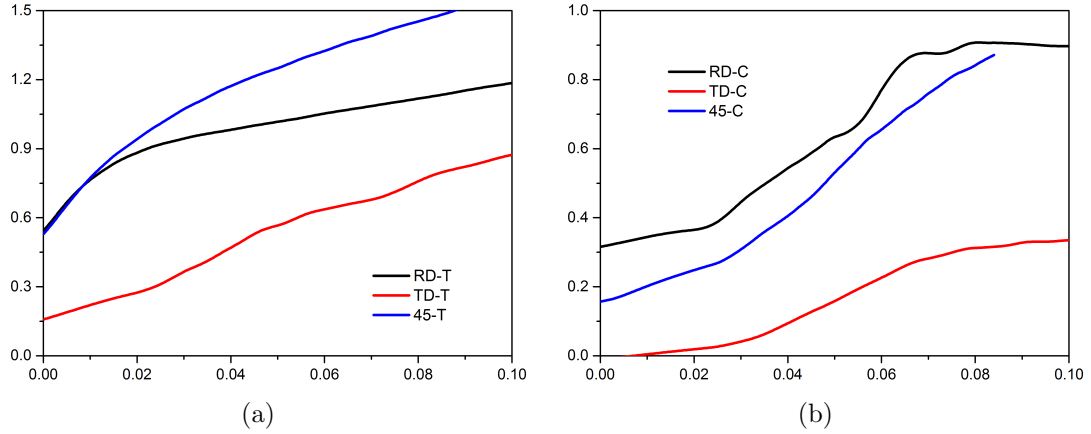


Figure 4.10: Instantaneous R values in different orientations in (a) tension and (b) compression.

although a little tensile twinning activity on small strains is predicted by the model. In contrast, the flow curve of compression along TD clearly reveals the characteristic S-shape. That means tensile twinning is an important deformation mechanism in TD-C

Figure 4.8 and 4.9 compare the predicted stress-strain curves under tension and compression along 45° direction. In general, the agreement between the predicted and measured stress-strain curve is reasonable. The predicted stress fits the experimental result well when strain is less than 0.1. After that, predicted stress slightly underestimates the experimental values.

R value, also called Lankford coefficient, is another important parameter in uniaxial test. It is defined as the ratio of the width strain to the thickness strain. The predicted instantaneous R values in different orientations along the tensile and compressive loading directions are plotted in Figure 4.10. The simulated R values for TD loading in both tension and compression are lower than RD and 45° orientations. This trend is attributed to greater resistance to in-plane deformation along RD vs

TT direction which is a direct result of the spread of the basal texture along the TD. This is consistent with the experimental result as well as initial texture in Figure 4.1. Generally, the predicted result successfully reproduce the trends in the measured R value.

Figure 4.11 shows the texture before and after tensile deformation along the RD. The predicted results are similar to the results measured by Kurukuri *et al.* (2014). The initial sample has no c-axis poles parallel to RD. This does not change with tensile deformation. Basal pole positions are smeared around the TD pole in the deformed samples and the prism plane pole is strengthened. From stress-strain curve and activities in Figure 4.3, very little twinning occurs in the samples, deformation mainly accommodated by basal and prismatic slip. The predicted pole figure results give reasonable prediction.

Initial texture and predicted post-deformation texture of tension along TD show in Figure 4.12. In general, predicted result qualitatively capture the main features of the pole figures. Pole figures show that major reorientation of the lattice takes place during deformation. Grains with c-axes parallel to TD rotated away by tensile twinning to lie along TT and RD which are under compression.

Figure 4.13 shows the pole figures of deformed under compression along RD, TD and TT. From the pole figures, it is clear that the c-axes of the grains rotate to lie parallel to the compression axis, irrespective of orientation. This is typical when magnesium deforms by tensile twinning. The stress-strain curves show a S-shape in all compression test. The amount of twinning in TD and TT compression samples is less because the spread of the basal pole intensity along the TT and TD.

Based on the above discussion, the genetic algorithm approach gives a good overall performance on fitting and predicting the deformation of ZEK100 sheet.

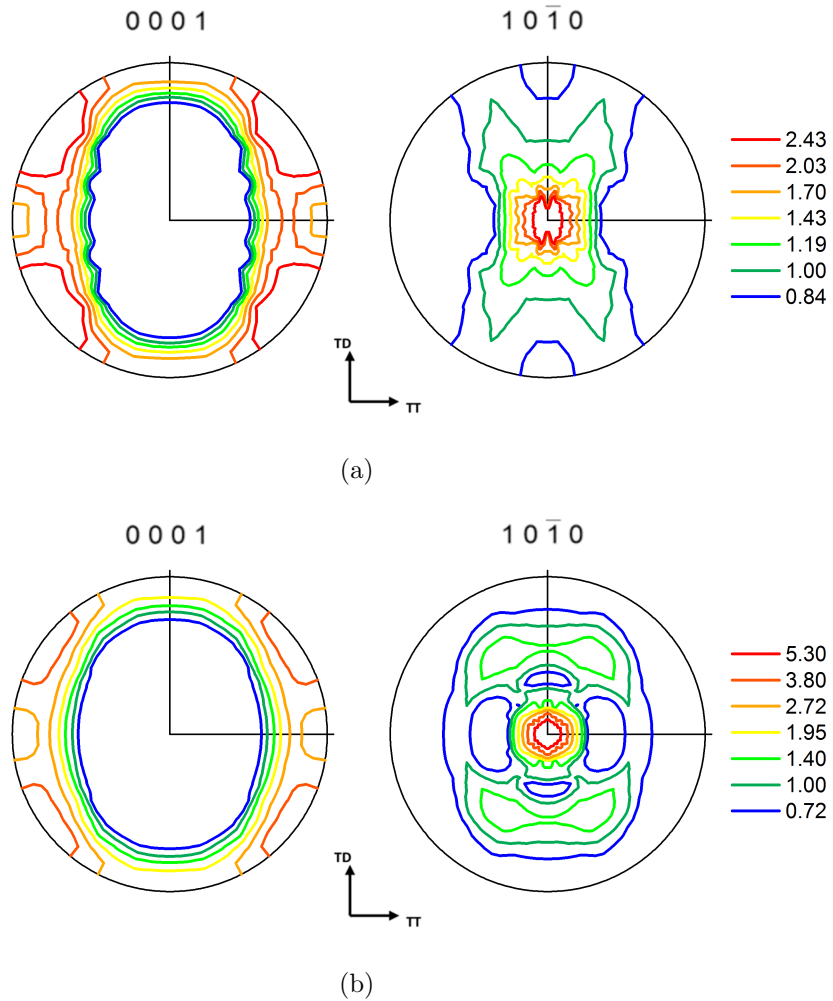


Figure 4.11: Predicted $\{0001\}$ and $\{10\bar{1}0\}$ pole figures of (a) initial texture (b) under tension along RD at strain = 0.15.

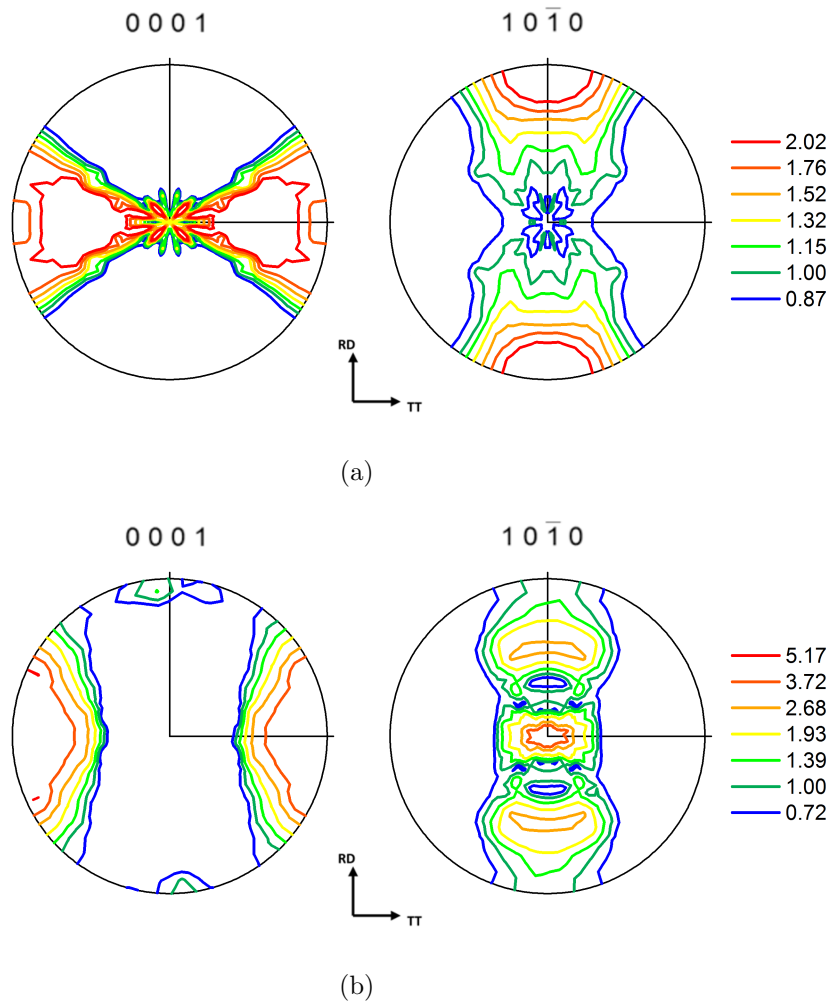


Figure 4.12: Predicted $\{0001\}$ and $\{10\bar{1}0\}$ pole figures of (a) initial texture (b) under tension along TD at strain = 0.2.

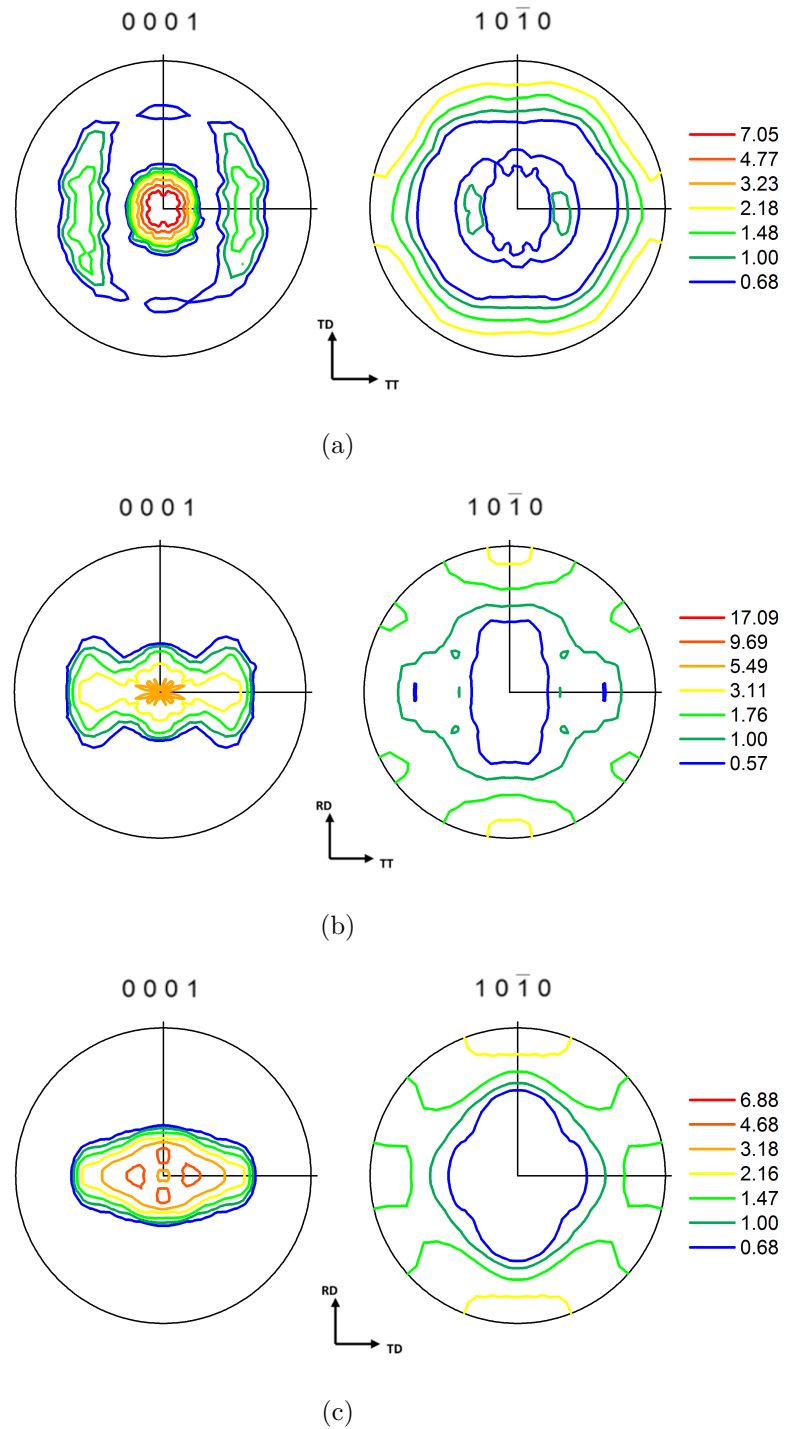


Figure 4.13: Predicted $\{0001\}$ and $\{10\bar{1}0\}$ pole figures of deformed compression samples at strain = 0.1 along (a) RD, (b) TD, (c) TT.

4.5 Conclusion

In this chapter, EVPSC-PTR model is used to simulate a series of mechanical test on magnesium ZEK100 sheet, and the accuracy of genetic algorithm approach on fitting material parameters has been proved.

The parameters are determined by fitting simulated stress and strain curve under uniaxial tension and compression along RD (RD-T, RD-C) and uniaxial compression along TT direction (TT-C) with the experimental result. The parameters are used to predict macroscopic behaviors of stress-strain curves along TD and 45°(TD-T, TD-C, 45-T, 45-C), R value, and the microscopic behaviors of post-deformation textures. By compare predicted results with experimental results, the accuracy and reliability of genetic algorithm approach is proved.

The genetic algorithm approach give a reliable fitting result for the magnesium ZEK100 plate. Although similar fitting result can be obtain by manually fitting parameters using traditional method, genetic algorithm approach can significantly reduce working time of human, and avoid spending time in the boring work. In general, genetic algorithm approach is a usable and reliable method for easily determining material parameters in polycrystal plasticity models. This method can be used in various research of EVPSC model.

Chapter 5

Study of magnesium alloy with random texture under tension and compression

5.1 Introduction

Due to the low symmetry of its crystallographic structure, constitutive modeling of the plastic deformation of Hexagonal Closed Packed (HCP) crystal is much more complicated than Face Centered Cubic (FCC) and Body Centered Cubic (BCC) crystal. In HCP crystal, there are different types of slip systems exist, although, very few slip systems can be activated at room temperature. For magnesium, the deformation behavior is different from other HCP metals such as Ti or Zr because the ratio of the crystallographic axes c/a close to ideal. At room temperature, the basal slip is the most easily activated system in Mg. The next systems to be activated are the first-order prismatic, followed by the first-order and second-order pyramidal which is general requires either higher applied stress and elevated temperatures to be activated.

Various polycrystal plasticity models have been developed for polycrystals. The Taylor model(Taylor, 1938) is one of the most popular one. Taylor model assumes that all grains must accommodate the same plastic strain, which equals to macroscopically imposed strain. This implies that the Taylor model neglects strain varies from grain to grain in the polycrystalline aggregate. As a consequence, the Taylor model does not consider the interaction between crystals, which is believed to be

less significant in FCC and BCC materials due to their high crystallographic symmetries. The Taylor model has played an important role in the field of modeling of forming of aluminum and steel sheets (Wu *et al.*, 1997; Dawson *et al.*, 2003; Eyckens *et al.*, 2009; Lévesque *et al.*, 2010). For metals like HCP polycrystals with low crystallographic symmetry, stress and strain vary from grain to grain and interaction among grains in a polycrystalline aggregate are significant and cannot be neglected in an attempt to accurately describe deformation behavior. Consequently, polycrystal plasticity models based on the self-consistent approach became more popular than the Taylor model when modeling HCP polycrystals. The self-consistent approach is originally proposed by Kröner (1958). Later, it was extended to the elasto-plastic (Hill, 1965) and viscoplastic (Hutchinson, 1976). In general, self-consistent models allow for different strain response in each grain, depending on the relative stiffness between the grain and a surrounding homogeneous equivalent medium (HEM). The consistency conditions require that the averaged behavior over all the grains must be the same as the macroscopically imposed one. Among various self-consistent plasticity models, the Visco-Plastic Self-Consistent (VPSC) model developed by Molinari *et al.* (1987), and extended by Lebensohn and Tomé (1993) to account for anisotropy, has been widely used to simulate large strain behavior and texture evolution of HCP polycrystalline Mg under various deformation modes (Agnew and Duygulu, 2005; Jain and Agnew, 2007; Neil and Agnew, 2009; Proust *et al.*, 2009; Signorelli *et al.*, 2009). Wang *et al.* (2010c) have developed a finite strain ElasticViscoplastic Self-Consistent (EVPSC) model for polycrystalline materials. The EVPSC model is a completely general elasticviscoplastic, fully anisotropic, self-consistent polycrystal model. It is applicable at large strain and to any crystal symmetry.

However, it has been noticed that the current polycrystal plasticity models involve a large number of material parameters, which may not be uniquely determined. For a textured HCP polycrystal, the only practical way to determine the material parameters associated with slip and twinning in a polycrystal plasticity model is by fitting numerical simulations based on the polycrystal model to the corresponding experimental data (Xu *et al.*, 2008). By introducing more constraints, the number of suitable parameter combinations can be significantly reduced, which can lead to a better predictive capability. An efficient way to tune polycrystal plasticity models is to obtain material parameters by not only fitting the macroscopic stress-strain curves and deformation textures, but also simultaneously fitting elastic lattice strains measured by in-situ neutron diffraction. However, using both the macroscopic and microscopic quantities to determine fitting parameters is very time consuming, and the traditional trial-and-error approach is not appropriate in this case. Therefore, a genetic algorithm approach is developed in this thesis to improve the agreement between a polycrystalline plasticity model and a large number of experimental data sets.

In this chapter, the reliability and accuracy of the genetic algorithm approach are evaluated by simulating the experimental result of random textured cast magnesium which was previously studied by Máthis *et al.* (2015). EVPSC-TDT model was used in this simulation. An assessment of the genetic algorithm approach is made based on comparisons of the predicted and experimental stress responses, twin volume fraction, texture evolution and lattice strain.

5.2 Constitutive model

5.2.1 Crystal plasticity

The EVPSC model(Wang *et al.*, 2010c) is applied to simulate the tension and compression tests in this chapter.

In the constitutive modeling of deformation of Mg alloys, the plastic deformation of a crystal is accommodated by crystallographic slip and twinning on crystallographic system $(\mathbf{s}^\alpha, \mathbf{n}^\alpha)$, with \mathbf{s}^α and \mathbf{n}^α being the slip/twinning direction and the normal of the slip/twinning plane for system α , respectively. The plastic strain rate tensor for the crystal can be written as:

$$\mathbf{d}^p = \sum_{\alpha} \dot{\gamma}^{\alpha} \mathbf{P}^{\alpha} \quad (5.1)$$

where $\dot{\gamma}^{\alpha}$ is the shear rate and $\mathbf{P} = (\mathbf{s}^{\alpha} \mathbf{n}^{\alpha} + \mathbf{n}^{\alpha} \mathbf{s}^{\alpha})/2$ is the Schmid tensor for system α . For both slip and twinning, the resolved shear stress $\tau^{\alpha} = \boldsymbol{\sigma} : \mathbf{P}$ is the driving force for the shear rate $\dot{\gamma}^{\alpha}$, with $\boldsymbol{\sigma}$ is the Cauchy stress tensor.

For slip, the shear strain rate is defined as:

$$\dot{\gamma}^{\alpha} = \dot{\gamma}^0 |\tau^{\alpha} / \tau_{cr}^{\alpha}|^{\frac{1}{m}} \text{sgn}(\tau^{\alpha}) \quad (5.2)$$

where $\dot{\gamma}^0$, τ_{cr}^{α} and m are a reference shear rate, the critical resolved shear stress (CRSS) and the strain rate sensitivity coefficient, respectively.

Due to its polar nature, the shear rate due to twinning is described by:

$$\dot{\gamma}^{\alpha} = \begin{cases} \dot{\gamma}^0 |\tau^{\alpha} / \tau_{cr}^{\alpha}|^{\frac{1}{m}} & \tau^{\alpha} > 0 \\ 0 & \tau^{\alpha} \leq 0 \end{cases} \quad (5.3)$$

For both slip and twinning, the evolution of the critical resolved shear stress (CRSS) τ_{cr}^α as deformation processed is given by:

$$\dot{\tau}_{cr}^\alpha = \frac{d\hat{\tau}^\alpha}{d\gamma_{ac}} \sum_{\beta} \mathbf{h}^{\alpha\beta} \dot{\gamma}^\beta \quad (5.4)$$

Where γ_{ac} is the accumulated shear strain in the grain, and $\mathbf{h}^{\alpha\beta}$ are the latent hardening coupling coefficients, which empirically account for the obstacles on system α associated with system β . $\hat{\tau}^\alpha$ is the threshold stress, described here by an extended Voce law (Tome *et al.*, 1984):

$$\hat{\tau}_0^\alpha = \tau_0^\alpha + (\tau_1^\alpha + h_1^\alpha \gamma_{ac}) (1 - \exp(-\frac{h_0^\alpha}{\tau_1^\alpha} \gamma_{ac})) \quad (5.5)$$

Here, τ_0, h_0, h_1 and $\tau_0 + \tau_1$ are the initial CRSS, the initial hardening rate, the asymptotic hardening rate, and the back-extrapolated CRSS, respectively.

In this chapter, the Affine self-consistent model of the EVPSC model is used. From Wang's results (Wang *et al.*, 2010b), it can be seen that the Affine self-consistent model performs the best features of Magnesium alloy. The Affine method (Masson *et al.*, 2000; Lebensohn *et al.*, 2004) assumes a higher compliance and will have a higher strain heterogeneity compared to the secant method.

$$\mathbf{M}^{\nu, \text{aff}} = \frac{\dot{\gamma}_0}{\mathbf{m}} \sum_{\alpha} \left(\frac{\tau^\alpha}{\tau_{cr}^\alpha} \right)^{\frac{1}{m}-1} \frac{\mathbf{P}^\alpha \mathbf{P}^\alpha}{\tau_{cr}^\alpha}, \dot{\epsilon}^{0, \text{aff}} = \left(1 - \frac{1}{m}\right) \dot{\epsilon}^p \quad (5.6)$$

For details concerning the self-consistent equations associated with the different visco-plastic self-consistent algorithms, one can refer to (Lebensohn *et al.*, 2007)

5.2.2 Twinning model

The plastic deformation in materials with HCP crystallographic structure is due to both slip and twinning. In magnesium and its alloys, the most commonly observed twinning mode is the $10\bar{1}2\langle 10\bar{1}1 \rangle$ extensive twinning when the c -axis of the hexagonal lattice experiences tension. The extension twinning results in an 85.22° reorientation of the basal pole. Because of this nearly 90° reorientation, de-twinning could occur in the twinned areas at subsequent reversed loading (see e.g. Roberts, 1960).

In the present TDT model, the deformation processes of twinning and de-twinning can take place by four operations, as illustrated in Figure 5.1:

- A. Twin initiation (which here comprises nucleation and propagation phases)
- B. twin growth
- C. twin shrinkage
- D. re-twinning (initiation of a twin with the parent orientation within the twin)

Note that operation D is actually a subset of a broader class of secondary twinning operations, which include twinning of all possible variants within the twins.

In Figure 5.1, (a) The grain is twin-free and is called the matrix in the text. (b) The grain undergoes twin initiation (Operation A) resulting in a twin band (called twin). Solid green lines represent twin boundaries (TBs). Lattices in the matrix (represented by blue lines) and twin (red lines) are crystallographic mirrors of one another. (c) Operation B is growth of the twin, thereby consuming the matrix. (d) Operation C is the reverse of operation B, involving propagation of the TBs back into the twin, causing growth of the matrix. (e) Operation D is another means of

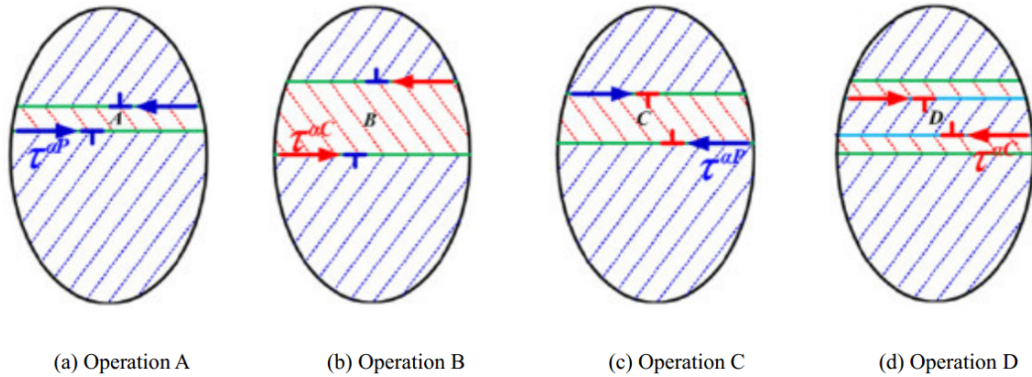


Figure 5.1: Schematic representation of twinning and de-twinning in a grain (Wang *et al.*, 2012a).

shrinking the twinned region through twin nucleation within the existing twin back into the orientation of the original matrix (hence the blue dotted lines).

Starting with a twin-free grain (referred to as matrix) in Figure 5.1(a), the grain starts twinning by twin nucleation (TN) associated with the twin system (Figure 5.1(b)) when the resolved shear stress (RSS) in the matrix, equals the critical resolved shear stress (CRSS) for operation A (τ_A). The grain is then split into a twinned domain (twin) and an un-twinned domain (matrix). The corresponding crystallographic lattices are mirrored across the twin boundary (TB) plane. When it is stated that a grain is ‘split’, note that an entirely new ‘grain’ is introduced into the self-consistent formulation to represent each twin variant that is activated, with a volume fraction corresponding to the amount of shear that has been accumulated during that straining step. Note further that the newly formed twin grains are free to undergo slip according to the same laws as the matrix grains. At this point, secondary twinning (twinning within the twins) is not accounted for, since this would lead to a proliferation of grains. The stress level in the newly formed grains is determined by the self-consistent algorithm and requires no assumptions. The accumulated shear strain

(or strain hardening state) within the twin domain reset to zero.

Due to the polar nature of twinning, the initial twinning event can only produce shear in the forward (twinning) direction. It is clear that the Cauchy stress acting on the matrix must be used to calculate the RSS of twin initiation because the twin is not born yet. The RSS acting on the twinning system is calculated in the same way as for slip Eq.4.2, and must be positive for twin nucleation to take place. In the present modeling scheme, no differentiation is made between twin nucleation and the rapid propagation (presumably at speeds approaching the speed of sound) across the matrix grain; this is denoted operation A. After this operation, twin growth (thickening) will occur when the RSS on the twinning system exceeds τ_B , the CRSS for twin growth, termed operation B. It is generally understood that the CRSS for twin growth is less than or equal to that required for initiation (Reed-Hill *et al.*, 1965; Partridge, 1967; Christian and Mahajan, 1995; Christian, 2002).

A key feature of the TDT model is an acknowledgement that the driving force for twin growth is provided by stresses acting on the twin boundary (TB) and the strategy employed is designed to approximate this reality. “Because the model is implemented within an effective medium approximation, it does not provide the local stresses at the TB, only the average stress in the ellipsoids that represent matrix and twin. (Wang *et al.*, 2012a) Thus, the Cauchy stress acting on the matrix grain and that acting on the new twin grain are both interrogated to assess the level of twin growth which may occur within a given straining increment. This is a key feature, which permits the model to describe the strain hardening plateau that is often observed when twinning is the primary strain accommodation mechanism. Other modeling strategies have not succeeded in predicting a strain hardening plateau without resorting to ad hoc

solutions, such as delaying the reorientation associated with twinning until after the plateau is complete (e.g. Agnew *et al.*, 2001) or adopting a very low CRSS value for prismatic slip when twinning is the dominant mechanism (Clausen *et al.*, 2008; Muránsky *et al.*, 2009). The former is known to be a poor representation, given all of the in-situ (and ex-situ) data which has been developed for twin volume fraction, f^{tw} , as a function of strain (e.g. Brown *et al.*, 2005; Muránsky *et al.*, 2009; Lou *et al.*, 2007). These data have unequivocally shown that f^{tw} is rapidly increasing throughout the plateau region. The suggestion of Clausen *et al.* (2008), that prismatic slip in Mg is strongly sensitive to the applied pressure (such that tensile and compressive responses would be so asymmetric), has failed to develop experimental support.

The lowering of the parameter describing prismatic slip strength during compression testing adopted by Clausen *et al.* (2008) has since been proven unnecessary by Wang *et al.* (2013a), though a number of recent papers have repeated this error as they reanalyzed the data published by Clausen *et al.* (2008) by employing the low value for prismatic slip strength for modeling ED compression (see Abdolvand and Daymond, 2012; Juan *et al.*, 2014). In addition, there are examples of FE-based crystal plasticity models in which no reorientation is accounted for at all (Graff *et al.*, 2007). In such case, the appearance of a plateau and subsequent rapid hardening are entirely phenomenological and should not be viewed as physically based.

Twin growth (operation B shown in Figure 5.1(c)) occurs when the sign of the resolved shear stress is positive. When the sense of the stress is negative, de-twinning (operation C) can occur. This simply means that the twin boundary retreats from the matrix into the twin. Hence, the twin volume fraction f^{tw} decreases. To some readers, this may initially seem like a violation of the twin polarity introduced above.

However, the aforementioned polarity of twinning only applies to the creation of a twin. Stresses in the anti-twinning direction will never result in twin nucleation, but once the twin is created, there is nothing to prevent the reverse motion of the TB, thereby accommodating twinning shear in the reverse sense. In the present model, no discrimination is made between the CRSS values of twin growth τ_B and twin shrinkage τ_C ; i.e., it is imagined that the twin boundaries can move with equal ease in the forward and reverse directions. This is contrary to the conclusion of Lou *et al.* (2007), that twinning is somewhat more difficult than de-twinning.

Finally, operation D Re-twinning (RT) represents the activation of a twin within a twin (Fig. 5.1(e)). It corresponds to the activation of TDs inside the twinned region, not necessarily at twin boundary (Fig. 5.1(e)). It splits the twin band and decreases the twin volume fraction and thus corresponding to de-twinning. The twin variant could be same as or different from the pre-existing twin variant. If the variant is the same as the pre-existing twin, it corresponds to de-twinning through the nucleation of a twin. If the variant is different from the pre-existing twin, it corresponds to secondary twinning through the nucleation of a new twin variant in the twin. Because re-twinning corresponds to the introduction of a new twin, the CRSS for re-twinning could be the same as the CRSS for twin nucleation. The resolved shear stress corresponding to this operation is calculated using the stress state inside the twin. It is clear that Operations B-D are impossible in a twin-free grain.

The driving force for both twinning and detwinning is assumed to be the resolved shear stress $\tau^\alpha = \boldsymbol{\sigma} : \boldsymbol{P}^\alpha$ associated with twinning system α . However, it is important in the self-consistent model to know where the resolved shear stress τ^α for twinning/de-twinning is originating from. It is clear that the twin nucleation by

Operation A has to be driven by the stress state of the parent ($\tau^{\alpha P}$ in Fig. 5.1(b)), since this is not yet a child. Computationally, the driving force $\tau^{\alpha P}$ is calculated from the true stress tensor $\boldsymbol{\sigma}$ of the parent and Schmid tensor $P^\alpha = \frac{1}{2}(s^\alpha n^\alpha + n^\alpha s^\alpha)$ associated with the lattice of the parent for system α . It is also clear that Operation D, taking place inside a twinned domain, has to be driven by the stress state of the twinned region or the child ($\tau^{\alpha C}$ in Fig. 5.1(c)). This implies that the driving force $\tau^{\alpha C}$ is calculated from the true stress tensor $\boldsymbol{\sigma}$ of the child and Schmid tensor $P^\alpha = \frac{1}{2}(s^\alpha n^\alpha + n^\alpha s^\alpha)$ associated with the lattice of the child for system α . As for Operations B and C, they are driven by the stress at the parent-child interface. Based on the discussion above for twin growth corresponding to Operation B it is more appropriate to use the resolved shear stress τ^α calculated from the child stress state ($\tau^{\alpha C}$). Note that the sense of this shear is such that it will activate TDs on the parent side but not on the child side, and so will lead to twin growth. By reversing the argument, although it is less clear-cut, in the case of de-twinning Operation C, where the sense of shear is reversed and the parent grows into the child. Now TDs propagating on the child side are activated by the resolved shear calculated from the parent stress state ($\tau^{\alpha P}$ in Fig. 5.1(d)).

In the proposed TDT model, a new twin band (child) is treated as a new grain, and all six tensile twin variants are possible present. The initial orientation of the new grain associated with twinning system is related to the orientation of the parent by the rotation matrix $\boldsymbol{Q} = 2\boldsymbol{n}^\alpha \otimes \boldsymbol{n}^\alpha - 1$. The weight of the new grain w^{g^α} is the product of the twin volume fraction f^α and the weight of the twin-free grain (parent) w^g , i.e. $w^{g^\alpha} = f^\alpha w^g$. Inside the parent, and associated with twinning system α , the shear rates due to Operations A and C are defined as:

$$\begin{aligned} \dot{\gamma}^{\alpha A} &= \begin{cases} \dot{\gamma}_0 |\tau^\alpha / \tau_{cr}^\alpha|^{\frac{1}{m}} & \tau^\alpha = \tau^{\alpha P} > 0 \\ 0 & \tau^\alpha = \tau^{\alpha P} \leq 0 \end{cases} \\ \dot{\gamma}^{\alpha C} &= \begin{cases} -\dot{\gamma}_0 |\tau^\alpha / \tau_{cr}^\alpha|^{\frac{1}{m}} & \tau^\alpha = \tau^{\alpha P} < 0 \\ 0 & \tau^\alpha = \tau^{\alpha P} \geq 0 \end{cases} \end{aligned} \quad (5.7)$$

It is clear that Operation A and Operation C cannot be activated simultaneously, and that Operation C is possible only when a child exists. It is also evident that Operation A and C are twinning and de-twinning, respectively. Therefore, the evolution of the twin volume fraction associated with Operation A and C are respectively represented by

$$\dot{f}^{\alpha A} = \frac{|\dot{\gamma}^{\alpha A}|}{\gamma^{tw}} \quad \dot{f}^{\alpha C} = \frac{-|\dot{\gamma}^{\alpha C}|}{\gamma^{tw}} \quad (5.8)$$

Where γ^{tw} is the characteristic twinning shear strain.

The shear rates for twinning system α inside a child are from Operation B and D:

$$\begin{aligned} \dot{\gamma}^{\alpha B} &= \begin{cases} -\dot{\gamma}_0 |\tau^\alpha / \tau_{cr}^\alpha|^{\frac{1}{m}} & \tau^\alpha = \tau^{\alpha B} < 0 \\ 0 & \tau^\alpha = \tau^{\alpha B} \geq 0 \end{cases} \\ \dot{\gamma}^{\alpha D} &= \begin{cases} \dot{\gamma}_0 |\tau^\alpha / \tau_{cr}^\alpha|^{\frac{1}{m}} & \tau^\alpha = \tau^{\alpha D} > 0 \\ 0 & \tau^\alpha = \tau^{\alpha D} \leq 0 \end{cases} \end{aligned} \quad (5.9)$$

Again, Operation B and D cannot be activated simultaneously and are impossible in a twin-free grain. It is clear that Operations B and D are twinning and de-twinning, respectively. The evolution of the twin volume fraction due to Operation B and D are respectively characterized by

$$\dot{f}^{\alpha B} = \frac{|\dot{\gamma}^{\alpha B}|}{\gamma^{tw}} \quad \dot{f}^{\alpha D} = \frac{-|\dot{\gamma}^{\alpha D}|}{\gamma^{tw}} \quad (5.10)$$

The evolution of twin volume fraction associated with twinning system α is governed by:

$$\dot{f}^{\alpha} = f^{\alpha}(\dot{f}^{\alpha A} + \dot{f}^{\alpha C}) + f^{\alpha}(\dot{f}^{\alpha B} + \dot{f}^{\alpha D}) \quad (5.11)$$

Where f^0 is the volume fraction of the parent, i.e. $f^0 = 1 - f^{tw} = 1 - \sum_{\alpha} f^{\alpha}$.

The stress state in the matrix and twin grains are computed independently, via the self-consistent algorithm, which employs linearized versions of the single crystal constitutive law such that the respective orientations of the twin and matrix are naturally taken into account.

The final element of this crystal plasticity model is a threshold approach which is employed to prevent grains from twinning in their entirety, since this is rarely observed experimentally. When the volume fraction of twins in a given grain exceeds a threshold value V^{th} , that grain ceases to be able to twin. Two empirical parameters A_1 and A_2 are employed to control this aspect of the response.

$$V^{th} = \min \left(1.0, A_1 + A_2 \frac{V^{eff}}{V^{acc}} \right) \quad (5.12)$$

The total accumulated twin volume fraction in the polycrystal is denoted as V^{acc} , and the volume fraction of grains which have ceased twinning is denoted V^{eff} . A_1 essentially controls the level of strain (volume fraction) which a grain can undergo prior to the twinning mechanism beginning to undergo exhaustion. A_2 , on the other hand, essentially controls the rate at which this exhaustion takes place once it has begun. Eventually, the capacity to twin is completely exhausted and additional straining

within the twins (and surrounding matrix grains) will rely on other means of straining. Since the alternatives involve deformation by prismatic slip (low critical stress, but poorly oriented) or non- prismatic slip (well oriented, but high critical stresses), the applied stress must be high in order for it to continue straining.

As mentioned before, for both slip and twinning, the evolution of the CRSS values τ_{cr}^α is potentially controlled by an empirically determined latent hardening matrix $h^{\alpha\beta}$.

$$\dot{\tau}_{cr}^\alpha = \frac{d\hat{\tau}^\alpha}{\Gamma} \sum_{\beta} h^{\alpha\beta} |\dot{\gamma}^\beta| \quad (5.13)$$

Where Γ is the total accumulated shear strain within the grain due to all slip and twinning systems; $\dot{\gamma}^\beta$ is the shear on a specific slip or twinning system, β ; and $\hat{\tau}^\alpha$ is an empirical Voce hardening law (with an initial CRSS value τ_0 , an initial hardening rate h_0 , and a saturation stress $(\tau_0 + \tau_1)$).

5.3 Genetic algorithm

In order to determine the material parameters associated with slip and twinning in this polycrystal plasticity model, a genetic algorithm fitting program is used to fit numerical simulations to the corresponding experimental data.

Genetic algorithm is a simple optimization technique which can be applied to data fitting problems. It begins by accepting upper and lower bounds on the parameters to be adjusted and generates several sets of parameters, distributed randomly throughout the available possibility space. Each set of parameters is known as an individual and the first set of randomly generated individuals forms the first generation. The algorithm then sends each individual to a separate instance of the problem being

optimized (i.e. in this case the EVPSC-TDT program). The various individuals then have the results of their application to the problem evaluated by a fitness function. The fitness function compare the simulation result with the experimental result and evaluates the difference:

$$\text{Fitness} = \sum (\text{distance}(\text{Exp.}, \text{Sim.})) \quad (5.14)$$

Once all the individuals have been evaluated and ranked relative to one another, a sample of the highest ranking individuals are taken and used as potential parent individuals to form the next generation.

The formation of each generation after the first one occurs via two operators, crossover and mutation. Crossover is the process of creating a new individual for generation $(n + 1)$ from two parental individuals in generation n . In the present case, crossover was performed by randomly selecting two parent individuals amongst the highest ranking individuals of generation n . For example, if two individuals in a given generation n with parameter sets of $(a_1; a_2; \dots; a_i)$ and $(b_1; b_2; \dots; b_i)$ are used as parents in a crossover process, the newly formed individual has the following parameters:

$$[\alpha_1 a_1 + (1 - \alpha_1) b_1; \alpha_2 a_2 + (1 - \alpha_2) b_2; \dots; \alpha_i a_i + (1 - \alpha_i) b_i] \quad (5.15)$$

where $\alpha_1, \alpha_2, \dots, \alpha_i$ are random real numbers between 0 and 1.

Mutation is analogous to biological mutation; it is a random process in which an individual is given one or more traits that were not present in either parent. Mutation is important in that it maintains a level of diversity amongst individuals of the same generation, which is useful in helping the GA to avoid becoming trapped in a region

of the parameter space that is only locally optimal. If a mutation is added to the previous example involving crossover, a potential result is

$$[\alpha_1 a_1 + (1 - \alpha_1) b_1; x_2; \dots; \alpha_i a_i + (1 - \alpha_i) b_i] \quad (5.16)$$

Note that x_2 is an entirely new trait not previously seen in the parent individuals.

The range of parameters is the the lower and upper bounds of the parameter set, $(l_1; l_2; \dots; l_i)$ and $(u_1; u_2; \dots; u_i)$, which is one of key factor in genetic algorithm approach.

In this case, four deformation mechanisms are taken into account during modeling and are subsequently refined by the GA: basal slip, prismatic slip, pyramidal slip and tensile twinning. As stated in the previous section, the parameters being adjusted for each slip and twinning system are initial CRSS τ_0 , the back-extrapolated CRSS τ_1 , the initial hardening rate θ_0 and the asymptotic hardening rate θ_1 . According to previous attempt at fitting EVPSC output to this data set, latent hardening $h_{\alpha\beta}$ simplified as h_{st} , indicates only the effect of extension twinning system t for slip system s take into account. This reduces latent hardening coefficient from 16 to 4. Furthermore, the τ_1 , θ_0 and θ_1 for tensile twinning has little effect to the simulation result in this experiment. These three parameters are not consider in this chapter. All in all, the total number of free parameters is 17.

With only two groups of experimental data, finding a suitable parameter combination should not be difficult. However, there is no preferential orientation in random texture material, and the activity of each slip system are similar in tension and compression. That causes difficulty in determining material parameters manually. Using genetic algorithm approach make the process easier. In this study, upper and lower

bounds of genetic algorithm are firstly determined by the previous research. The boundaries used in genetic algorithm approach are shown in Table. 5.1.

Mode	$\tau_0(\text{MPa})$	$\tau_1(\text{MPa})$	$\theta_0(\text{MPa})$	$\theta_1(\text{MPa})$
Basal	$1 \leq \tau_0^{bas} \leq 20$	$1 \leq \tau_1^{bas} \leq 20$	$100 \leq \theta_0^{bas} \leq 150$	$30 \leq \theta_1^{bas} \leq 60$
Prismatic	$10 \leq \tau_0^{bas} \leq 40$	$20 \leq \tau_1^{bas} \leq 60$	$300 \leq \theta_0^{bas} \leq 600$	$90 \leq \theta_1^{bas} \leq 140$
Pyramidal	$50 \leq \tau_0^{bas} \leq 80$	$40 \leq \tau_1^{bas} \leq 80$	$150 \leq \theta_0^{bas} \leq 250$	$60 \leq \theta_1^{bas} \leq 100$
Tensile Twin	$2 \leq \tau_0^{bas} \leq 20$	0	0	0

Table 5.1: Upper and lower bounds of parameters used during genetic algorithm refinement.

Besides, the bounds for latent hardening were: $1.0 \leq h_{st} \leq 2.0$. These ranges were chosen to agree with published polycrystal data and are also satisfy with previous fitting results.

Since the boundaries involve in genetic algorithm are refer to other experimental parameters for AZ31 alloy in EVPSC-TDT model as well as same material with EPSC model(Máthis *et al.*, 2015), the final result should be appropriate.

After some trial to find a good balance between total run time and the final quality of the results, a fitting procedure was developed. 100 individuals were used in each generation, and the algorithm was allowed to run for a total of 30 generations, resulting in a total of more than 2500 different parameter sets being run through the EVPSC-TDT model. It took roughly 3 to 4 days to run all 30 generations.

5.4 Results and discussion

The material considered in this chapter is cast magnesium, which has been experimentally studied by Máthis *et al.* (2015). The texture used in this research is randomly textured cast polycrystalline magnesium, it does not show any preferential

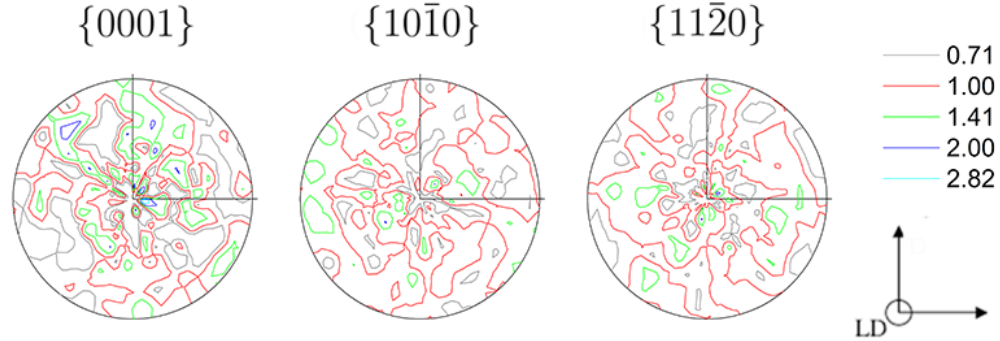


Figure 5.2: Initial texture of the random texture cast magnesium represented in terms of the $\{0001\}$, $\{10\bar{1}0\}$ and $\{11\bar{2}0\}$ pole distributions.

orientation. The initial crystallographic texture used in simulation is 1000 grains random texture. The $\{0002\}$, $\{10\bar{1}0\}$ and $\{11\bar{2}0\}$ pole figures of the texture are shown in Figure 5.2. The plastic deformation mechanisms of magnesium included in the EVPSC-TDT modeling are basal ($\{0001\}\langle 11\bar{2}0\rangle$), prismatic ($\{10\bar{1}0\}\langle 11\bar{2}0\rangle$), pyramidal $\langle \mathbf{a}+\mathbf{c} \rangle$ ($\{11\bar{2}2\}\langle 11\bar{2}3\rangle$) slip as well as tensile twinning ($\{10\bar{1}2\}\langle 10\bar{1}1\rangle$). Since the maximum measured strain level was only 6%, the $\{10\bar{1}1\}$ compressive twinning which usually observed at higher strains (Agnew *et al.*, 2013) was not included in the analysis.

In this chapter, the reference slip/twinning rate, $\dot{\gamma}_0$, and the rate sensitivity, m , are prescribed to be the same for all the slip/twinning systems: $\dot{\gamma}_0 = 0.001\text{s}^{-1}$ and $m = 0.05$, respectively. The macroscopic strain rate of $1 \times 10^{-3}\text{s}^{-1}$ is employed for the uniaxial tensile and compression test. The loading direction(LD) of this sample referred to as axial direction(Axial). For measured component of the lattice strain, the direction perpendicular to LD is called radial direction(Radial)

Values of the hardening parameters are determined by fitting numerical simulations of uniaxial tension and compression test using genetic algorithm approach.

Table 5.2 lists values of the material parameters for the EVPSC-TDT model. These parameters are used in all the simulations reported in this chapter.

Mode	τ_0 (MPa)	τ_1 (MPa)	θ_0 (MPa)	θ_1 (MPa)	h^{st}	A_1	A_2
Basal	3	15	135	57	1.5		
Prismatic	30	32	380	130	1		
Pyramidal	50	65	200	98	1.5		
Tensile Twin	2	0	0	0	1.3	0.1	0.75

Table 5.2: List of values of the hardening parameters involved in the EVPSC-TDT model.

Figure 5.3 present the fitted stress strain curves and activities of uniaxial tension and compression of EVPSC-TDT, respectively. The experimental and simulated stress-strain responses shows good agreement. That shows genetic algorithm approach work well on the fitting of stress-strain curve.

The parameters are used to predict twin volume fraction and microscopic behavior of the texture evolution. Figure 5.4 shows the twin volume fraction as a function of the absolute value of the applied strain for the tension and compression samples. The simulated twin volume fraction compared with the measured one (taken from (Čapek *et al.*, 2014)) is presented in. The simulation result slightly underestimates the experimental values, but the course of the simulation curves follow the measured data points well. In the entire range the twin volume fraction is larger for compression than for tension.

The pole figures (PF) at 0 , 2, 4 and 6% deformation for radial detector are shown in Figure 5.5 and Figure 5.6. The evolution of the texture is usually used to study the material behaviors at microscopic scale. The measured and predicted pole figures provide a view of the distribution of texture components in the Euler space. In this section, the texture is represented by the $\{0002\}$, $\{1010\}$ and $\{11\bar{2}0\}$ pole figures,

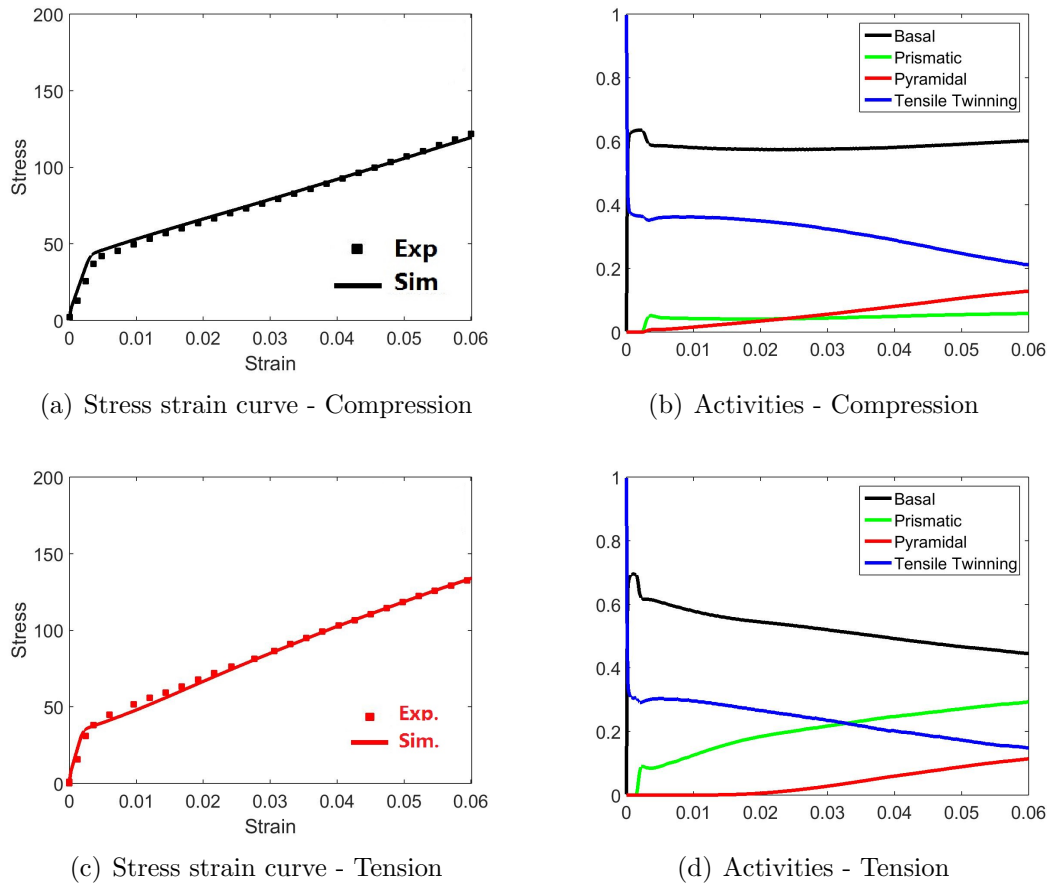


Figure 5.3: Experiment (symbols) and simulated (solid lines) true stress and true strain curves under (a) uniaxial compression, (c) uniaxial tension, Predicted slip/twinning activities under (b) uniaxial compression (d) uniaxial tension.

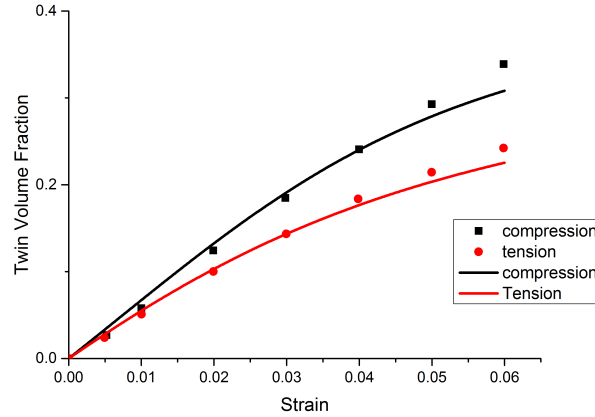


Figure 5.4: Experimental(symbols) and simulated(lines lines) twinned volume fraction in tension(red) and compression(black). The experimental data are taken from Čapek *et al.* (2014).

which are of the greatest interest and are the most frequently reported by literature.

Since the material used in this chapter is cast magnesium, it has a random texture distribution. As it shows in Figure 5.2, the initial texture orientation is homogeneous and does not show any preferential orientation.

In compression, Figure 5.5, $\{0001\}$ pole figure shows the transformation from a uniform orientation to a concentration of orientation at the centre of the pole figure.

In tension, a similar behavior is apparent. But it behaves exactly in opposite way due to the polar nature of the twinning. In $\{0001\}$ pole figure uniform orientation transforms to an annular distribution of orientations. The centre of the pole figure becomes the minimum part.

The main contribution of rapid texture evolution is from the re-orientation due to tensile twinning. It can be proved by activities curve on Figure 5.3, which tensile twinning is the one of major deformation mode. The results prove tensile twinning plays a major role in the deformation process.

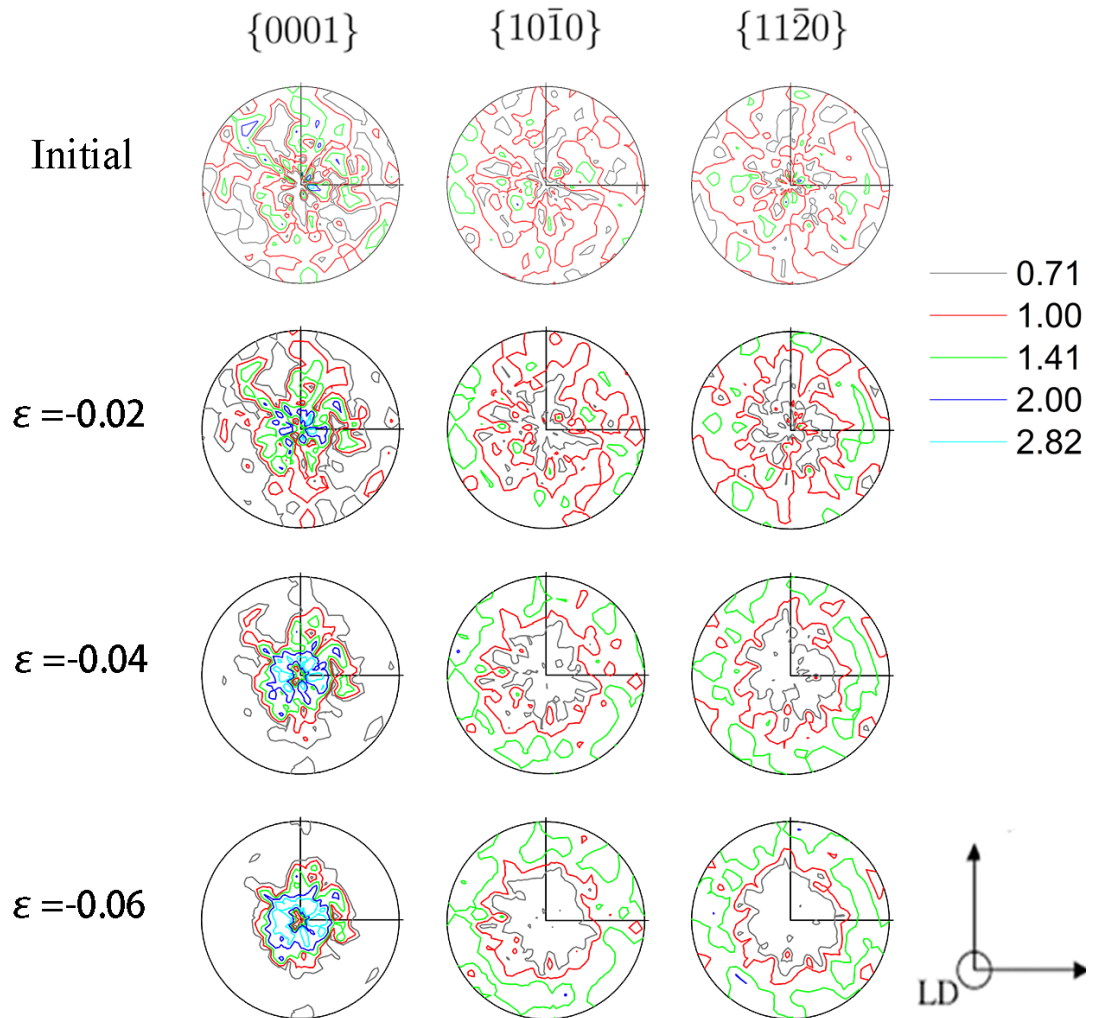


Figure 5.5: Simulated texture evolution in uniaxial compression.

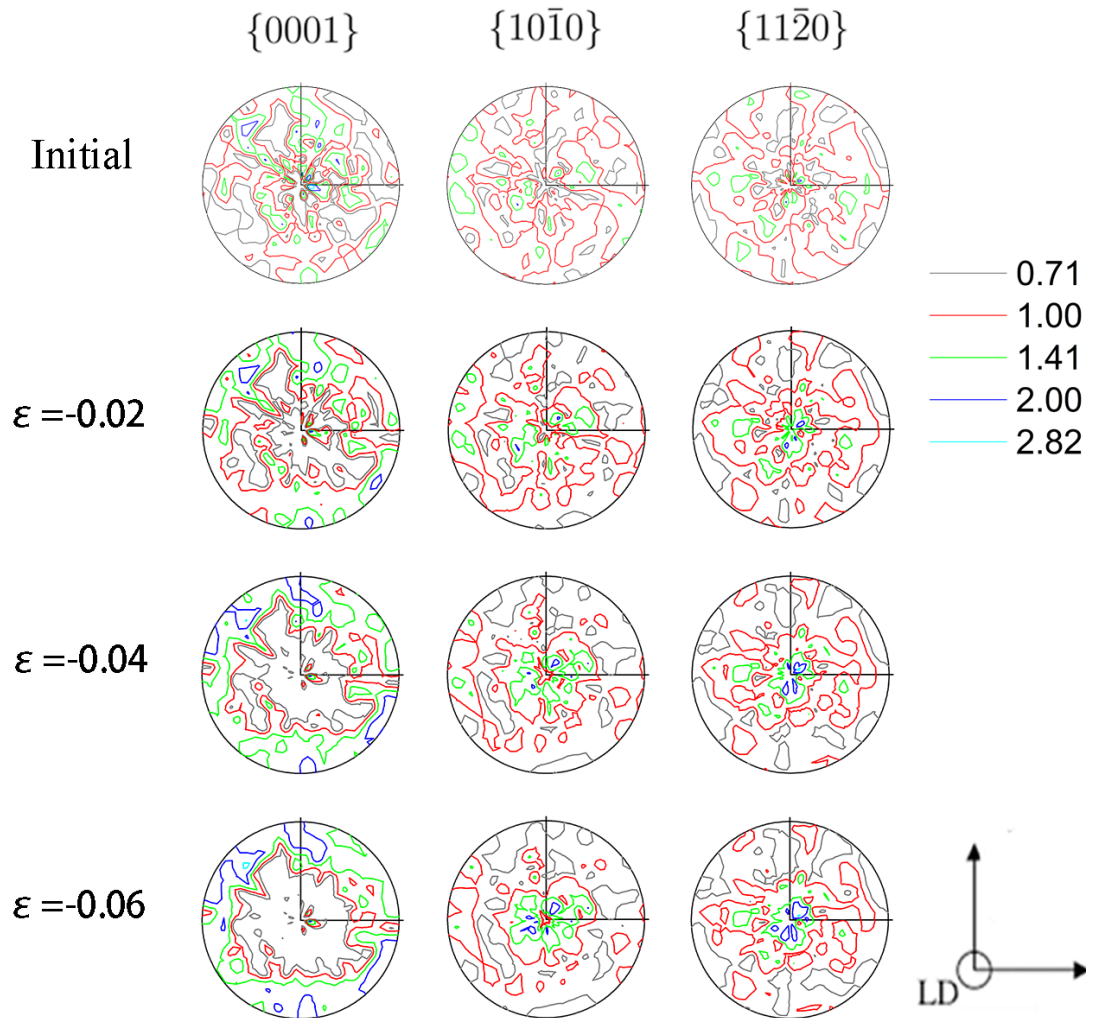


Figure 5.6: Simulated texture evolution in uniaxial tension.

The comparison of the simulation and measured lattice strains is depicted in Figure 5.7 and Figure 5.8. The non-linear behavior of the experimental internal strain data is qualitatively quite well predicted. Generally speaking, the model successfully reproduce the trends in the lattice strain data.

Figure 5.7(a) and Figure 5.7(b) show lattice strains along axial direction and radial direction under compression. For lattice strain along axial direction, the model give a bad prediction for the $\{0002\}$ grain family. But it give reasonable agreement between the predictions and experiments for the other families. For lattice strain along radial direction, the predicted lattice strain curves for the $\{0002\}$ family show clear relaxation effects at a stress of 75 MPa. This relaxation is caused by the sudden twinning-related reorientation of grains having the c-axis along the radial direction. This poor agreement between the simulations and experiments is mainly caused by the employed TDT twinning scheme.

Lattice strains along axial and radial direction under tension (Figure 5.8) are similar to compression. Along axial and radial direction, all grain families agree reasonably well with the experimental data, except $\{0002\}$ family along axial direction.

Based on the discussion above, it can be concluded that the GA approach has a good performance in determining the material parameters associated with slip and twinning in EVPSC-TDT model. Although some of the predictions of the TDT model for texture coefficients are not perfect, they are still reasonable. It has better performance than traditional manual fitting method. Although the GA has some limitation, using machine work instead of traditional trial-and-error approach reduce the workload for researcher.

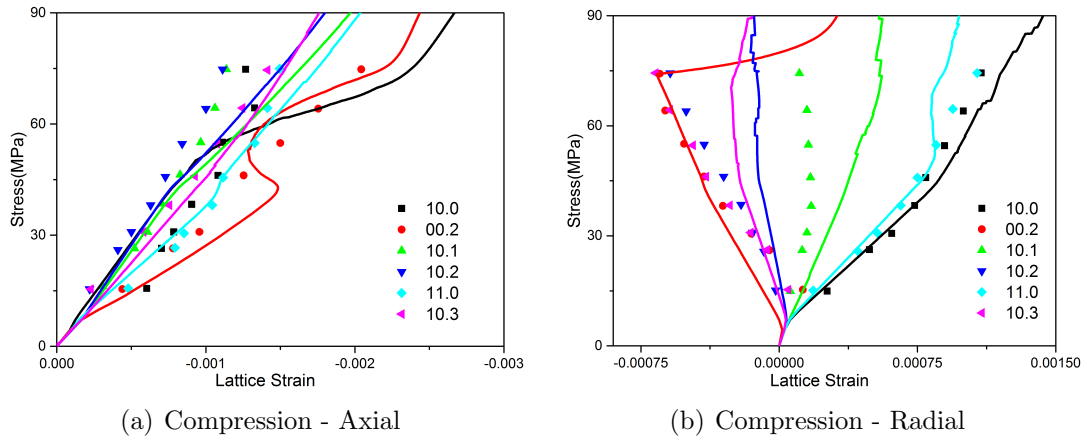


Figure 5.7: Experimental (symbols) and simulated (lines) lattice strain evolution versus the applied stress in uniaxial compression for both direction.

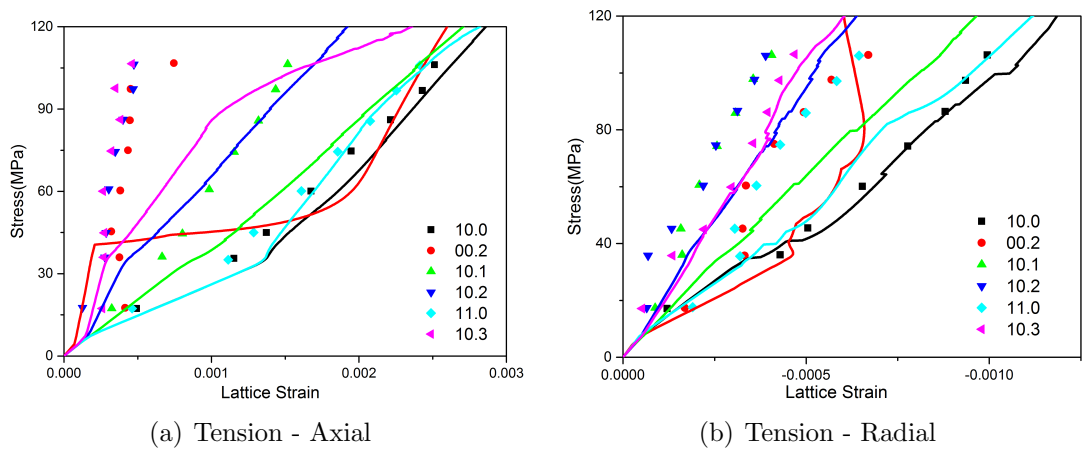


Figure 5.8: Experimental (symbols) and simulated (lines) lattice strain evolution versus the applied stress in uniaxial tension for both direction.

5.5 Conclusion

In this chapter, by fitting the material parameters of a random texture cast AZ31 magnesium alloy for EVPSC-TDT model, the performance of the genetic algorithm is tested.

The study is based on the predictability of the macroscopic behaviors of stress-strain curves and twin volume fraction and the microscopic behaviors of textures evolution and lattice strain. The deformation mechanisms of basal, prismatic, second order pyramidal $\langle c+a \rangle$ slips and tensile twinning are chosen to accommodate the plastic deformation. The genetic algorithm obtain the material parameters by fitting two sets of experimental stress strain curves (compression and tension).

The algorithm ran for a total of 30 generations, and 100 individuals are used in each generation. More than 2500 different parameter sets has been run through the EVPSC-TDT model to finally get a best set of parameters.

Overall, the genetic algorithm approach has a good performance. The fitting of stress-strain curve is quite well. For microscopic behavior of the texture evolution, the predicted results are in line with expectations. Although lattice strains are not perfectly fit the experimental result. One of the reason is the limited accuracy of TDT model for the prediction of strain lattice. Another important reason is the initial grain orientations of random texture are random. The simulation results should be more accurate if number of grains increases significantly. But more grains means it will cost more time on simulation, that will increase the difficulty and time cost of genetic algorithm approach.

As it known, the generation algorithm approach has prove its fitting result is

accurate and reliable. Further more, GA approach can get an effective result within a relatively short period of time. For a task have some difficulties by manually fitting, genetic algorithm approach got better result than human being. Besides, using genetic algorithm approach free researchers from spending time on the work of determining parameters, that save valuable time.

Chapter 6

Study of rolled magnesium AZ31 alloy under uniaxial compression and plane strain compression

6.1 Introduction

Magnesium is known as one of the lowest density structural metals. It is a highly competitive material for transportation industry due to the increasing importance of fuel economy and the need to reduce weight. Crystal plasticity-based approaches for modeling the constitutive behavior of textured Mg alloys have proliferated over the past decade or so. (Abdolvand and Daymond, 2012; Agnew *et al.*, 2001, 2006; Brown *et al.*, 2005; Clausen *et al.*, 2008; Graff *et al.*, 2007; Guo *et al.*, 2013; Lee *et al.*, 2014; Lévesque *et al.*, 2010; Muránsky *et al.*, 2009; Proust *et al.*, 2009; Wang *et al.*, 2010a, 2011, 2012b, 2013b,c)

At room temperature magnesium and its alloys are difficult to deform due to the crystal structure which is hexagonal close packed (HCP). It has been found that plastic deformation of HCP crystal is accommodated by slip and twinning. The most active slip mode for magnesium and its alloys is basal $\langle a \rangle$ slip. The next two systems to be activated are the first-order prismatic, followed by the first-order and second-order pyramidal. Prismatic and pyramidal slips generally require either higher applied stress and elevated temperatures to be activated. The most commonly observed twinning mode is the $\{10\bar{1}2\}$ tensile twinning when the c-axis of the hexagonal lattice experiences tension. The tensile twinning results in an 85.22° reorientation of the basal pole. $\{10\bar{1}1\}$ compressive twins are observed when compressed along c-axis, which

resulting in contraction along the c-axis and tilting of the lattice by 56° .

Among various self-consistent plasticity models, the Visco-Plastic Self-Consistent (VPSC) model (Molinari *et al.*, 1987; Lebensohn and Tomé, 1993) has been widely used to simulate large strain behavior and texture evolution of HCP polycrystalline Mg under various deformation modes (Agnew and Duygulu, 2005; Jain and Agnew, 2007; Neil and Agnew, 2009; Proust *et al.*, 2009; Signorelli *et al.*, 2009). The large strain EVPSC model developed by Wang *et al.* (2010c) is a completely general elastic-viscoplastic, fully anisotropic, self-consistent polycrystal plasticity model. The EVPSC model has been found to be able to predict many aspects of the large strain behavior of HCP materials (Clausen *et al.*, 2008; Guo *et al.*, 2013; Hutchinson *et al.*, 2012; Muránsky *et al.*, 2008, 2009; Neil and Agnew, 2009; Oppedal *et al.*, 2012; Xu *et al.*, 2008; Turner *et al.*, 1995; Wang *et al.*, 2010a,d, 2011, 2012a,b, 2013b; Wu *et al.*, 2012)

However, for current polycrystal plasticity models with both slip and twinning, including the VPSC and EVPSC, there are a large number of material parameters involved. For a textured HCP polycrystal, the only practical way to determine the material parameters is by fitting numerical simulations to the corresponding experimental data (Xu *et al.*, 2008). The parameters may not be uniquely determined. By introducing more constrains, the number of suitable parameter combinations can be significantly reduced, which can lead to a better predictive capability. However, using the traditional trial-and-error approach to determine parameters are very time consuming. Moreover, the more constrains were used, the more difficult to determine the parameter by traditional method. Therefore, a genetic algorithm approach is developed to optimize material parameters, in an effort to improve the agreement between

predictions from polycrystalline plasticity models and experimental data.

In this chapter, a hot-rolled magnesium AZ31 plate deformed under channel-die and uniaxial compression along different direction is simulated using EVPSC-TDT model. The material was previously studied experimentally by Chapuis *et al.* (2014). A genetic algorithm approach which presented in Chapter 3 are used to determined the material parameters. The author evaluated the performance of the simulated result at the true stress and true strain curves, twin volume fraction and texture evolution.

The chapter is organized as follows: Section 6.2 introduces the EVPSC model and TDT twinning models. Section 6.3 shows both the experimental and predicted results at the stress-strain curves, twin volume fraction and texture evolution. Finally, a summary are drawn in Section 6.4.

6.2 Constitutive model

6.2.1 Crystal plasticity

The elastic visco-plastic self-consistent (EVPSC) model for polycrystals recently developed by Wang *et al.* (2010c) was used to simulate the lattice strain evolution. It is a completely general elasti-visco-plastic, fully anisotropic, self-consistent polycrystal model, applicable to large strains and to any crystal symmetry. The model is based on the approximation proposed by Molinari *et al.* (1997) for treating the elasto-visco-plastic inclusion problem. Here is briefly describe of the model.

The plastic deformation of a crystal is assumed to be due to crystallographic slip and twinning on crystallographic system $(\mathbf{s}^\alpha, \mathbf{n}^\alpha)$, with \mathbf{s}^α and \mathbf{n}^α being the

slip/twinning direction and the normal of the slip/twinning plane for system α , respectively. For magnesium alloy, Basal $\langle \mathbf{a} \rangle$ ($\{0001\} \langle 11\bar{2}0 \rangle$), Prismatic $\langle \mathbf{a} \rangle$ ($\{10\bar{1}0\} \langle 11\bar{2}0 \rangle$) and Pyramidal $\langle \mathbf{c} + \mathbf{a} \rangle$ ($\{\bar{1}\bar{1}22\} \langle \bar{1}\bar{1}23 \rangle$) slip systems, and the tensile twin ($\{10\bar{1}2\} \langle 10\bar{1}\bar{1} \rangle$) and compression twin ($\{10\bar{1}1\} \langle 10\bar{1}\bar{2} \rangle$) system are usually considered.

The plastic strain rate tensor for the crystal can be written as:

$$\boldsymbol{\varepsilon}^p = \sum_{\alpha} \dot{\gamma}^{\alpha} \mathbf{P}^{\alpha} \quad (6.1)$$

Where $\dot{\gamma}^{\alpha}$ is the shear rate and $\mathbf{P}^{\alpha} = (\mathbf{s}^{\alpha} \mathbf{n}^{\alpha} + \mathbf{n}^{\alpha} \mathbf{s}^{\alpha})/2$ is the Schmid tensor for system α

The resolved shear stress $\tau^{\alpha} = \boldsymbol{\sigma} : \mathbf{P}^{\alpha}$, is the driving force for shear rate $\dot{\gamma}^{\alpha}$, with $\boldsymbol{\sigma}$ is the Cauchy stress tensor.

For slip:

$$\dot{\gamma}^{\alpha} = \dot{\gamma}_0 |\tau^{\alpha} / \tau_{cr}^{\alpha}|^{\frac{1}{m}} \text{sign}(\tau^{\alpha}) \quad (6.2)$$

Where $\dot{\gamma}_0$, τ_{cr}^{α} and m are a reference shear rate, the Critical Resolved Shear Stress (CRSS), and the strain rate sensitivity coefficient, respectively.

Due to its polar nature, the shear rate due to twinning is described by:

$$\dot{\gamma}^{\alpha} = \begin{cases} \dot{\gamma}_0 |\tau^{\alpha} / \tau_{cr}^{\alpha}|^{\frac{1}{m}} & \tau^{\alpha} > 0 \\ 0 & \tau^{\alpha} \leq 0 \end{cases} \quad (6.3)$$

The evolution of the critical resolved shear stress (CRSS) τ_{cr}^{α} as deformation proceeds is given by:

$$\dot{\tau}_{cr}^{\alpha} = \frac{d\hat{\tau}^{\alpha}}{d\Gamma} \sum_{\beta} \mathbf{h}^{\alpha\beta} |\dot{\gamma}^{\beta}| \quad (6.4)$$

Where $\Gamma = \sum_{\alpha} \int |\dot{\gamma}^{\alpha}| dt$ is the accumulated shear strain in the grain, and $h^{\alpha\beta}$ are the latent hardening coupling coefficients, which empirically account for the obstacles on system α associated with system β . $\hat{\tau}^{\alpha}$ is the threshold stress and is characterized by:

$$\hat{\tau}_0^{\alpha} = \tau_0^{\alpha} + (\tau_1^{\alpha} + h_1^{\alpha}\Gamma)(1 - \exp(-\frac{h_0^{\alpha}}{\tau_1^{\alpha}}\Gamma)) \quad (6.5)$$

Here, τ_0 , h_0 , h_1 and $\tau_0 + \tau_1$ are the initial CRSS, the initial hardening rate, the asymptotic hardening rate, and the back-extrapolated CRSS, respectively.

The elastic constitutive equation for crystal is:

$$\overset{\nabla}{\boldsymbol{\sigma}}^* = \mathcal{L} : \dot{\boldsymbol{\epsilon}}^e - \boldsymbol{\sigma} tr \dot{\boldsymbol{\epsilon}}^e \quad (6.6)$$

where \mathcal{L} is the fourth order elastic stiffness tensor, $\dot{\boldsymbol{\epsilon}}^e$ is the elastic strain rate tensor and $\overset{\nabla}{\boldsymbol{\sigma}}^*$ is the Jaumann rate of the Cauchy stress $\boldsymbol{\sigma}$ based on the lattice spin tensor \boldsymbol{w}^e . The single crystal elastic anisotropy is included in \mathcal{L} through the crystal elastic constants C_{ij} (Wang and Mora, 2008).

The response of a polycrystal comprised of many grains is obtained using a self-consistent approach: each grain is treated as an ellipsoidal inclusion embedded in a Homogeneous Effective Medium (HEM), which represents the aggregate of all the grains. Interactions between each grain and the HEM are described using the Eshelby inclusion formalism (Eshelby, 1957). The behaviour of the inclusion (single crystal) and HEM (polycrystal) can be linearized as follows:

$$\dot{\boldsymbol{\varepsilon}} = \mathbf{M}^e : \dot{\boldsymbol{\sigma}} + \mathbf{M}^\nu : \boldsymbol{\sigma} + \dot{\boldsymbol{\varepsilon}}^0 \quad (6.7)$$

$$\dot{\mathbf{E}} = \overline{\mathbf{M}}^e : \dot{\boldsymbol{\Sigma}} + \overline{\mathbf{M}}^\nu : \boldsymbol{\sigma} + \dot{\mathbf{E}}^0 \quad (6.8)$$

Here, \mathbf{M}^e , \mathbf{M}^ν , $\dot{\boldsymbol{\varepsilon}}$, $\boldsymbol{\sigma}$ and $\dot{\boldsymbol{\varepsilon}}^0$ are, respectively, the elastic compliance, the viscoplastic compliance, the strain rate, the true stress, and the back-extrapolated strain rate for the grain. $\overline{\mathbf{M}}^e$, $\overline{\mathbf{M}}^\nu$, $\dot{\mathbf{E}}$, $\boldsymbol{\Sigma}$ and $\dot{\mathbf{E}}^0$ are the corresponding terms for the HEM. Equations 6.7 and 6.8 can be written in component form as follows:

$$\dot{\varepsilon}_{ij} = M_{ijkl}^e \dot{\sigma}_{kl} + M_{ijkl}^\nu \sigma_{kl} + \dot{\varepsilon}_{ij}^0 \quad (6.9)$$

$$\dot{E}_{ij} = \overline{M}_{ijkl}^e \dot{\Sigma}_{kl} + \overline{M}_{ijkl}^\nu \Sigma_{kl} + \dot{E}_{ij}^0 \quad (6.10)$$

The grain-level stress and strain rates are related self-consistently to the corresponding values for the HEM (Turner and Tomé, 1994; Wang *et al.*, 2010c):

$$(\dot{\boldsymbol{\varepsilon}} - \dot{\mathbf{E}}) = -\tilde{\mathbf{M}}^e : (\dot{\boldsymbol{\sigma}} - \dot{\boldsymbol{\Sigma}}) - \tilde{\mathbf{M}}^\nu : (\boldsymbol{\sigma} - \boldsymbol{\Sigma}) \quad (6.11)$$

where $\tilde{\mathbf{M}}^e$ and $\tilde{\mathbf{M}}^\nu$ are the interaction tensors that can be given by:

$$\tilde{\mathbf{M}}^e = (\mathbf{I} - \mathbf{S}^e)^{-1} : \mathbf{S}^e : \overline{\mathbf{M}}^e$$

$$\tilde{\mathbf{M}}^\nu = (\mathbf{I} - \mathbf{S}^\nu)^{-1} : \mathbf{S}^\nu : \overline{\mathbf{M}}^\nu$$

Where \mathbf{S}^e and \mathbf{S}^ν are the elastic and visco-plastic Eshelby tensors for a given grain, respectively, and \mathbf{I} is the identity tensor.

As mentioned before, a linearization scheme shall be used to obtain Equation 6.5. From previous result (Wang *et al.*, 2010b), it can be observed that the Affine self-consistent model of the EVPSC-TDT model performs the best features of HCP alloy such as magnesium. In this chapter, Affine self-consistent model of the EVPSC model is used.

The Affine method (Masson *et al.*, 2000; Lebensohn *et al.*, 2004) assumes a higher compliance and will have associated to a higher strain heterogeneity compared to secant method.

$$\mathbf{M}^{\nu,\text{aff}} = \frac{\dot{\gamma}_0}{\mathbf{m}} \sum_{\alpha} \left(\frac{\tau^{\alpha}}{\tau_{cr}^{\alpha}} \right)^{\frac{1}{m}-1} \frac{\mathbf{P}^{\alpha} \mathbf{P}^{\alpha}}{\tau_{cr}^{\alpha}}, \dot{\epsilon}^{0,\text{aff}} = \left(1 - \frac{1}{m}\right) \dot{\epsilon}^p \quad (6.12)$$

For details concerning the self-consistent equations associated with the different visco-plastic self-consistent algorithms, one can refer to Lebensohn *et al.* (2007)

6.2.2 Twinning mode

To model twinning, the author use the twinning and de-twinning (TDT) model proposed by Wang *et al.* (2012a). A detailed description of the TDT models for describing the plastic deformation that results from twinning and de-twinning is presented in Chapter 5. The TDT model treat twins as separate inclusions from the start and allow for any active twin variants to become a twin. The TDT model treat twins as new grains and there are no deformation constraints applied among the matrix and the twins.

In the TDT model, the evolution of twin volume fraction associated with α is governed by:

$$\dot{f}^{\alpha} = f(\dot{f}^{\alpha A} + \dot{f}^{\alpha C}) + f^{\alpha}(\dot{f}^{\alpha B} + \dot{f}^{\alpha D}) \quad (6.13)$$

Where f^0 is the volume fraction of the parent, i.e. $f^0 = 1 - f^{tw} = 1 - \sum_{\alpha} f^{\alpha}$, and superscripts A, B, C and D represent for Operations A, B, C and D, respective.

A threshold twin volume fraction is defined in the model to terminate twinning because rarely a grain can be fully twinned. Correspondingly, the TDT model introduces two statistical variables: accumulated twin fraction V^{acc} and effective twinned fraction V^{eff} . More specifically, V^{acc} and V^{eff} are the weighted volume fraction of the twinned region and volume fraction of twin terminated grains, respectively. The threshold volume fraction V^{th} is defined as $V^{th} = \min(1.0, A_1 + A_2 \frac{V^{eff}}{V^{acc}})$, where A_1 and A_2 are two material parameters. This aspect of the model may be viewed as accounting for sharp increase in the resistance to continued twin growth by the surrounding medium, once the threshold value is reached.

For both slip and twinning, the evolution of the critical resolved shear stress (CRSS) τ_{cr}^{α} as deformation proceeds is given by:

$$\dot{\tau}_{cr}^{\alpha} = \frac{d\hat{\tau}^{\alpha}}{d\Gamma} \sum_{\beta} h^{\alpha\beta} |\dot{\gamma}^{\beta}| \quad (6.14)$$

Where Γ is the total accumulated shear strain within the grain due to all slip and twinning systems, $\dot{\gamma}^{\beta}$ is the shear on a specific slip or twinning system β , and $\hat{\tau}^{\alpha}$ is an empirical Voce hardening law (with initial CRSS value τ_0 , initial hardening rate h_0 , and saturation stress $(\tau_0 + \tau_1)$).

6.3 Results and discussion

The material under consideration is a piece of hot rolled Magnesium AZ31 plate studied by Chapuis *et al.* (2014). The composition is Mg-3%Al-1%Zn-0.6%Mn. The

plate was annealed for homogenization at 400 °C for 1 h. The hot rolled and annealed plate has an average grain size of about 25 μm . The initial texture of the material was modeled as 3,000 discrete orientations and is shown in Figure 6.1 in terms of the $\{0001\}$, $\{10\bar{1}0\}$ and $\{11\bar{2}0\}$ pole figures. It is clear that the material exhibits a strong basal texture. In this chapter, the RD, TD and ND stand for the rolling, transverse and normal directions, respectively.

Uniaxial compression and channel-die compression are performed along different orientation with respect to the ND. More specifically, as shown in Figure 6.2, five different specimen orientations with tilt angles of $\alpha = 0^\circ, 30^\circ, 45^\circ, 60^\circ$ and 90° between the ND and loading direction (LD) are used in this study. The samples deformed in uniaxial compression are called UC-0, UC-30, UC-45, UC-60, UC-90 according to the angle between ND and LD. In addition, a sample was cut for compression test along RD called UC-RD. Similarly, the samples deformed in channel-die are designated as CD-0, CD-30, CD-45, CD-60, CD-90 and CD-RD. In channel-die compression, rolling direction of the plate (RD) is constrained for samples CD-0, CD-30, CD-45, CD-60 and CD-90. Test sample CD-RD is constrained along ND and compressed along RD. All the compression tests were performed at room temperature and at a strain rate 0.01s^{-1} .

The EVPSC-TDT model with the Affine self-consistent scheme is employed in the following simulations. The plastic deformation of magnesium AZ31 alloy is assumed to be accommodated by basal ($\{0001\}\langle 11\bar{2}0\rangle$), prismatic ($\{10\bar{1}0\}\langle 11\bar{2}0\rangle$), pyramidal $\langle \mathbf{a}+\mathbf{c} \rangle$ ($\{11\bar{2}2\}\langle 11\bar{2}3\rangle$) slip, tensile twinning ($\{10\bar{1}2\}\langle 10\bar{1}1\rangle$) as well as compression twinning ($\{10\bar{1}1\}\langle 10\bar{1}\bar{2}\rangle$). In all the slip/twinning systems, the reference slip/twinning rate $\dot{\gamma}_0$ and the rate sensitivity m are prescribed to be the same:

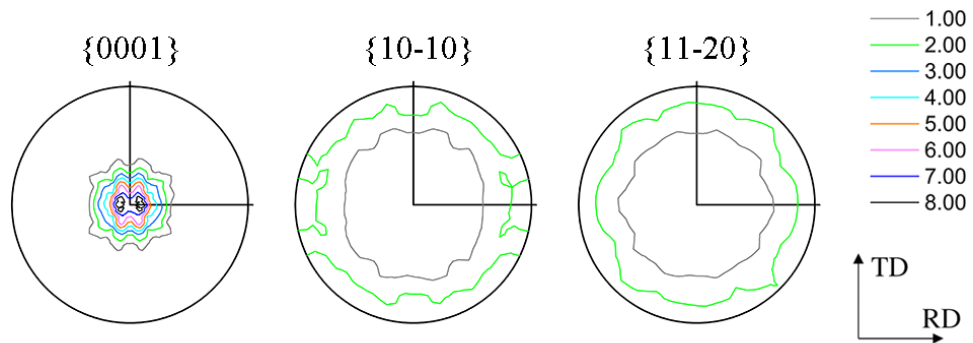


Figure 6.1: Initial texture presented in terms of the $\{0001\}$, $\{10\bar{1}0\}$ and $\{11\bar{2}0\}$ pole figures.

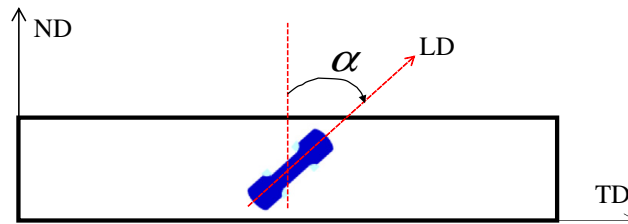


Figure 6.2: Schematic representation of a uniaxial compression sample with an angle α rotating around the RD from the ND to the loading direction (LD).

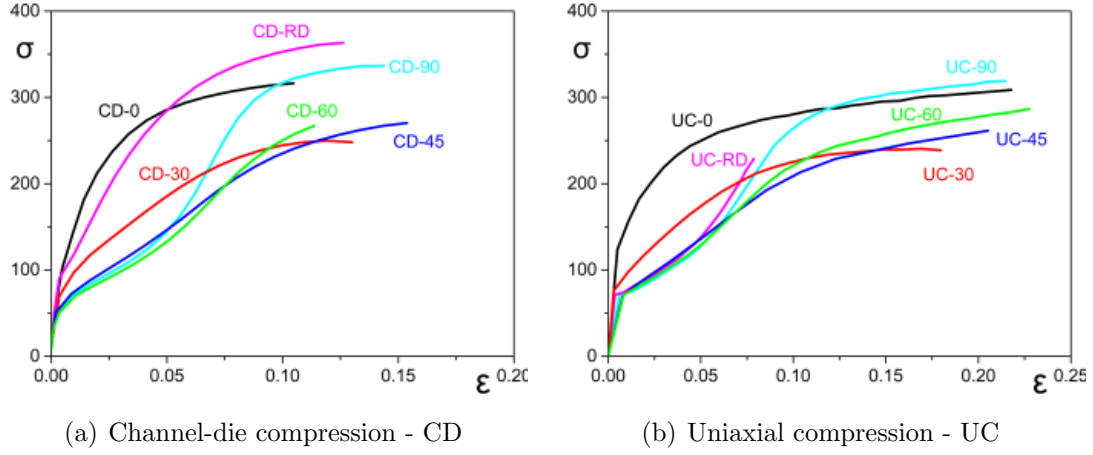


Figure 6.3: Experimental true stress and strain curves under (a) channel-die compression (CD) and (b) uniaxial compression (UC).

$\dot{\gamma}_0 = 0.001\text{s}^{-1}$ and $m = 0.05$, respectively. The room temperature elastic constants of the magnesium alloy are assumed to be close to those of Mg single crystal: $C_{11} = 58.0$, $C_{12} = 25.0$, $C_{13} = 20.8$, $C_{33} = 61.2$, and $C_{44} = 16.6\text{GPa}$ (Simmons and Wang, 1971).

Figure 6.3 shows the experimental stress-strain curves of the samples deformed in uniaxial compression and channel-die compression; these curves will be used to compare with simulated result.

It is found that the orientation-dependence of the deformation behavior is very pronounced in compression. The stress and strain curve of the material under compression along the ND (ND-0, $\alpha = 0^\circ$) exhibits a typical slip dominated plastic deformation, while the importance of twinning under compression along the TD (ND-90, $\alpha = 90^\circ$) is clearly revealed by the characteristic S-shape of the flow curve. The influence of tensile twinning increases as the tilt angle α increases from zero. No inflection point is visible for $\alpha = 30^\circ$. For $\alpha = 45^\circ$ and $\alpha = 60^\circ$, the flow curves are clearly S-shaped, similar to compression along the TD (ND-90, $\alpha = 90^\circ$). From the shape of the flow curves alone Figure 6.3, it can be surmised that the compression tests

cover a wide range of twinning activities: from a deformation process dominated by twinning to a case where twinning is negligible.

As stated in previous section, there are five different slip/twinning systems taken into account while simulate channel-die and uniaxial compression. The parameters being adjusted for each slip and twinning system are initial CRSS τ_0 , the initial hardening rate θ_0 , the asymptotic hardening rate θ_1 , and the back-extrapolated CRSS τ_1 . According to previous attempt at fitting EVPSC output to this data set, latent hardening $h_{\alpha\beta}$ simplified as two part: latent hardening between basal and slips $h_{s,basal}$ and latent hardening between tensile twin and slips $h_{s,et}$. Together with TDT threshold values A_1 and A_2 for tensile twinning and compression twin, the total number of material parameters is $20 + 5 + 5 + 4 = 34$. It is nearly impossible to tune using the traditional method.

It is hard to uniquely determined such a large number of material parameters. Meanwhile, there are experimental result of compression test for same piece of material in different directions. So that it is possible to significantly reduce the number of suitable parameter combinations by introducing more constraints. However, that also means increasing difficulty on finding a suitable parameter combination.

Studies showed that minimum numbers of experimental data sets is enough to determine the material parameters for EVPSC-TDT model. In this chapter, in order to get most accurate result, extract experimental data are used to constrain the fitting result. This research used genetic algorithm approach to fit stress-strain curves of 6 groups of experiments: CD-0, CD-45, CD-90, CD-RD, UC-0 and UC-45. Other experimental data are used to compare with predicted result.

After some trial to find a good balance between total running time and the final

quality of the results, a fitting procedure is developed. With 100 individuals in each generation, the algorithm run for a total of 30 generations. It took roughly one week to finished. The material parameters associated with the EVPSC-TDT model are listed in Table 6.1.

Mode	τ_0 (MPa)	τ_1 (MPa)	θ_0 (MPa)	θ_1 (MPa)	$h^{s,basal}$	$h^{s,et}$	A_1	A_2
Basal	4	21	88	28	1	1		
Prismatic	33	75	1100	48	1.5	1		
Pyramidal	54	60	2000	0	1.7	1		
Tensile Twin	23	18	130	0	1	1	0.6	0.8
Compression Twin	125	10	100	0	1	1	0.6	0.8

Table 6.1: List of the material parameters in the EVPSC-TDT model.

Figure 6.4-6.8 present the measured and simulated true stress and true stain curves and activities for the experiments. It is found that the EVPSC-TDT model can fit the experimental curves very well. Also, the parameter set determined by genetic algorithm approach is accurate.

Figure 6.4 (a) and (c) show the measured and simulated true stress and true stain curve under uniaxial compression and channel-die compression along ND. Figure 6.4 (b) and (d) are relative activities of slip/twinning under CD-0 and UC-0. As expected, for both channel-die compression and uniaxial compression, there is negligible tensile twinning activities. Mostly Basal and Pyramidal slip accommodate in the plastic deformation, while very little Prismatic slip activity is predicted by the model. The flow stress of the CD-0 and UC-0 reach a ceiling limited by compression twin softening effect. There is strong activity of compression twinning since the compression direction is parallel to ND.

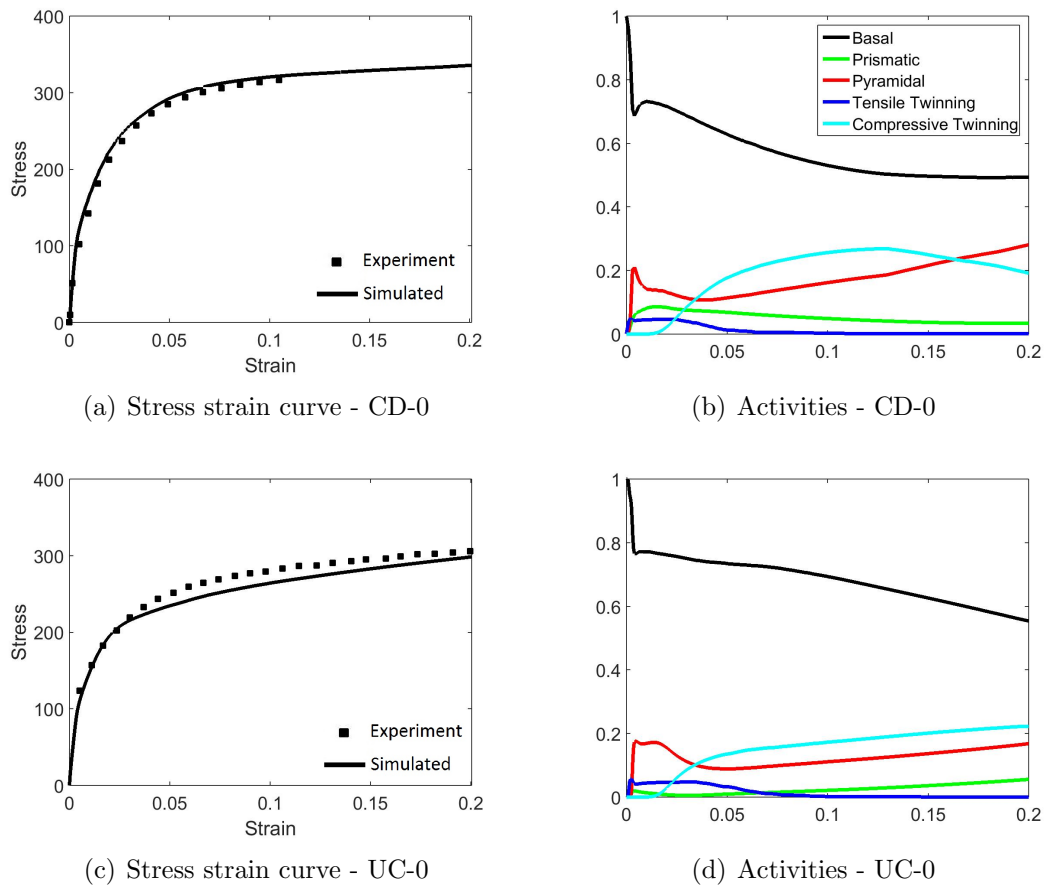


Figure 6.4: Experiment (symbols) and simulated (solid lines) stress - strain curves and activities under (a,b) CD-0; (c,d) UC-0.

Figure 6.5 (a) and (b) present true stress and true strain curve and relative activities under channel-die compression along $\alpha = 90^\circ$ (CD-90). The characteristic S-shape of the flow curve shows a typical twinning effect. At strains $|\varepsilon| < 0.04$, tensile twinning is very active, most grains reorient their c-axis along the TD. The remaining plasticity is accommodated by Basal slip. For strains $|\varepsilon| > 0.05$, model predicts increasing Basal slip, Pyramidal slip activity and little Prismatic slip, When the tensile twinning activity is dramatically reduced. In channel-die compression along $\alpha = 90^\circ$, there is tension effect through-thickness direction, so that limited compression twinning was activated. Almost no compression twins are visible in experiment.

Stress and strain curve and relative activities under channel-die compression along RD (CD-RD) are showed in Figure 6.5 (c) and (d). The CD-RD sample is compression along RD , constrained along ND. According to the experiment(Chapuis *et al.*, 2014), this sample deformed mainly with prismatic slip, that matched predicted activities.

Figure 6.6 shows the measured and simulated stress-strain curves and activities under channel-die compression along (a, b) $\alpha = 30^\circ$ (CD-30), (c, d) $\alpha = 45^\circ$ (CD-45) and (e, f) $\alpha = 60^\circ$ (CD-60). CD-45 is fitting result , the others are predictions. The agreement between the measured and predicted stress and strain curves is good. It is also observed that basal slip is the most active mechanism in plastic deformation. Tensile twinning is activated at small strains($|\varepsilon| < 0.04$). The flow curves are slightly S-shaped, similar to CD-90(Figure 6.5 (a)). It can be noticed that the influence of tensile twinning increases, and the influence of compression twinning decreases as the tilt angle α increase.

Figure 6.7 is the measured and simulated stress-strain curves and activities under uniaxial compression along (a,b) $\alpha = 30^\circ$ (UC-30), (c,d) $\alpha = 45^\circ$ (UC-45) and (e,f)

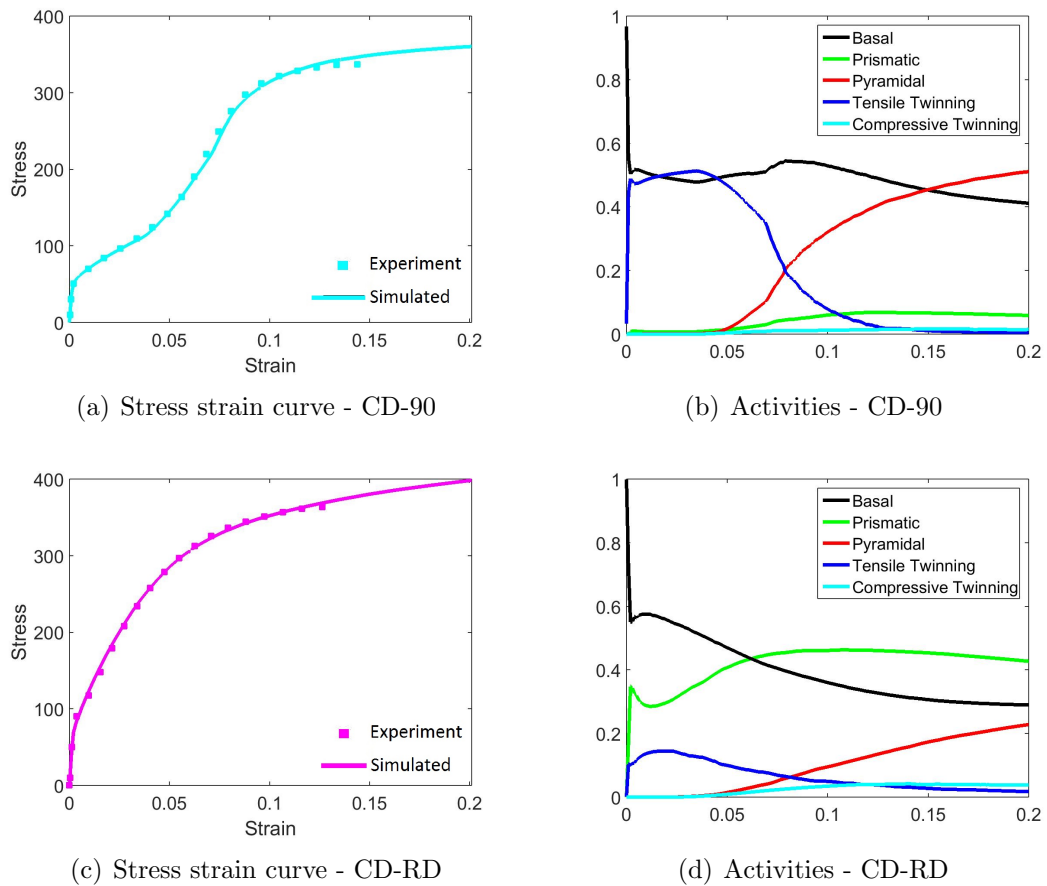


Figure 6.5: Experiment (symbols) and simulated (solid lines) stress - strain curves and activities under (a,b) CD-90; (c,d) CD-RD.

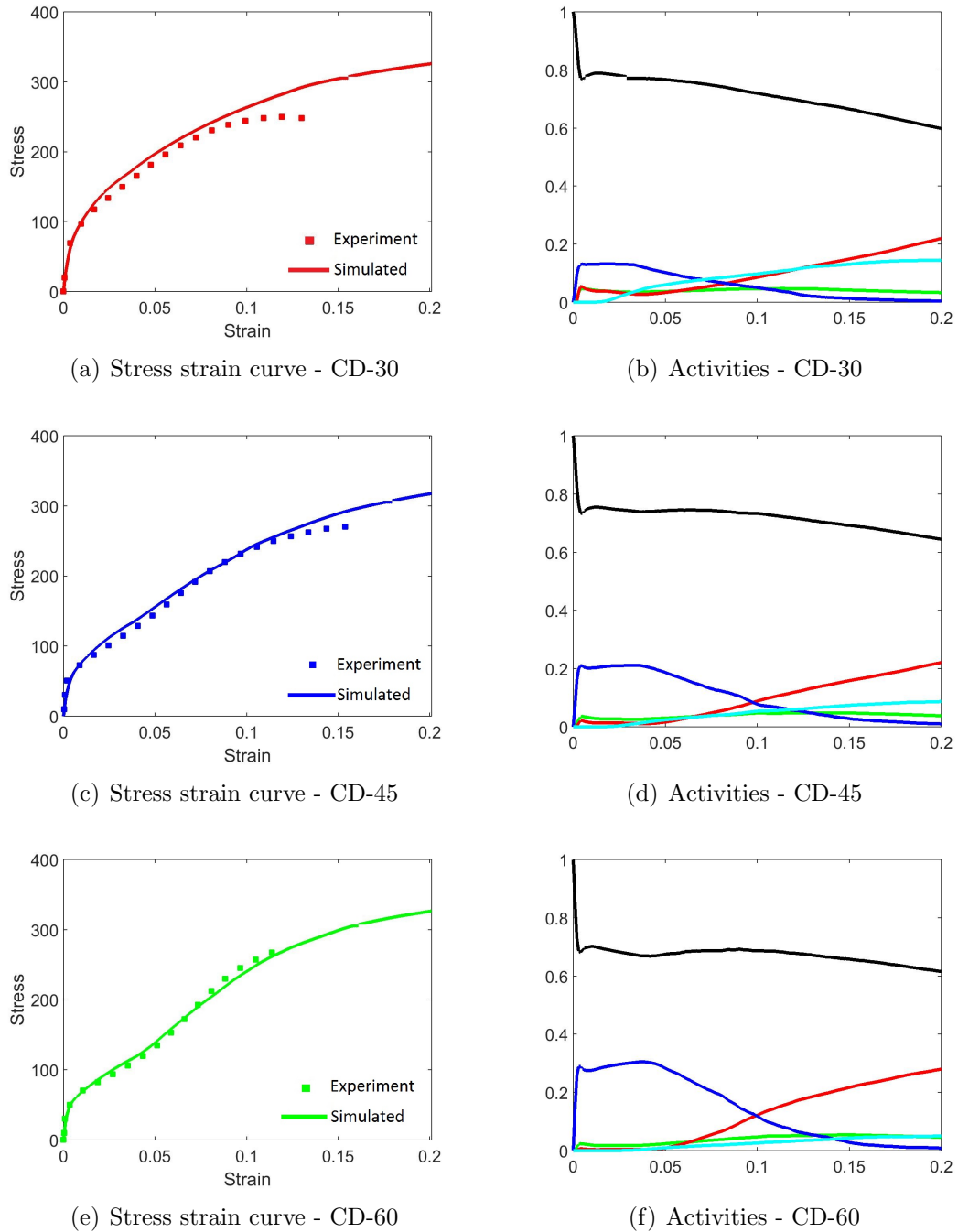


Figure 6.6: Experiment (symbols) and simulated (solid lines) stress - strain curves and activities under (a,b) CD-30; (c,d) CD-45; (e,f) CD-60.

$\alpha = 60^\circ$ (UC-60). Similar to channel-die compression in Figure 6.6, the deformation is mostly accommodated by basal slip and tensile twinning at small strains. As tilt angle α increase, the influence of tensile twinning increases, the flow curve shows more significant S-shaped. Generally, the simulated result predicts well the measured stress and strain curve.

The measured and predicted true stress true strain curve and activity under uniaxial compression along $\alpha = 90^\circ$ (UC-90) are shown in Figure 6.8(a) and 6.8(b). The flow curve has a clearly S-shape. This characteristic reveal that tensile twinning is important under uniaxial compression along TD(UC-90). However, the predicted result underestimates the stress by 5-8% for strain $|\varepsilon| > 0.1$.

Figure 6.8(c) and 6.8(d) are the measured and predicted true stress true strain curve and activity under uniaxial compression along RD. Since the initial texture of the plate exhibits in-plane symmetric, the simulated flow curve and activities of UC-90 and UC-RD almost the same. The plastic deformation is accommodated mostly by basal and prismatic. Because the sample deformed in in-plane compression which ND is under the tensile effect, there is a clear tensile twinning activated, and compression twinning occur rarely.

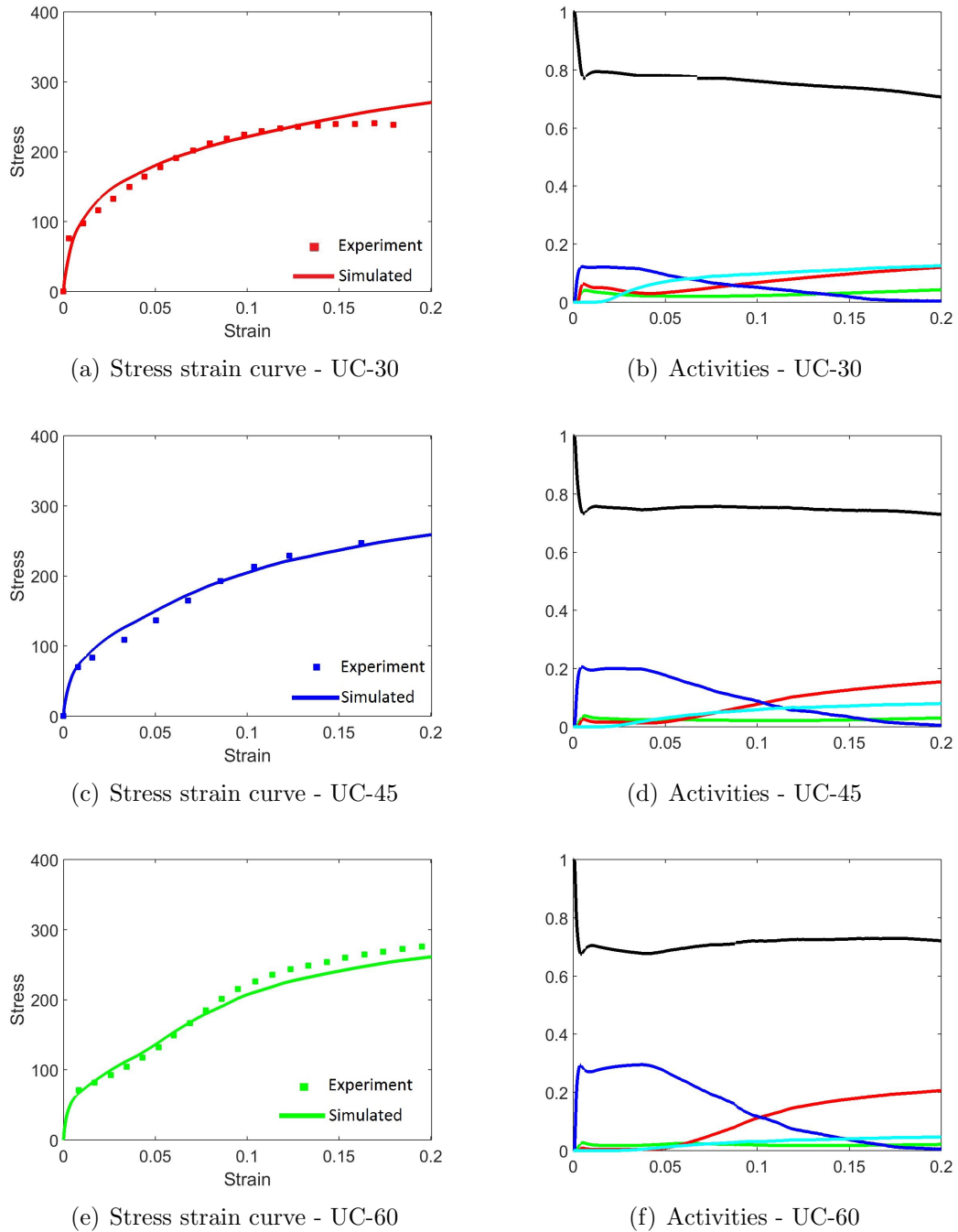


Figure 6.7: Experiment (symbols) and simulated (solid lines) stress - strain curves and activities under (a,b) UC-30; (c,d) UC-45; (e,f) UC-60.

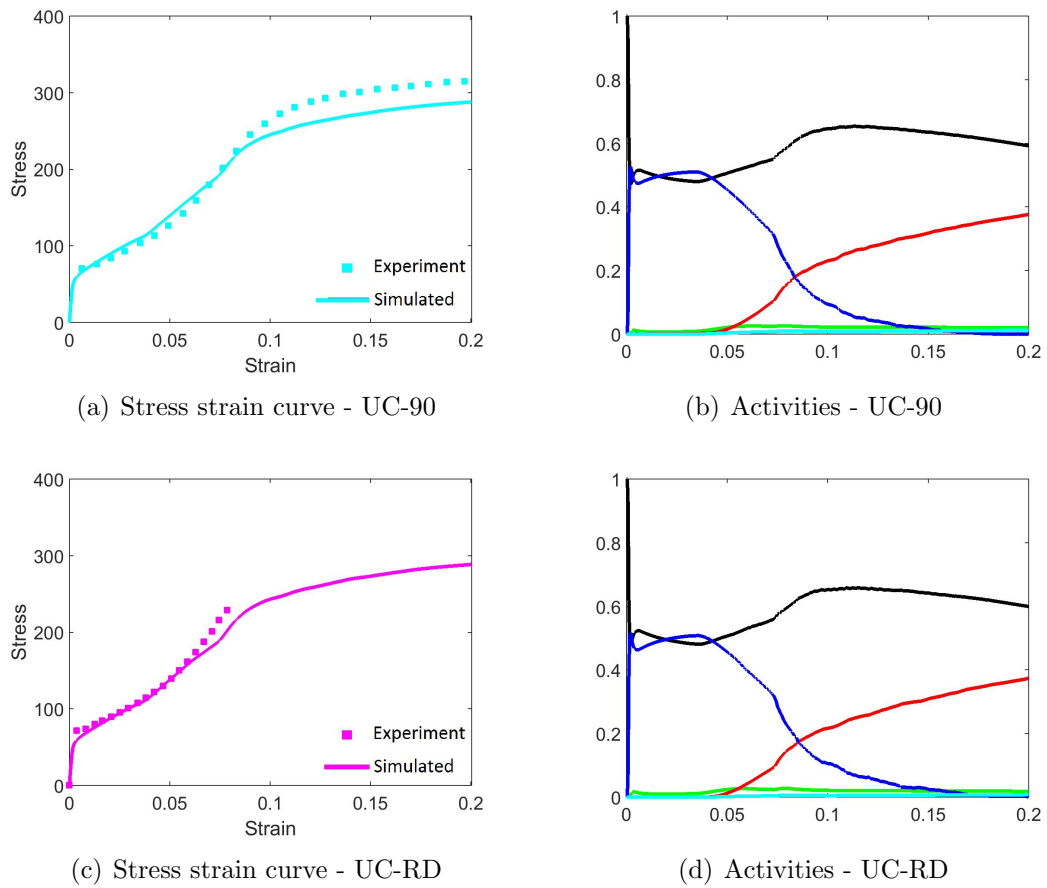


Figure 6.8: Experiment (symbols) and simulated (solid lines) stress - strain curves and activities under (a,b) UC-90; (c,d) UC-RD.

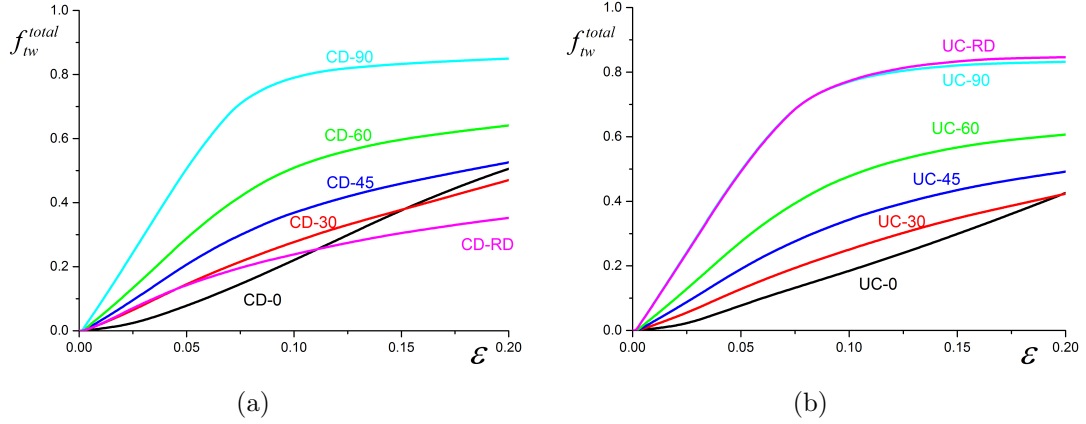


Figure 6.9: Predicted total twin volume fraction under (a) channel-die compression, (b) uniaxial compression along different tilt angles.

Figure 6.9 presents the predicted evolution of twin volume fraction as a function of compressive strain along different tilt angles. Figure 6.9(a) is total twin volume fraction under channel-die compression, and Figure 6.9(b) is total twin volume fraction under uniaxial compression.

Twin volume fraction of (a) tensile twinning and (b) compression twinning under channel-die compression are showed in Figure 6.10. It is found that with increasing tilt angle α , volume fraction of tensile twinning increases monotonically. It is also found that, for tensile twinning, except in the case of CD-0 which twinning is very low, the strain at when the twin volume fraction saturated increases with decreasing the tilt angle α . This implies that with the tilt angle α decreases, the peak of twinning activity also decreases, but the relative twinning activity reduces more gradually as function of strain. This is consistent with the predicted slip/twinning activities shown in Figure 6.4-6.8.

The total amount of compression twinning is the highest for the CD-0 sample and decreases with increasing tile angle α .

The total twin volume fraction is sum of twin volume fraction of tensile twinning and compression twinning. When tilt angle α is small, e.g. CD-0, tensile twinning fraction is very low and compression twinning is higher. Compression twinning is the major twinning mode, it contribute most in total twin volume fraction. As tilt angle α increase, twin volume fraction of tensile twinning increases, while twinning volume fraction of compression twinning decrease. Tensile twinning becomes major twinning mode. This coincide with predicted activities.

The predicted $\{11\bar{1}2\}$ tensile twinning twin volume fraction for channel-die compression along RD (CD-RD) is about 30%. That meets the experimental result which said tensile twinning consumed about about 30-40% of the sample (Chapuis *et al.*, 2014).

Figure 6.11 shows twin volume fraction of (a) tensile twinning and (b) compression twinning under uniaxial compression. It is similar to channel-die (Figure 6.10), tensile twinning twin volume fraction increases monotonically with increasing tilt angle α , while compressive twinning twin volume fraction decreases.

Uniaxial compression along RD is symmetric to uniaxial compression along TD (UC-90) because of the texture of the plate is near in-plane isotropy. Twin volume fraction of both tensile and compressive twinning along UC-RD are close to UC-90.

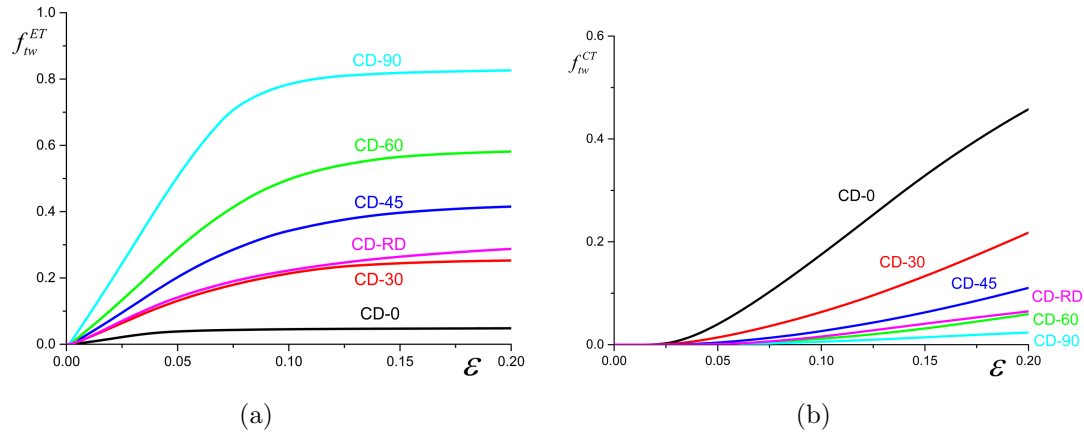


Figure 6.10: Predicted twin volume fraction of (a) tensile twinning and (b) compression twinning under channel-die compression.

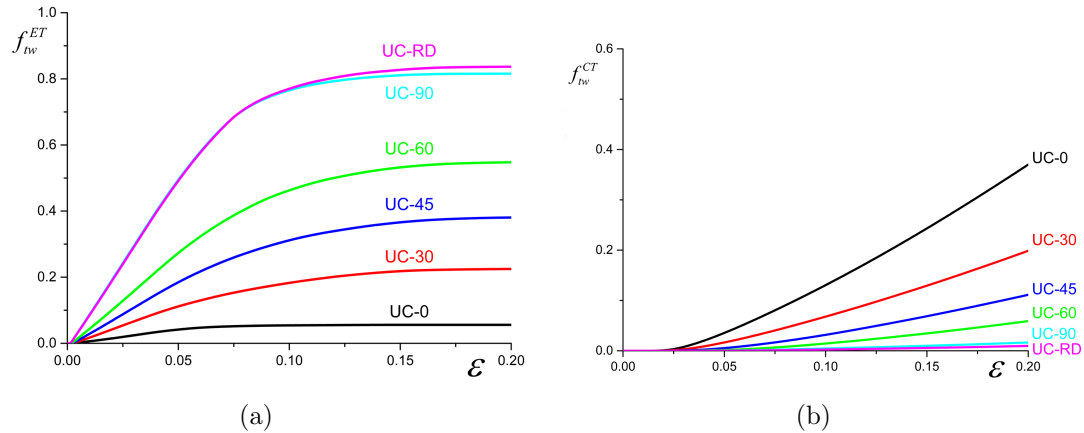


Figure 6.11: Predicted twin volume fraction of (a) tensile twinning and (b) compression twinning under uniaxial compression.

Figure 6.12 and 6.13 exhibit texture evolution by the predicted $\{0001\}$, $\{10\bar{1}0\}$ and $\{11\bar{2}0\}$ pole figures at different strain levels under channel-die compression and uniaxial compression along ND, 45° , 90° (TD). Although the channel-die compression samples have their RD constrained while uniaxial compression samples do not, there texture evolution are similar.

In the case of $\alpha = 0^\circ$ (Figure 6.12 (a)), the initial basal texture is progressively enhanced with straining by Basal slip and Pyramidal slip. Under channel-die compression along $\alpha = 90^\circ$ (Figure 6.12 (c)), the main contribution of texture evolution is from the reorientation due to tensile twinning. In the middle of case $\alpha = 0^\circ$ and $\alpha = 90^\circ$, the case of $\alpha = 45^\circ$ (Figure 6.12 (b)), the deformation is a combination of twinning and slip. At small strains, texture evolution is mainly caused by tensile twinning, while at large strains, the main factors are Basal slip and Pyramidal slip.

Generally, the predicted result successfully reproduce the texture evolution during deformation. The uniaxial compression pole figure consistent with simulation result in Guo *et al.* (2015b).

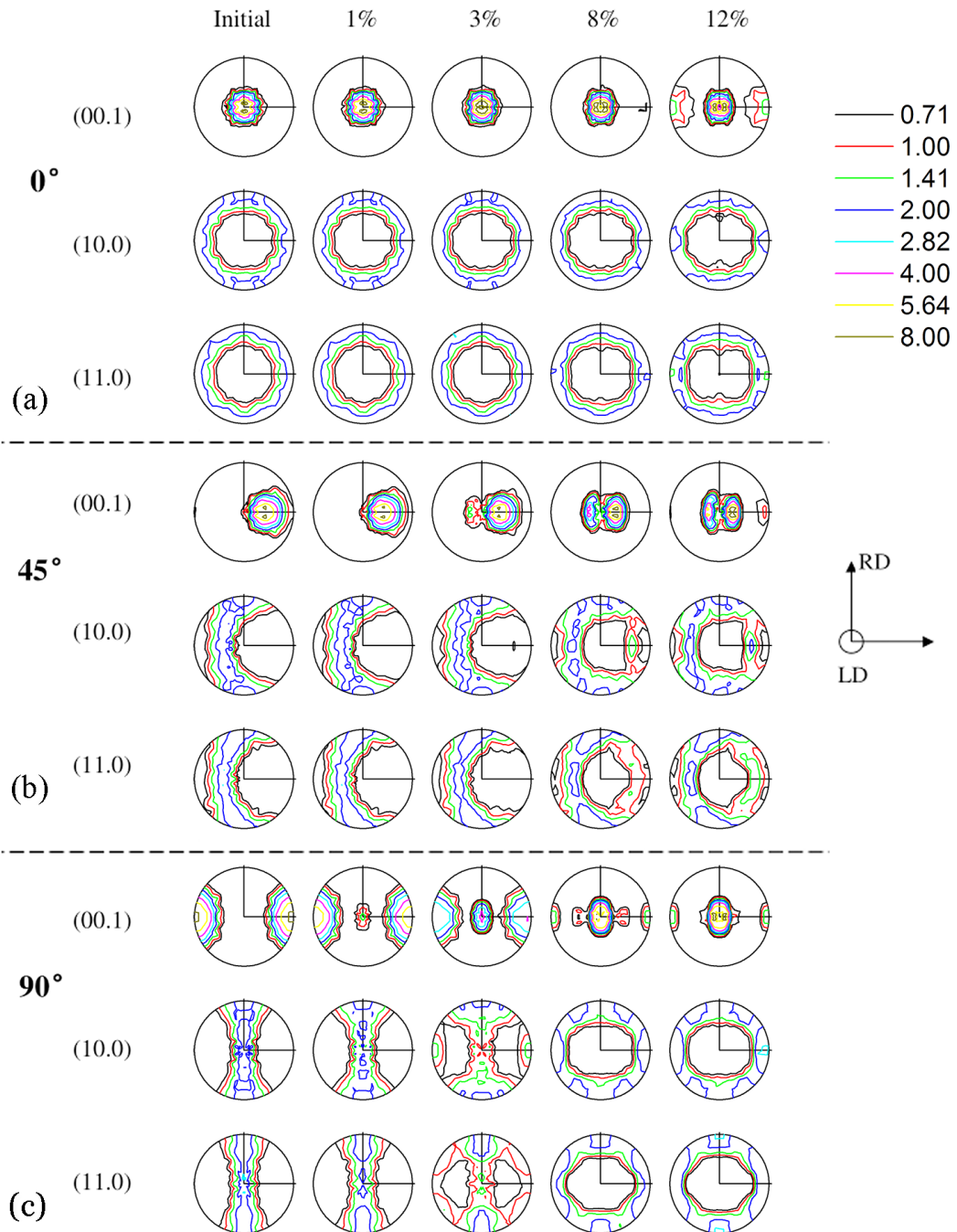


Figure 6.12: Predicted texture evolution under Channel-die compression along (a) $\alpha = 0^\circ$; (b) $\alpha = 45^\circ$; (c) $\alpha = 90^\circ$.

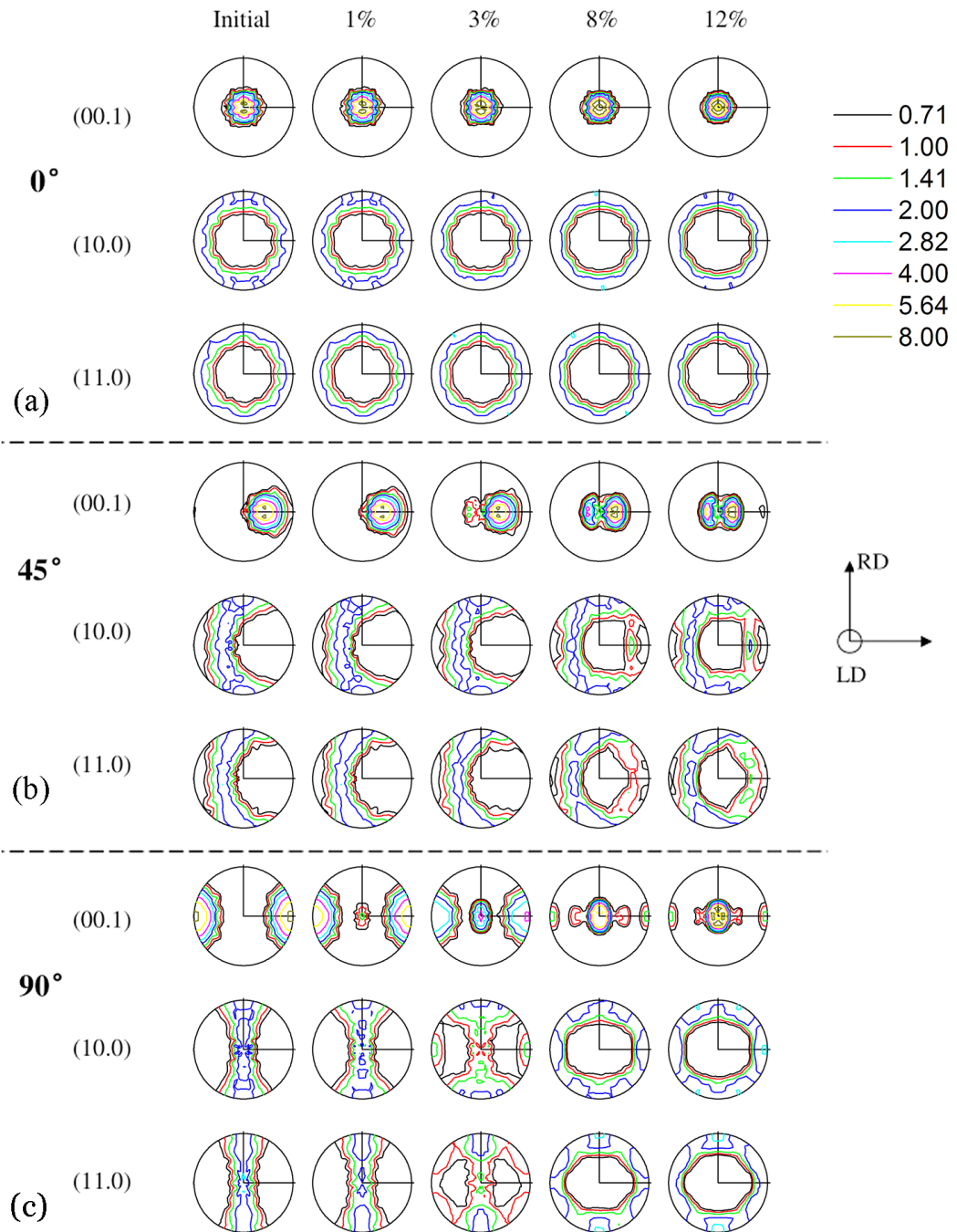


Figure 6.13: Predicted texture evolution under uniaxial compression along (a) $\alpha = 0^\circ$; (b) $\alpha = 45^\circ$; (c) $\alpha = 90^\circ$.

6.4 Conclusion

In this chapter, genetic algorithm approach is used to tune materials parameters in EVPSC-TDT model of a magnesium AZ31 plate. By fitting the macroscopic stress-strain curves of channel-die compression and uniaxial compression, the genetic algorithm approach obtained a group of best fit parameters.

Overall, the genetic algorithm approach give a good and reliable fitting result for the AZ31 plate. The simulated results, including stress-strain curve, twin volume fraction and texture, fit the experimental result well. In contrast, it is extremely difficult to determine by traditional method because there are so many experimental data needed to fit at the same time. It is almost impossible to find a set of fitting parameters using the traditional method.

It can be concluded that the genetic algorithm approach is an effective method in tuning material parameters in EVPSC model. Genetic algorithm approach can accomplish the task that the traditional method can not do. Genetic algorithm approach can replace the traditional method in further research.

Chapter 7

General conclusions

In this thesis, a genetic algorithm approach is developed to determine material parameters which involve in Elastic Visco-Plastic Self-Consistent (EVPSC) models (Wang *et al.*, 2010c). This new fitting method is evaluated by studying large strain behavior of magnesium alloys under different deformation processes through EVPSC model.

The genetic algorithm approach is firstly used to determining plasticity parameters for magnesium ZEK100 sheet. The parameters is determined by fitting simulated to experimental uniaxial tension and compression curves along RD (RD-T, RD-C) and compression along the TT (TT-C), then used to predict uniaxial tension and compression along the TD (TD-T, TD-C) and the 45° direction (45-T, 45-C). The prediction of stress-strain curve, R values and texture evolution proves that the results fitted by genetic algorithm approach is correct.

By fitting the deformation of randomly textured magnesium (Máthis *et al.*, 2015), which only has minimal data inputted as constrain to correct the fitting, genetic algorithm approach still give a good performance in a very short time. That is what tradition method hard to achieve.

As for a task nearly unable to do manually, the rolled magnesium AZ31 plate deformed along six different directions under both uniaxial compression and plane strain compression (Chapuis *et al.*, 2014), the results fitted by genetic algorithm approach present good prediction on stress-strain response, twin volume fraction and texture evolution. Although it cost more time, genetic algorithm approach successfully finished the extremely hard fitting task.

All in all, genetic algorithm approach can get good fitting results for polycrystal plasticity models in less time. It also has the advantage of easy to use which can significantly reduce the workload of researchers. The genetic algorithm approach might be able to replace the traditional trial-and-error approach in future research about EVPSC model.

Bibliography

- Abdolvand, H. and Daymond, M. R. (2012). Internal strain and texture development during twinning: comparing neutron diffraction measurements with crystal plasticity finite-element approaches. *Acta Materialia*, **60**(5), 2240–2248.
- Agnew, S. R. and Duygulu, Ö. (2005). Plastic anisotropy and the role of non-basal slip in magnesium alloy AZ31B. *International Journal of plasticity*, **21**(6), 1161–1193.
- Agnew, S. R., Yoo, M. H., and Tome, C. N. (2001). Application of texture simulation to understanding mechanical behavior of Mg and solid solution alloys containing Li or Y. *Acta Materialia*, **49**(20), 4277–4289.
- Agnew, S. R., Tomé, C. N., Brown, D. W., Holden, T. M., and Vogel, S. C. (2003). Study of slip mechanisms in a magnesium alloy by neutron diffraction and modeling. *Scripta Materialia*, **48**(8), 1003–1008.
- Agnew, S. R., Brown, D. W., and Tomé, C. N. (2006). Validating a polycrystal model for the elastoplastic response of magnesium alloy AZ31 using in situ neutron diffraction. *acta Materialia*, **54**(18), 4841–4852.
- Agnew, S. R., Mulay, R. P., Polesak, F., Calhoun, C. A., Bhattacharyya, J. J., and Clausen, B. (2013). In situ neutron diffraction and polycrystal plasticity modeling of a Mg–Y–Nd–Zr alloy: effects of precipitation on individual deformation mechanisms. *Acta Materialia*, **61**(10), 3769–3780.
- Asari, R. J. and Needleman, A. (1985). Texture development and strain hardening in rate dependent polycrystal. *Acta metallurgica et Materialia*, **33**, 923–953.

- Aydiner, C. C., Bernier, J. V., Clausen, B., Lienert, U., Tomé, C. N., and Brown, D. W. (2009). Evolution of stress in individual grains and twins in a magnesium alloy aggregate. *Physical Review B*, **80**(2), 024113.
- Battaini, M. (2008). *Deformation behaviour and twinning mechanisms of commercially pure titanium alloys*. Ph.D. thesis, Monash University. Faculty of Engineering. Department of Materials Engineering.
- Beyerlein, I. J. and Tomé, C. N. (2010). A probabilistic twin nucleation model for HCP polycrystalline metals. In *Proceedings of the Royal Society of London A: Mathematical, Physical and Engineering Sciences*, volume 466, pages 2517–2544.
- Bohlen, J., Nürnberg, M. R., Senn, J. W., Letzig, D., and Agnew, S. R. (2007). The texture and anisotropy of magnesium–zinc–rare earth alloy sheets. *Acta Materialia*, **55**(6), 2101–2112.
- Bohlen, J., Yi, S., Letzig, D., and Kainer, K. U. (2010). Effect of rare earth elements on the microstructure and texture development in magnesium–manganese alloys during extrusion. *Materials Science and Engineering: A*, **527**(26), 7092–7098.
- Brown, D. W., Agnew, S. R., Bourke, M., Holden, T. M., Vogel, S., and Tomé, C. N. (2005). Internal strain and texture evolution during deformation twinning in magnesium. *Materials Science and Engineering: A*, **399**(1), 1–12.
- Canova, G. R. (1994). Self-consistent methods: application to the prediction of the deformation texture of polyphase materials. *Materials Science and Engineering: A*, **175**(1), 37–42.

- Čapek, J., Máthis, K., Clausen, B., Stráská, J., Beran, P., and Lukáš, P. (2014). Study of the loading mode dependence of the twinning in random textured cast magnesium by acoustic emission and neutron diffraction methods. *Materials Science and Engineering: A*, **602**, 25–32.
- Capolungo, L., Marshall, P. E., McCabe, R. J., Beyerlein, I. J., and Tomé, C. N. (2009). Nucleation and growth of twins in Zr: a statistical study. *Acta Materialia*, **57**(20), 6047–6056.
- Chapuis, A., Wang, B., and Liu, Q. (2014). A comparative study between uniaxial compression and plane strain compression of Mg–3Al–1Zn alloy using experiments and simulations. *Materials Science and Engineering: A*, **597**, 349–358.
- Christian, J. W. (2002). *The theory of transformations in metals and alloys*. Newnes.
- Christian, J. W. and Mahajan, S. (1995). Deformation twinning. *Progress in Materials Science*, **39**(1), 1–157.
- Clausen, B., Tomé, C. N., Brown, D. W., and Agnew, S. R. (2008). Reorientation and stress relaxation due to twinning: modeling and experimental characterization for Mg. *Acta Materialia*, **56**(11), 2456–2468.
- Dawson, P. R., MacEwen, S. R., and Wu, P. D. (2003). Advances in sheet metal forming analyses: dealing with mechanical anisotropy from crystallographic texture. *International Materials Reviews*, **48**(2), 86–122.
- De Garmo, E. P., Black, J. T., and Kohser, R. A. (2011). *DeGarmo's materials and processes in manufacturing*. John Wiley & Sons.

- Dreyer, C. E., Chiu, W. V., Wagoner, R. H., and Agnew, S. R. (2010). Formability of a more randomly textured magnesium alloy sheet: Application of an improved warm sheet formability test. *Journal of Materials Processing Technology*, **210**(1), 37–47.
- Eshelby, J. D. (1957). The determination of the elastic field of an ellipsoidal inclusion, and related problems. In *Proceedings of the Royal Society of London A: Mathematical, Physical and Engineering Sciences*, volume 241, pages 376–396.
- Eyckens, P., Van Bael, A., and Van Houtte, P. (2009). Marciniak–Kuczynski type modelling of the effect of through-thickness shear on the forming limits of sheet metal. *International Journal of Plasticity*, **25**(12), 2249–2268.
- Flynn, P. W., Mote, J., and Dorn, J. E. (1961). On the thermally activated mechanism of prismatic slip in magnesium single crystals. *Transactions of the Metallurgical Society of AIME*, **221**(6), 1148–1154.
- Graff, S., Brocks, W., and Steglich, D. (2007). Yielding of magnesium: From single crystal to polycrystalline aggregates. *International Journal of Plasticity*, **23**(12), 1957–1978.
- Guo, X. Q., Wu, W., Wu, P. D., Qiao, H., An, K., and Liaw, P. K. (2013). On the Swift effect and twinning in a rolled magnesium alloy under free-end torsion. *Scripta Materialia*, **69**(4), 319–322.
- Guo, X. Q., Wang, H., Qiao, H., and Mao, X. B. (2015a). Numerical study of the large strain behavior of extruded magnesium alloy AM30 tube by elastic viscoplastic self-consistent model. *Materials & Design*, **79**, 99–105.

- Guo, X. Q., Chapuis, A., Wu, P. D., and Agnew, S. R. (2015b). On twinning and anisotropy in rolled Mg alloy AZ31 under uniaxial compression. *International Journal of Solids and Structures*, **64**, 42–50.
- Hantzsche, K., Bohlen, J., Wendt, J., Kainer, K. U., Yi, S. B., and Letzig, D. (2010). Effect of rare earth additions on microstructure and texture development of magnesium alloy sheets. *Scripta Materialia*, **63**(7), 725–730.
- Hill, R. (1965). Continuum micro-mechanics of elastoplastic polycrystals. *Journal of the Mechanics and Physics of Solids*, **13**(2), 89–101.
- Hill, R. (1967). The essential structure of constitutive laws for metal composites and polycrystals. *Journal of the Mechanics and Physics of Solids*, **15**(2), 79–95.
- Hirsch, J. and Al-Samman, T. (2013). Superior light metals by texture engineering: optimized aluminum and magnesium alloys for automotive applications. *Acta Materialia*, **61**(3), 818–843.
- Hosford, W. F. (1993). The mechanics of crystals and textured polycrystals. *Oxford University Press(USA)*, 1993,, page 248.
- Hutchinson, B., Jain, J., and Barnett, M. R. (2012). A minimum parameter approach to crystal plasticity modelling. *Acta materialia*, **60**(15), 5391–5398.
- Hutchinson, J. W. (1970). Elastic-plastic behaviour of polycrystalline metals and composites. In *Proceedings of the Royal Society of London A: Mathematical, Physical and Engineering Sciences*, volume 319(1537), pages 247–272.

- Hutchinson, J. W. (1976). Bounds and self-consistent estimates for creep of polycrystalline materials. In *Proceedings of the Royal Society of London A: Mathematical, Physical and Engineering Sciences*, volume 348, pages 101–127.
- Jain, A. and Agnew, S. R. (2007). Modeling the temperature dependent effect of twinning on the behavior of magnesium alloy AZ31B sheet. *Materials Science and Engineering: A*, **462**(1), 29–36.
- Juan, P. A., Berbenni, S., Barnett, M. R., Tomé, C. N., and Capolungo, L. (2014). A double inclusion homogenization scheme for polycrystals with hierarchal topologies: application to twinning in Mg alloys. *International Journal of Plasticity*, **60**, 182–196.
- Kocks, U. F., Tomé, C. N., and Wenk, H. R. (2000). *Texture and anisotropy: preferred orientations in polycrystals and their effect on materials properties*. Cambridge university press.
- Kröner, E. (1958). Berechnung der elastischen konstanten des vielkristalls aus den konstanten des einkristalls. *Zeitschrift für Physik*, **151**(4), 504–518.
- Kurukuri, S., Worswick, M. J., Bardelcik, A., Mishra, R. K., and Carter, J. T. (2014). Constitutive behavior of commercial grade ZEK100 magnesium alloy sheet over a wide range of strain rates. *Metallurgical and materials transactions A*, **45**(8), 3321–3337.
- Lebensohn, R. (1999). Modelling the role of local correlations in polycrystal plasticity using viscoplastic self-consistent schemes. *Modelling and Simulation in Materials Science and Engineering*, **7**(5), 739.

- Lebensohn, R. A. and Canova, G. R. (1997). A self-consistent approach for modelling texture development of two-phase polycrystals: application to titanium alloys. *Acta Materialia*, **45**(9), 3687–3694.
- Lebensohn, R. A. and Tomé, C. N. (1993). A self-consistent anisotropic approach for the simulation of plastic deformation and texture development of polycrystals: application to zirconium alloys. *Acta metallurgica et materialia*, **41**(9), 2611–2624.
- Lebensohn, R. A., Gonzalez, M. I., Tomé, C. N., and Pochettino, A. A. (1996). Measurement and prediction of texture development during a rolling sequence of Zircaloy-4 tubes. *Journal of nuclear materials*, **229**, 57–64.
- Lebensohn, R. A., Turner, P. A., and Canova, G. R. (1997). Recent advances in modelling polycrystals with complex microstructures. *Computational materials science*, **9**(1), 229–236.
- Lebensohn, R. A., Tomé, C. N., and Maudlin, P. J. (2004). A selfconsistent formulation for the prediction of the anisotropic behavior of viscoplastic polycrystals with voids. *Journal of the Mechanics and Physics of Solids*, **52**(2), 249–278.
- Lebensohn, R. A., Tomé, C. N., and Castañeda, P. P. (2007). Self-consistent modelling of the mechanical behaviour of viscoplastic polycrystals incorporating intragranular field fluctuations. *Philosophical Magazine*, **87**(28), 4287–4322.
- Lee, S. Y., Wang, H., Gharghoury, M. A., Nayyeri, G., Woo, W., Shin, E., Wu, P. D., Poole, W. J., Wu, W., and An, K. (2014). Deformation behavior of solid-solution-strengthened Mg –9 wt.% Al alloy: In situ neutron diffraction and elastic-viscoplastic self-consistent modeling. *Acta Materialia*, **73**, 139–148.

- Lévesque, J., Inal, K., Neale, K., and Mishra, R. (2010). Numerical modeling of formability of extruded magnesium alloy tubes. *International Journal of Plasticity*, **26**(1), 65–83.
- Lou, X. Y., Li, M., Boger, R. K., Agnew, S. R., and Wagoner, R. H. (2007). Hardening evolution of AZ31B Mg sheet. *International Journal of Plasticity*, **23**(1), 44–86.
- Masson, R., Bornert, M., Suquet, P., and Zaoui, A. (2000). An affine formulation for the prediction of the effective properties of nonlinear composites and polycrystals. *Journal of the Mechanics and Physics of Solids*, **48**(6), 1203–1227.
- Máthis, K., Csiszár, G., Čapek, J., Gubicza, J., Clausen, B., Lukáš, P., Vinogradov, A., and Agnew, S. R. (2015). Effect of the loading mode on the evolution of the deformation mechanisms in randomly textured magnesium polycrystals—comparison of experimental and modeling results. *International Journal of Plasticity*, **72**, 127–150.
- Mitchell, M. (1998). *An introduction to genetic algorithms*. MIT press.
- Molinari, A. and Tóth, L. S. (1994). Tuning a self consistent viscoplastic model by finite element results-I. modeling. *Acta Metallurgica et Materialia*, **42**(7), 2453–2458.
- Molinari, A., Canova, G. R., and Ahzi, S. (1987). A self consistent approach of the large deformation polycrystal viscoplasticity. *Acta Metallurgica*, **35**(12), 2983–2994.
- Molinari, A., Ahzi, S., and Kouddane, R. (1997). On the self-consistent modeling of elastic-plastic behavior of polycrystals. *Mechanics of Materials*, **26**(1), 43–62.

- Muránsky, O., Carr, D. G., Barnett, M. R., Oliver, E. C., and Šittner, P. (2008). Investigation of deformation mechanisms involved in the plasticity of AZ31 Mg alloy: in situ neutron diffraction and EPSC modelling. *Materials Science and Engineering: A*, **496**(1), 14–24.
- Muránsky, O., Carr, D. G., Šittner, P., and Oliver, E. C. (2009). In situ neutron diffraction investigation of deformation twinning and pseudoelastic-like behaviour of extruded AZ31 magnesium alloy. *International Journal of Plasticity*, **25**(6), 1107–1127.
- Neil, C. J. and Agnew, S. R. (2009). Crystal plasticity-based forming limit prediction for non-cubic metals: application to Mg alloy AZ31B. *International Journal of Plasticity*, **25**(3), 379–398.
- Oppedal, A. L., El Kadiri, H., Tomé, C. N., Kaschner, G. C., Vogel, S. C., Baird, J. C., and Horstemeyer, M. F. (2012). Effect of dislocation transmutation on modeling hardening mechanisms by twinning in magnesium. *International Journal of Plasticity*, **30**, 41–61.
- Partridge, P. G. (1967). The crystallography and deformation modes of hexagonal close-packed metals. *Metallurgical reviews*, **12**(1), 169–194.
- Poirier, P. P. and Le Hazif, R. (1976). Microscopie électronique et déformation plastique des métaux et alliages hexagonaux compacts. *Journal de Microscopie et de Spectroscopie Electroniques*, **1**, 595–607.
- Proust, G., Tomé, C. N., and Kaschner, G. C. (2007). Modeling texture, twinning and

- hardening evolution during deformation of hexagonal materials. *Acta Materialia*, **55**(6), 2137–2148.
- Proust, G., Tomé, C. N., Jain, A., and Agnew, S. R. (2009). Modeling the effect of twinning and detwinning during strain-path changes of magnesium alloy AZ31. *International Journal of Plasticity*, **25**(5), 861–880.
- Qiao, H., Wu, P. D., Wang, H., Gharghour, M. A., and Daymond, M. R. (2015a). Evaluation of elastic–viscoplastic self-consistent polycrystal plasticity models for zirconium alloys. *International Journal of Solids and Structures*, **71**, 308–322.
- Qiao, H., Agnew, S. R., and Wu, P. D. (2015b). Modeling twinning and detwinning behavior of Mg alloy ZK60A during monotonic and cyclic loading. *International Journal of Plasticity*, **65**, 61–84.
- Reed-Hill, R. E., Hirth, J. P., and Rogers, H. C. (1965). *Deformation twinning: proceedings*, volume 25. Gordon and Breach Science Publishers.
- Roberts, C. S. (1960). *Magnesium and its Alloys*. Wiley.
- Sachs, G. (1928). Plasticity problems in metals. *Transactions of the Faraday Society*, **24**, 84–92.
- Signorelli, J. W., Bertinetti, M. A., and Turner, P. A. (2009). Predictions of forming limit diagrams using a rate-dependent polycrystal self-consistent plasticity model. *International Journal of Plasticity*, **25**(1), 1–25.
- Simmons, G. and Wang, H. (1971). Single crystal elastic constants and calculated polycrystal properties.

- Solas, D. E. and Tomé, C. N. (2001). Texture and strain localization prediction using a N-site polycrystal model. *International Journal of Plasticity*, **17**(5), 737–753.
- Taylor, G. I. (1938). Plastic strain in metals. *Journal of the Institute of Metals*, **62**, 307–324.
- Tomé, C. N. (1999). Self-consistent polycrystal models: a directional compliance criterion to describe grain interactions. *Modelling and Simulation in Materials Science and Engineering*, **7**(5), 723.
- Tomé, C. N. and Kaschner, G. C. (2005). Modeling texture, twinning and hardening evolution during deformation of hexagonal materials. In *Materials Science Forum*, volume 495, pages 1001–1006.
- Tome, C. N., Canova, G. R., Kocks, U. F., Christodoulou, N., and Jonas, J. J. (1984). The relation between macroscopic and microscopic strain hardening in FCC polycrystals. *Acta metallurgica*, **32**(10), 1637–1653.
- Tomé, C. N., Lebensohn, R. A., and Kocks, U. F. (1991). A model for texture development dominated by deformation twinning: application to zirconium alloys. *Acta Metallurgica et Materialia*, **39**(11), 2667–2680.
- Tomé, C. N., Beyerlein, I. J., Wang, J., and McCabe, R. J. (2011). A multi-scale statistical study of twinning in magnesium. *JOM*, **63**(3), 19–23.
- Turner, P. A. and Tomé, C. N. (1994). A study of residual stresses in Zircaloy-2 with rod texture. *Acta Metallurgica et Materialia*, **42**(12), 4143–4153.
- Turner, P. A., Christodoulou, N., and Tomé, C. N. (1995). Modeling the mechanical response of rolled zircaloy-2. *International journal of plasticity*, **11**(3), 251–265.

- Van Houtte, P. (1978). Simulation of the rolling and shear texture of brass by the Taylor theory adapted for mechanical twinning. *Acta Metallurgica*, **26**(4), 591–604.
- Wang, H., Wu, P. D., and Gharghoury, M. A. (2010a). Effects of basal texture on mechanical behaviour of magnesium alloy AZ31B sheet. *Materials Science and Engineering: A*, **527**(15), 3588–3594.
- Wang, H., Raesinia, B., Wu, P. D., Agnew, S. R., and Tomé, C. N. (2010b). Evaluation of self-consistent polycrystal plasticity models for magnesium alloy AZ31B sheet. *International Journal of Solids and Structures*, **47**(21), 2905–2917.
- Wang, H., Wu, P. D., Tomé, C. N., and Huang, Y. (2010c). A finite strain elastic-viscoplastic self-consistent model for polycrystalline materials. *Journal of the Mechanics and Physics of Solids*, **58**(4), 594–612.
- Wang, H., Wu, Y., Wu, P. D., and Neale, K. W. (2010d). Numerical analysis of large strain simple shear and fixed-end torsion of HCP polycrystals. *Computers Materials and Continua*, **19**(3), 255.
- Wang, H., Wu, P. D., Boyle, K. P., and Neale, K. W. (2011). On crystal plasticity formability analysis for magnesium alloy sheets. *International Journal of Solids and Structures*, **48**(6), 1000–1010.
- Wang, H., Wu, P. D., Tomé, C. N., and Wang, J. (2012a). A constitutive model of twinning and detwinning for hexagonal close packed polycrystals. *Materials Science and Engineering: A*, **555**, 93–98.
- Wang, H., Wu, P. D., Tomé, C. N., and Wang, J. (2012b). Study of lattice strains in magnesium alloy AZ31 based on a large strain elastic-viscoplastic self-consistent

- polycrystal model. *International Journal of Solids and Structures*, **49**(15), 2155–2167.
- Wang, H., Wu, P. D., Wang, J., and Tomé, C. N. (2013a). A crystal plasticity model for hexagonal close packed (HCP) crystals including twinning and de-twinning mechanisms. *International Journal of Plasticity*, **49**, 36–52.
- Wang, H., Wu, P. D., and Wang, J. (2013b). Modeling inelastic behavior of magnesium alloys during cyclic loading–unloading. *International Journal of Plasticity*, **47**, 49–64.
- Wang, H., Clausen, B., Tomé, C. N., and Wu, P. D. (2013c). Studying the effect of stress relaxation and creep on lattice strain evolution of stainless steel under tension. *Acta Materialia*, **61**(4), 1179–1188.
- Wang, H., Wu, P. D., and Wang, J. (2015). Modelling the role of slips and twins in magnesium alloys under cyclic shear. *Computational Materials Science*, **96**, 214–218.
- Wang, Y. and Mora, P. (2008). Macroscopic elastic properties of regular lattices. *Journal of the Mechanics and Physics of Solids*, **56**(12), 3459–3474.
- Wu, P. D., Neale, K. W., and Van der Giessen, E. (1997). On crystal plasticity FLD analysis. In *Proceedings of the Royal Society of London A: Mathematical, Physical and Engineering Sciences*, volume 453, pages 1831–1848.
- Wu, P. D., Wang, H., and Neale, K. W. (2012). On the large strain torsion of HCP polycrystals. *International Journal of Applied Mechanics*, **4**(03), 1250024.

- Wu, W., Qiao, H., An, K., Guo, X. Q., Wu, P. D., and Liaw, P. K. (2014). Investigation of deformation dynamics in a wrought magnesium alloy. *International Journal of Plasticity*, **62**, 105–120.
- Xu, F., Holt, R. A., and Daymond, M. R. (2008). Modeling lattice strain evolution during uniaxial deformation of textured Zircaloy-2. *Acta Materialia*, **56**(14), 3672–3687.
- Xu, F., Holt, R. A., and Daymond, M. R. (2009). Modeling texture evolution during uni-axial deformation of Zircaloy-2. *Journal of Nuclear Materials*, **394**(1), 9–19.
- Zecevic, M., Knezevic, M., Beyerlein, I. J., and Tomé, C. N. (2015). An elasto-plastic self-consistent model with hardening based on dislocation density, twinning and de-twinning: application to strain path changes in HCP metals. *Materials Science and Engineering: A*, **638**, 262–274.